**Faculty of Science and Engineering**
**Department of Exploration Geophysics**

# Compaction Trends of Shales: Rock Physics and Petrophysical Properties

**Roman Beloborodov**

**This thesis is presented for the Degree of**
**Doctor of Philosophy**
**of**
**Curtin University**

**November 2017**

# Declaration

To the best of my knowledge and belief this thesis contains no material previously published by any other person except where due acknowledgment has been made.

This thesis contains no material which has been accepted for the award of any other degree or diploma in any university.

**Signature:** 

**Date:** 28/11/17

# Acknowledgements

I would like to thank my advisors, colleagues, and fellow students from the Department of Exploration Geophysics for this enjoyable yet sometimes challenging time that we spent together at Curtin University. I met a lot of specialists passionate about their work, hardworking and at the same time interesting and friendly people. I would like to thank them for being my family and helping me to develop and grow professionally during these three sunny years Down Under.

I am cordially grateful to Maxim Lebedev and Marina Pervukhina for their constant support, wise guidance, and kind hearts. They have always inspired me with exciting research ideas, encouraged me in any initiative, and helped to make right decisions during my research and life in Australia.

I thank Michael B. Clennell, Matthew Josh, Claudio Delle Piane, Tongcheng Han, Lionel Esteban, Dave Dewhurst and my other colleagues from CSIRO with whom I worked side by side, who influenced my way of thinking, and helped me to find interesting and challenging research tasks. I hope that in my future endeavours we will make a good team and challenge the new remarkable research tasks.

Of course, this journey of mine would not happen without my family. I whole-heartedly appreciate all the efforts my parents and grandparents put in guiding and educating me during my whole life. I am especially grateful to my wife Alena who always supported me along the way; she made any problem seem as nothing, and without her it would be a completely different story. I dedicate this work to our son Solomon wishing him to become a wise, strong, and kind man in the near future.

---

The research presented in this thesis was funded through the CSIRO Shale Rock Physics and Petrophysics (SHARPP) project sponsored by Total.

RB would like to acknowledge ASEG Research Foundation for sponsoring him with Grant (RF16P05).

# Abstract

This thesis is dedicated to investigation of the compaction trends of rock physics and petrophysical properties of shale. It is supplemented with analysis of shale microstructure as a key parameter controlling all the macroscopic properties of shale, their anisotropy, and compaction trends.

Shales are the most abundant and, at the same time, the least known type of rock. They are found in every sedimentary basin around the world. Lean shales comprise seals for conventional oil and gas reservoirs, whereas organic-rich shales are explored as an important source of hydrocarbons. Being an effective barrier for fluids shales are often considered as a target for nuclear waste disposal and $CO_2$ sequestration. Hence, the knowledge of the shale properties is of high practical importance and is essential for geomechanical, geophysical, and hydrogeological applications.

To investigate the compaction trends of shale properties, I designed and tailored a special experimental setup. It allows measuring permeability and anisotropic elastic properties of shales simultaneously during the mechanical compaction. At the end of compaction experiments I analyse the microstructure of compacted samples and their anisotropic dielectric properties.

In the first two chapters of the thesis, I provide reader with the present-day information on shales and describe the experimental methodology used in this study to measure their properties and parameters of microstructure. Following paragraphs outline the steps undertaken to conclude the study.

First, I analyse the effect of pore fluid on the formation of clay microstructure in shales and compaction trends of anisotropic elastic properties. I show that the salinity and pH of pore fluid are the key parameters determining the microstructure of clay sediment. Shales with different initial clay microstructure exhibit significantly different compressibility and consequently compaction trends of anisotropic elastic properties.

Second, I investigate the compaction trends of elastic properties and permeability of shales. The simultaneously acquired compaction trends of the permeability and seismic attributes measured normal to the bedding exhibit strong correlations. Mineral composition and quartz content are found to be crucial for broad variations of permeability in shales. I provide the empirical equations for estimating permeability from these parameters.

Third, I investigate the anisotropic electric properties of shales. Dielectric response of shales is strongly dependent on the cation composition of saturating brine, its salinity, clay fraction, and the direction of an applied electric field. I found that the dielectric anisotropy may be used for identification of the type of connate brine. The dielectric response of shales in megahertz range can be used to identify shales of saline and fresh water origins.

Fourth, we propose a new multiphase incremental model for the anisotropic dielectric properties of sedimentary rocks. The model is for any number of mineral grain components aligned in any direction and is independent of the mixing order.

Finally, the outline is drawn to highlight the most important results of this work and to illustrate its novelty. All the thesis chapters containing experimental results are based on the published papers that are provided in appendices.

# Index

# Chapter 1 – Literature review

## INTRODUCTION

Shale is a fissile and anisotropic type of mudstones that dominates among the rocks constituting sedimentary basins. Shales usually form effective seals on top of conventional oil and gas reservoirs although in some cases they can store significant for production amounts of hydrocarbons within their structure. Despite their wide distribution, we have very limited knowledge on their properties and compaction trends. This lack of knowledge is usually attributed to the complex multiphase and multimineral composition of shales.

In this chapter I discuss the role of environmental conditions and mechanical compaction in the formation of the shale microstructure. I illustrate the relationships between shale microstructure and properties. I analyse the latest literature and summarize the current knowledge regarding the anisotropic elastic, electric, and hydraulic properties of shales.

## A NOTE ON THE PROPERTIES OF CLAY MINERALS

Although clay minerals are the essential components of shales, to date, the information on the physical properties of individual clay particles is absent due both to our inability to measure them directly and to the high variability in chemical composition of clay minerals. The clay particles are anisotropic due to their layered crystalline structure (Vyzhva et al., 2014, Militzer et al., 2011, Sayers, 2005); and their spatial arrangement within the rock composite affects the anisotropy of all the macroscopic physical properties of clay rocks (Johansen et al., 2004, Clennell et al., 1999, Hirt et al., 1995, Sayers, 1994, Vernik and Nur, 1992, Seriff, 1985, Campbell, 1976). In addition to this, clay particles exhibit uncompensated charges on their edges and faces in the presence of polar liquids (e.g. water solutions), therefore causing the formation of an electric double layer on liquid-solid interfaces (Wang and Siu, 2006). The electric double layer may be subdivided into two parts: the bound or Stern layer that is immediately adjacent to the clay surface and the diffuse layer spreading farther into the solution. The water within the bound layer has properties significantly different from those of free water. It has higher viscosity, elasticity and tensile strength, a different density, and a dielectric permittivity approximately 40 times lower

(Boyarskii et al., 2002, Der'agin, 1989). The diffuse layer exhibits higher concentrations of counterions compared to the free water not affected by the clay surface. The presence of an electric double layer in water-saturated clay rock determines the way clay particles interact and consequently the microstructure that also affects all the macroscopic physical properties (Fam and Santamarina, 1995) including the elastic, electric and hydraulic ones.

## THE CHARACTERISATION OF SHALE DIAGENESIS

The properties of shale are significantly affected by the depositional environments, where the initially soft sediment is accumulated, as they control the clay content of a sediment, its chemical and mineral composition, pH of connate water, the amount of organic matter, and sedimentation rate.

The deposited sediment undergoes mechanical compaction under the weight of the overburden, losing most of its porosity and, because of the slow sedimentation rate, acquires microstructure oriented in the bedding direction. At greater depth, compacted shales may undergo chemical alteration under the influence of high temperatures and pressures, further reducing the porosity and increasing structural anisotropy due to recrystallization of some clay minerals.

The stress states of consolidated shale intervals are often altered due to the tectonic forces, maturation of hydrocarbons accompanied by the gas generation leading to an increase of internal pore pressure, fluid substitutions, and ongoing explorations from the nearby reservoir rocks. These stress changes, often anisotropic, lead to additional porosity and cracks within the shale on multiple scales and in particular directions, consequently affecting the macroscopic transport, elastic, and electrical properties of shales.

The latter effects are not considered in this work due to their secondary nature, whereas the thorough attention is paid to pure mechanical compaction as the main process responsible for formation of microstructure and properties of shallow shales buried up to ~3 km in depth at temperatures below 80˚C – the onset of chemical compaction.

## THE MICROSTRUCTURE OF CLAY ROCKS

In order to address the complex shale properties and their anisotropy, shale rocks have been investigated at multiple scales using various laboratory and field techniques,

numerical simulations, and theoretical modelling. Data integration is necessary to fully understand the nature and origin of complex properties of shale formations found in nature. However, the knowledge of shale microstructure as the foundation of its properties is essential for the design of rock physics models and interpretation of data acquired from different sources, e.g., seismic exploration and well-logs.

According to Sergeyev et al. (1980), microstructure is defined as the union of morphometric (size, shape, surface geometry of structure elements and their proportions), geometric (texture) and energetic features (e.g. the type of contacts between structure elements) of the rock, where each of them is controlled by the composition, volumetric ratio, and character of interaction between rock components.

In the beginning of the 20$^{th}$ century, Terzaghi (1925) highlighted the importance of clay rock microstructure in formation of its properties, and proposed a classification system for sediment microstructures. During the first half of the 20$^{th}$ century the ideas of Therzaghi were further developed. The behaviour of clay particles in saturated water solutions was described from the point of electric double layer theory and the processes of clay particle aggregation and flocculation were described in detail. In the 1950s, with the advent of the electron microscopy era most of the proposed theoretical models of clay rock microstructure were validated by the analogues found in nature. In 1963, Van Olphen (1977) has analysed the theoretically possible mechanisms of clay particle interactions in different physicochemical environments and came up with the three general types of clay microstructures, namely, aggregated, flocculated, and dispersed.

Later, in their fundamental study Collins and McGown (1974) illustrated the more diverse nature of the clay rock microstructure and described the few types of microstructures in relation to a rock genesis. They found that the characteristic properties of clay rock such as swelling, plasticity, and subsidence are attributed to different types of rock microstructure.

The most comprehensive classification of clay rock microstructures, to my opinion, was presented by Sergeyev et al. (1980). It is based on the large database of clay rocks that includes loose sediments, clays, mudstones, shales and argillites found across USSR and Polish People's Republic. The segregation of microstructure types was based on the most characteristic peculiarities of clay rocks, such as clay content, its state (aggregated, dispersed, or flocculated), orientation of structure elements and type of contacts between them, degree of compaction and the parameters of pore space. For the most part of analysed microstructures, their properties and especially the

orientation of structure elements is found to be strongly related to the environmental conditions.

To summarize, the microstructure of clay rocks determines their properties and should be investigated for the better understanding of clay rock properties, their origin, and evolution mechanisms.

## THE ROLE OF ENVIRONMENTAL CONDITIONS ON THE FORMATION OF CLAY ROCK MICROSTRUCTURE

Depositional environments determine the mineral composition of a clay rock, the chemical composition of its fluid component, and the organic content. In its turn, these factors control the formation of rock microstructure and properties. This influence of depositional environments on the microstructure and properties of a rock is illustrated in a number of studies.

Wang and Dong (2008) have studied the effects of pH of a pore fluid on the formation of a sediment employing elastic and dielectric measurements on two kaolinite-water mixtures. Artificial sediments were specifically prepared with different fabric formations by altering the pH of a pore fluid. The sample prepared with pH of 6.6, which is above the isoelectric point (IEP) of kaolinite (pH = 5), exhibited dispersed and deflocculated structure, while the sample prepared with pH of 3.4 exhibited edge-to-face (EF) flocculated structure.

It is shown that the sedimentation process might be divided into three distinct stages: particle settling, sediment accumulation, and sediment consolidation. In the first sample (pH = 3.4) accumulation stage is completed in several minutes due to aggregation of clay particles according to EF scheme and their fast settlement. Consolidation of the sample results in decrease of its volume over a short period of time. Uniform distribution of water content and particle sizes within the whole sediment was observed. In the sample with pH of 6.6, the strong double-layer repulsion between the particles prevents the aggregation of sediment. The particles settle individually under the gravitational force thereby slowing down the settling completion. The accumulation stage dominates during the whole time of sedimentation. The depth segregation of particles by their size and differential consolidation are observed in this sample.

Shear wave velocities measured with horizontal ($V_{SH}$) and vertical ($V_{SV}$) polarization along the bedding plane are identical in the flocculated sediment due to

the random orientation of clay particles. The velocities grow continuously during the consolidation of sediment. In the deflocculated sample the $V_{SH}$ is higher than $V_{SV}$ due to the inherent structure anisotropy caused by the face-to-face (FF) aggregation of clay particles.

Dielectric measurements of water relaxation strength indicate that the deflocculated sample have lesser bulk water content owing to denser particle packing, flocculated sample exhibit card-house structure, and therefore has higher bulk water content. During the consolidation, both samples show the decrease in bulk water, but the increase in relative bound water content as a result of increasing particle concentration.

In the flocculated sediment, the fluid conductivity has more contribution to the total conductivity than the surface charge conduction of the sediment. The consolidation of the sample results in a decreasing conduction due to the simultaneous reduction of pore sizes and the increased tortuosity of its pore network. The ratio of conductivity in different directions is close to unity as a result of structure isotropy. On the contrary, the dispersed deflocculated sample has higher surface charge conduction relatively to fluid conduction resulting in the increasing conductivity of the sediment during the consolidation, as the volumetric concentration of particles in the sediment volume increases. The face-to-face aggregation of the sample results in conductivity anisotropy of 1.1 with higher conductivity value along the bedding direction.

This study illustrates how the change in chemical composition of a fluid leads to significantly different results in terms of microstructure and properties of a sediment given the same mineral composition. However, natural sediments will differ even more as their mineral composition as well as the cation composition of a pore fluid will vary in different parts of sedimentary basins.

Jiang et al. (2017) have showed that the properties of the natural shales are indeed controlled by depositional environments. The authors have compared a number of shale rock samples from marine, lacustrine, and transitional environments found in the Sichuan Basin (China) and illustrated how they differ in terms of mineral composition, permeability, porosity and organic content.

In their case, shales from marine environment are characterized by the lowest clay content and permeability, highest brittle mineral content, and have greater micron- and nano-scale porosity within the organic matter compared to lacustrine and

transitional shales. The shale gas is evenly distributed across the marine facies and shows the best prospect rates.

Transitional shale shows the lowest porosity, highest clay content, and hence the significantly lower values of permeability than in lacustrine shales. The extraction of hydrocarbon seems to be impracticable due to the very low completion quality.

The shales of lacustrine origin are characterized by intermediate brittleness between the transitional and marine shales. These shales are interbedded with layers of sandstones and carbonates and exhibit the highest permeability. These properties make the lacustrine shales a good candidate for oil and gas production.

This study illustrates the effect of environmental conditions on clay rock composition and consequently on its microstructure and macroscopic properties. Different depositional environments of the Schiuan basin resulted in formation of three types of rocks with the distinctive brittleness, permeability, and maturity of organic matter.

The extensive study of microstructure and macroscopic properties of the Ordovician shales from the Barrow Basin (Western Australia) in relation to their postsedimentation diagenesis was conducted by Delle Piane et al. (2015).

They found that the early cementation of supratidal Bongabini shale by dolomite and anhydrite has formed a stiff framework that resisted the following mechanical compaction. As a result, Bongabini shale has preserved the early compaction microstructure. In contrast, the open marine shale from Goldwyer Formation has not experienced significant cementation initially and being composed of mostly quartz and illite its further mechanical compaction has led to the formation of strongly oriented microstructure. The difference in the degree of clay particle alignment has been evidenced with X-Ray Texture goniometry (XTG): the shale from the Bongabini Formation has a weaker preferred orientation compared to Goldwyer Formation shale with multiples of random distribution (m.r.d.) of 2.54 and 5.77 respectively.

The observed microstructural anisotropy (the degree of illite alignment) of the two shales explains the different values of their elastic anisotropy, therefore, Goldwyer shale show the higher degree of elastic anisotropy than Bongabini shale for both P- and S-wave velocities.

This exemplary work highlights the role of sedimentation environment, diagenetic processes such as cementation, mechanical compaction and chemical

mineral transformation and their sequence in the formation of shale microstructure. It has been showed that these factors influence the degree of alignment of a clay fraction.

Wenk et al. (2008) have investigated kaolinite-illite-rich shale samples from Switzerland and France with synchrotron X-Ray spectrometry in order to quantify the texture parameters of the samples and obtain the orientation distributions of different mineral phases.

The results of this study showed that the investigated samples have either moderate or strong preferred orientation of mineral phases. Observed orientations are conditioned by the geological history of the formation and correlate well with the anisotropy of elastic and transport properties of these shales.

The environmental conditions are also responsible for the formation of sealing properties and strengths of hydrocarbon traps. Osipov et al. (2004) have analysed a large database of clay rocks and showed that their sealing properties strongly depend on the facial belonging, and the latter determine the mineral composition of a clay fraction and the macroscale structure of a clay rock strata.

The facial approach allows dividing clay seals into three groups. The first group originates from calm hydrodynamic setting at the deepest part of sedimentary basins. Clay rocks within this group are characterized by uniform composition, lowest content of coarse material (e.g. silt, sand) and high amounts of swelling clay minerals. These rocks form the best seals impermeable for oil and gas.

The second group is formed on a shelf and marginal deltaic zones. It has increased concentration of coarse mineral grains and tends to be less uniform in composition. Non-swelling illite and mixed-layer clay minerals are dominating within this group. These rocks are impermeable for oil and are usually permeable for gas via slow diffusion processes.

Clay seals of the third group are non-uniform, they have a significant amount of sand material often interbedded with the non-swelling minerals, namely, kaolinite, illite, chlorite. They are considered as poor seals and cannot stop the migration of hydrocarbons themselves.

Authors described models of microstructures and mechanisms of their evolution with depth for different classes of clay seals in relation to their facial belonging. These models allowed estimating the tensile and compressional strength of test seal-rock samples given the data on burial depth, mineral composition, and quantitative geometrical properties of microstructure (e.g., contact angle between clay particles).

Finally, the compaction trends of tensile and compressional strength were acquired for different types of clay seals. These trends showed a good correlation ($R^2 > 0.8$) with the available empirical data. The best fit between the predicted curves and the data is observed at the depth above 2.5 km. However, these trends slightly overestimate the measured data due to the inability of the models to predict the weakening of the core samples upon recovery/extraction. At greater depths, the trends deviate stronger due to the effects of fracturing occurring at these depths that are not accounted for in the modelling.

This work illustrates the strong relationship between the rock microstructure, its mechanical strength, and sealing properties. It is showed that the evolution of microstructure with depth consequently leads to changes in rock properties.

## THE MECHANICAL COMPACTION OF SHALES

The mechanical compaction is a process that occurs with a newly deposited soft and highly porous sediment under overburden pressure. It takes place in sedimentary basins at the first few kilometres below the surface and leads to porosity reduction via re-arrangement of the mineral particles (Bjorlykke, 2014, Hedberg, 1936, Weller, 1959, Rieke et al., 1978, Vasseur et al., 1995, Dewhurst et al., 1998, Djeran-Maigre et al., 1998, Pervukhina et al., 2011). The mechanical compaction of shales attracts close attention of geoscientists as it is poorly understood, governs vertical seismic velocity profiles and is one of the main reasons for elastic, mechanical, hydraulic, and electrical polar anisotropy in the most of clay-bearing sedimentary rocks (Vasseur et al., 1995, Bachrach, 2011, Lonardelli et al., 2007, Wenk et al., 2008, Voltolini et al., 2009, Gao et al., 2015, Pervukhina and Rasolofosaon, 2017).

From the practical point of view, compaction trends are crucial in seismic exploration, flow modelling, and borehole geomechanics for several reasons. They are often used to detect overpressured zones, to build velocity models and convey depth conversions in seismic, to predict seismic response in sand-shale interfaces at various depths, and to detect hydrocarbon reservoirs in seismic data distinguishing them from anomalies.

Although analysis of compaction trends can be approached at different scales, each strategy has its own advantages and disadvantages (*Table 1*), and it is important to understand them. Compaction trends are challenging to study in natural shales as they are influenced by multiple factors, namely, clay mineralogy, silt fraction,

developed overpressure, maximum experienced burial stress, etc. It is difficult if not impossible to segregate the factors that have essential influence on the resultant burial velocity trend from those that might be neglected. This thesis is focused on the analysis of compaction trends using the mechanical compaction of artificial shales as the most flexible and accessible method. This approach is advantageous above others as it provides total control over the composition and stress state of a rock and allows simulating mechanical compaction at the whole shallow section of sedimentary basin ranging from 0 to ~3–5 km, before the depth of the temperature onset of chemical compaction (80˚C).

*Table 1. The comparison between the scales for analysis of compaction trends in clay rocks.*

| Scale | Advantages | Disadvantages |
|---|---|---|
| Seismic | • in situ conditions<br>• large amounts of data<br>• the best coverage of a target | • averaging of the properties of different rock types<br>• indirect relation to non-elastic properties<br>• only local trends<br>• absence or poor quality of data at the interval of interest |
| Well logs | • in situ conditions<br>• dense sampling of the targeted intervals<br>• simultaneous measurements of different rock properties | • data is affected by the tool coupling<br>• the effect of cracks cannot be eliminated<br>• absence or poor quality of data at the interval of interest |
| Core analysis | • detailed information on rock properties<br>• direct measurements of rock properties<br>• application of unconventional measuring techniques | • the limited number of samples at different depths<br>• irreversible deformations upon extraction of samples<br>• the influence of different mineralogy on properties cannot be investigated<br>• complex and non-uniform multimineral system |
| Experimental compaction of resedimented clays | • an ability to reconstruct the in-situ conditions at different depths<br>• analysis of the trends for a fixed rock mineralogy | • multimineral composition<br>• no control over the microstructure, mineralogy, and fluid composition<br>• difficult to match mineralogy to the rock of interest |
| Experimental compaction of artificial shales | • full control over the composition and microstructure<br>• compaction trends for a fixed rock mineralogy<br>• compaction trends for the whole shallow section of a basin<br>• approach is useful for validation of rock physics models | • the artificial shales are generally simpler than their natural analogues<br>• it is possible to create non-realistic rocks<br>• relatively fast consolidation of samples |

A number of studies conducted at different scales outlined the essential factors and mechanisms controlling the mechanical compaction of shales and sands (Moyano et al., 2012, Marcussen et al., 2009, Day-Stirrat et al., 2008, Revil et al., 2002, Dewhurst et al., 1998, Bjorlykke, 1998, Vasseur et al., 1995, Rieke et al., 1978, Weller, 1959, Hedberg, 1936, Hamilton, 1979). However, most of these works avoided the question of microstructure evolution due to compaction. More recent works show that the microstructure along the mineral and fluid composition of rock components have the dominant effect on compaction trends (Pervukhina and Rasolofosaon, 2017, Zadeh et al., 2016, Delle Piane et al., 2015, Bjorlykke, 2014).

Some of the exemplary studies outline the to-date knowledge about the compaction, draw our attention to the key practical difficulties associated with it, and pose questions yet to be answered.

Thus, Hamilton (1979) being particularly interested in the modelling of the seafloor and concerned by the lack of available information on velocity depth trends in shallow marine sediments has analysed a sonobuoy data collected in the Gulf of Mexico and described certain velocity trends at the depths above 1km. Despite the same origin and the general increase of velocity with depth, these trends are significantly different for the sediments of different genesis and composition. He extensively discussed the influence of overburden pressure, temperature, and cementation on the formation of observed velocity gradients in siliceous, calcareous and turbidite sediments at the Gulf of Mexico.

Motivated by the shortage of conventional well-log data in the shallow section of the Gulf of Mexico, Dutta et al. (2009) used data integration approach to calculate the velocity and porosity-depth trends. They found that the shallow sections are highly non-uniform and simple extrapolation of compaction trends upwards, calculated using the data on lower sections, can lead to wrong results in the shallower section.

Pervukhina and Rasolofosaon (2017) have performed the analysis on a large database (more than 800 samples) of measured shale properties and showed that the burial depth or compaction have no first order influence on the elastic anisotropy of shales. They have showed that the elastic anisotropy of shales may be well explained and defined by the preferred orientation/alignment of clay platelets. The authors also suggest that the orientation of clay platelets is determined by the conditions of deposition environment: the rate of sedimentation, pH and the salinity of a pore fluid, what links back to the microstructure of shale.

Significant progress in understanding the microstructural changes under the influence of compaction was achieved with laboratory compaction experiments conducted on artificial silt-clay mixtures with controlled mineralogy (Mondol et al., 2007, Mondol et al., 2008, Voltolini et al., 2009, Fawad et al., 2010). Recent studies of the laboratory compaction were complemented with detailed microstructural analyses (Lash and Blood, 2004, Aplin et al., 2006, Day-Stirrat et al., 2011). The advance in understanding of microstructural changes due to the mechanical compaction was also accompanied with numerical modelling of the compaction process and corresponding changes in petrophysical properties of shales (Bachrach, 2011, Moyano et al., 2012, Johansen et al., 2004, Dræge et al., 2006).

Laboratory experiments on artificial shales have also raised new questions. For example, some studies showed that the shales having the same mineralogical composition exhibit different properties at the same porosity and cannot be described with the same burial trend (Mondol et al., 2007). A few of the questions alike are outlined below. How do the elastic properties and anisotropy develop with compaction of sediment? Does the microstructure affect the compaction behaviour and consequently the properties of rocks? How different are the parameters of various microstructures and what do we expect to see in natural rocks? I address these questions to the best of my knowledge in the Chapter 3 of the thesis.

## THE ANISOTROPY OF SHALE ROCK PROPERTIES

Shales are notorious for having the strong anisotropy of almost all of their properties, including elastic, electric, mechanical, and transport ones (Josh et al., 2016, Donadille, 2016, Adams et al., 2016, Mokhtari and Tutuncu, 2015, Gao et al., 2015, Saba et al., 2014, Day-Stirrat et al., 2012, Kuila et al., 2011, Sayers, 2010). It is convenient to divide the sources of shale anisotropy into two groups: intrinsic and extrinsic, as suggested by Allan et al. (2015). In their study, authors have applied multiphysics approach to characterize the velocity anisotropy of 5 dried organic rich shales. They showed that the coupling of the conventional petrophysical methods such as ultrasonic velocity measurements with imaging techniques including, SEM, X-Ray texture goniometry, and micro-CT scanning enables complete characterization of the sources of elastic anisotropy in shales.

Authors suggest dividing the sources of shales' velocity anisotropy into intrinsic, determined by the degree of the preferred orientation of mineral phases, and extrinsic,

conditioned by the presence of soft crack-like porosity. It has been shown that intrinsic anisotropy in dried shales attributes to at least 70% of total elastic anisotropy at low confining stresses (up to 15 MPa), however, it is expected that the pore pressure preserves soft porosity in in situ shales and this effect becomes significant at higher confining pressures.

Intrinsic anisotropy of shales is determined by several different factors. First, clay minerals have structural anisotropy due to their layered crystalline structure and most often reside in a form of platy like particles. During the sedimentation and following mechanical compaction, clay particles align and combine together to form aggregates or continuous matrix, consequently forming networks of aligned pores between them. Finally, the thin laminations of clay material may form layered anisotropic structures (Osipov et al., 1989). This intrinsic anisotropy determines the mechanical properties of a rock and to some extent controls the extrinsic anisotropy of shales by the means of preferred orientations and geometry of cracks forming under the complex stress configurations (Piane et al., 2011).

The latter mechanism is described in detail in the study by Kuila et al. (2011) who have studied stress and velocity anisotropy in low-porosity illite-rich shale samples from the Officer Basin in Western Australia. Samples were subjected to both isotropic and anisotropic stress fields during consolidated undrained multi-stage triaxial tests. The elastic P- and S-wave velocities were measured in multiple directions at each stage of the tests. Shales appeared to have consistent velocity and velocity anisotropy behaviour during the testing. These shales are characterized by initially high levels of intrinsic elastic anisotropy due to lamination of both mica and clay minerals. Additionally, authors note the microfractures of various aspect ratios oriented along the particle lamination.

Increase of confining stress normal to the bedding have resulted in two independent effects: 1) microfractures with small aspect ratio close progressively during the test, resulting in the increase of both vertical P- and S-waves velocities and reducing the elastic anisotropy; 2) higher differential stress initiates dilatation of the sample and the formation of axial tensile fractures, reducing the elastic velocities in horizontal direction and further diminishing the elastic anisotropy. Nevertheless, quasi P-wave measured at a 45-degree angle show little to no dependency on differential stress, but appears to be most sensitive to confining pressure.

Authors conclude that the initial presence of the preferred orientation of minerals along the aligned porosity and compliant microfractures in bedding directions explain the initial intrinsic elastic anisotropy in the shales and its evolution under applied anisotropic stress. One must note that as the stress anisotropy changes, the velocity and velocity anisotropy in shales is controlled by the orientation of texture in relation to the maximum principal stress direction.

This thesis is focused on the intrinsic anisotropy of shales alone, whereas the effects of anisotropic stress and crack distribution on the formation of anisotropy of shales cannot be investigated in the present compaction setup configuration. The anisotropy of elastic and electrical shale properties, and the compaction trends of anisotropic elastic properties in relation to the shale microstructure are investigated in Chapters 3, 4 and 5 of the thesis.

## THE FLUID PERMEABILITY IN SHALES

Knowledge of the fluid permeability of mudstones is crucial for hydrogeology, basin modelling and nuclear waste disposal (Wang et al., 2013, Hasanov, 2014). However, the link between measured log data and the hydraulic permeability is still poorly understood (e.g. Heller et al., 2014). This can be attributable to a limited number of permeability measurements available on mudstones due to (1) the challenge to measure the extremely low permeabilities that are specific to shales and large experimental errors associated with these measurements and (2) the fact that shale intervals are rarely cored.

At the same time, even the limited sampling pool and large experimental errors mentioned above cannot explain the fact that the permeabilities reported for mudstones differ by up to ten orders of magnitude at the same porosity (e.g. Dewhurst et al., 1998, Yang and Aplin, 2010). It has also been shown that the permeability of the rock is strongly related to its lithology. This effect is even more prominent in clay rocks where a slight change in the mineralogical composition of the clay fraction drastically affects their permeability and compressibility (Dewhurst et al., 1998).

To overcome the lack of information on natural mudstones, a number of studies were conducted on resedimented clays, i.e. prepared using the powders of natural mudstones, that mimic the mineralogical composition of natural clay rocks. Although these studies helped to achieve a good understanding of permeability anisotropy and relations between permeability and some petrophysical parameters (Clennell et al.,

1999, Adams et al., 2016), they are not suitable for verification of existing rock physics models due to the complex composition and inhomogeneity of the resedimented clays.

Measuring the permeability of shales can be a challenging task, and conventional methodologies such as a steady-state method are usually not applicable to them. A detailed overview of five methods for measuring the permeability in shale samples is presented in a study of Mokhtari and Tutuncu (2015). They have also applied crushed-sample, pulse-decay and complex transient methods to measure the permeability in organic-rich black shale, Mancos, and Eagle Ford shale samples. The effects of heterogeneity and anisotropy of the samples on the permeability and permeability hysteresis in relation to applied stress are discussed in the paper. Additionally, authors indicate some advantages and disadvantages of using these methods for permeability characterization in shales.

Dependency of permeability on the sample size has been observed in the crushed sample method (GRI). Although there is no effect of microcracks on permeability measurements acquired with the GRI method, authors suggest that more detailed investigation is required to reliably compare the results of this method with the other common methods.

The three-sample method (vertical, horizontal and 45-degree) for the estimation of permeability anisotropy may be unreliable in the samples heterogeneous at 1-inch scale. The other source of error in permeability measurements this method is the inhomogeneity due to the microcracks generated by decompression. Therefore, quality control by the means of micro-CT investigation on each sample is required prior to the pure matrix permeability measurements.

It has been shown that the transient methods for measuring shale permeability are more reliable and less time consuming than most of conventional ones. For instance, the complex transient method is a faster substitute for a pulse decay method in low-permeable rocks. Additionally, it allows returning the sample to the initial stress state at the end of a cycle and consequently repeating the procedure with the different frequency. It is shown that the adequate frequency should be used to achieve the correct results.

The pressure-oscillation method for permeability measurements in tight rocks is defined and implemented in the works by (e.g. Bernabé et al., 2006, Fischer, 1992, Hasanov et al., 2017). This method is found advantageous over the others as it can be implemented directly during the compaction experiment. It is reliable and allows

controlling the stress state of a sample. For further reference, Table 2 illustrates the simple comparison of different methods with references to methodology.

Chapter 4 of this thesis is dedicated to the analysis of compaction trends of permeability in artificial shales in relation to the clay mineralogy and volumetric content of the silt fraction. I have chosen the pressure-oscillation technique for permeability measurements as the conventional techniques are rather time consuming and not applicable to tight rocks, whereas the other more advanced methods are not reliable enough or could not be implemented during mechanical compaction experiments, where the latter is essential for the present work.

*Table 2. Assessment of different methods for permeability measurements*

| Methods for permeability measurements | Evaluation criteria | | | | | | | | | | |
|---|---|---|---|---|---|---|---|---|---|---|---|
| | Applicable to tight rocks (perm < 1nD) | Applicable during the compaction | Ease of implementation | Reasonable timing of the experiment | Stress control | Pore pressure control | High precision | Field applicability | Analysis of fluid flow anisotropy | Data enhancement in frequency domain | Overall rating |
| Cuttings (GRI) (Luffel et al., 2013) | ✓ | – | ✓ | ✓ | – | – | – | – | – | – | 3 |
| Steady-state (Bertoncello and Honarpour, 2013) | – | ✓ | ✓ | – | ✓ | ✓ | – | ✓ | – | – | 5 |
| Bender element (Kang et al., 2014) | ✓ | – | – | ✓ | – | – | ✓ | – | ✓ | ✓ | 5 |
| Pore-scale modelling (Dewers et al., 2012) | ✓ | – | ✓ | ✓ | – | ✓ | – | – | ✓ | – | 5 |
| Transient methods (Heller et al., 2014) | ✓ | ✓ | ✓ | ✓ | ✓ | ✓ | ✓ | ✓ | ✓* | – | 9 |
| Pressure oscillation (Hasanov, 2014) | ✓ | ✓ | ✓ | ✓ | ✓ | ✓ | ✓ | ✓ | ✓* | ✓ | 10 |

* - requires special setup design modifications

## DIELECTRIC PROPERTIES OF SHALES

Among the physical and petrophysical parameters employed for shale characterization, the electrical and more specifically dielectric properties are one of the most direct and effective ways for a discrimination of geo-fluid types and concentrations as well as for the inference of their transport properties.

Dielectric permittivity of a material is a measure of its frequency dependent electrical polarizability (Von Hippel, 1954), in an applied external electric field. In the presence of an electric field, electrons, ions, and polar molecules all contribute to frequency dependent dielectric properties. In composite materials, the build-up of charge at dissimilar conductivity boundaries and the creation of exchangeable cations may completely dominate the dielectric behaviour. For example, rock consists of liquid, solid, and gas components and each of them is clearly defined by specific chemical and/or mineral composition. Although the dielectric constants of the most of individual rock components rarely exceed 80, the bulk dielectric permittivity of a rock sample may reach many orders of magnitude at the radio frequency range (kilohertz to megahertz), implying that not only the constituents of a rock but also their geometry, interaction, spatial arrangement, and interfaces have a significant contribution to polarization (Sen, 1981).

In clay bearing rocks, the presence of a connate brine results in so-called surface effects: electric double layer polarization (i.e. Stern layer polarisation) and Maxwell-Wagner space-charge polarisation. They occur due to the presence of polarisable bound water at the clay-water interface and weakly bounded ions on the surface of mineral particles, which can slowly move under the influence of an external field and contribute to both the conduction and electric polarisation (Sen and Chew, 1983). These effects become prominent at frequencies below MHz range and complicate the interpretation of data.

Dielectric measurements in petrophysics and petroleum industry are mostly used to determine the water content. Water molecules have a fixed electrical dipole moment and rotate quickly to align with an external electric field (Freed et al., 2016), whereas hydrocarbons have non-polar molecules and as a result have much lower permittivity than water. Therefore, estimating the moisture content from the dielectric permittivity at high frequencies (>1 GHz) is often used in borehole petrophysics. However, dielectric logging at frequencies of 1 GHz and above remains challenging in field

measurements due to the decreased depth of penetration of an electric field. On the contrary, currently available commercial dielectric tools operate at multiple spot frequencies (Hizem et al., 2008) to facilitate a determination of water content and CEC: dielectric response at frequencies below 50 MHz is more affected by the surface effects described above (Josh et al., 2015). At lower frequencies, clay content, geometry and spatial orientations of mineral rock constituents, and the salinity of pore fluid also affect the measured dielectric permittivity (Garrouch and Sharma, 1994, Sen, 1980).

Some recent studies suggest alternative methods for oil recovery in unconventional reservoirs that utilize dielectric heating (Mukhametshina and Martynova, 2013). This technology allows increasing the economical efficiency of exploration and reducing the ecological impact on the environment. It heavily relies on knowledge of the dielectric behaviour in the kilohertz-megahertz range of frequencies where the depth of electric field penetration is sufficient for field applications and the dielectric loss-factor exhibits peak values (Abraham et al., 2016). However, the interplay of several physical effects results in wide dispersion of dielectric relaxation peaks at frequencies below gigahertz. Identifying of the frequencies of these attenuation peaks as well as the estimation of the range of dielectric dispersion for specific types of rock would be useful for tuning the frequency of dielectric heating tools to ensure the energy efficient and productive heating.

Another purpose of dielectric measurements is the estimation of cation exchange capacity (CEC), a property that is directly attributed to mineral composition and specifically to clay content. Josh (2014) showed a strong correlation between dielectric response at ~30 MHz and the CEC. In turn, this property is linearly proportional to the specific surface area (SSA) of a rock that determines the character and amount of inter-particle contacts (coordination number) under the given mineral composition and porosity of a rock. Therefore, it is expected that dielectric constant should correlate with both static and dynamic elastic properties of a rock.

Also, knowledge of dielectric properties of artificial clay seals is important for hydrogeological applications and may be used for non-invasive detection of the chemical reactions between the clay minerals and sequestered contaminants (Canan, 1999, Olhoeft, 1992). Therefore, artificial clay-water mixtures can be effectively used to assess and analyse the dielectric response in controlled laboratory environments.

It is hard to segregate and independently study different factors influencing the dielectric properties of natural shales due to the complex composition of their mineral and fluid components. There are many experimental, and theoretical studies dedicated to frequency dependent dielectric properties of rocks in relation to the geometry of their components (e.g. aspect ratios and orientation of mineral grains and pores), water saturation, and organic content (e.g. Berryman and Hoversten, 2012, Sen, 1981, Al-Harahsheh et al., 2009). However, there is very little evidence of studies taking into account the clay content, microstructure, and the chemical composition of pore fluid (e.g. Garrouch and Sharma, 1994, Freed et al., 2016). The anisotropy of dielectric properties of shales is crucial for the interpretation of dielectric well-logs, especially in deviated wells, and may affect the efficiency of production via the dielectric heating in unconventional shale reservoirs (Donadille, 2016, Josh et al., 2016). Again, there is little to no evidence on how the anisotropy of dielectric properties of shales depend on the aforementioned parameters. The least known parameter in terms of its effect on dielectric response is the microstructure of the clay fraction in shales. Different geological settings may significantly affect the microstructure of sediment and consequently its properties (Beloborodov et al., 2016b). For example, Dong and Wang (2008) showed that the kaolinite sediments saturated with water solutions of different pH exhibit significantly different dielectric spectra due to the different mechanisms of microstructure formation.

Although dielectric properties are easily acquired in field and laboratory practices, for improved inversion and interpretation of this data, a robust rock physics model that links the bulk dielectric properties of shales to those of the rock-forming components is essential. Such models must also be able to account for the shale anisotropy caused by the preferential orientation of various mineral components.

In recent decades, shale dielectric modelling was mainly focused on the effects of the electrical double layer associated with clay minerals (e.g. Josh, 2014, Clavier et al., 1984, de Lima and Sharma, 1990, Glover et al., 1994, Leroy et al., 2008, Rabaute et al., 2003, Revil and Skold, 2011, Schwartz and Furman, 2012). Efforts have been made to develop models that can explain the dependence of the complex electrical conductivity on CEC and SSA, salinity and pH of the pore fluid, sorption of cations and organic molecules, grain sizes of mineral components, temperature, and water saturation. Thus, for example, Revil et al. (2013) generalized the versatile model to the case of anisotropic shales by introducing tensorial versions of the formation factor and

tortuosity to quantify the effect of kerogen on surface conductivity and quadrature conductivity. However, the model accounts only for the Stern layer (the inner portion of the electrical double layer coating the surface of mineral grains) polarisation (Stern, 1924), and neglects an important polarisation mechanism in the intermediate frequency range (0.1 MHz–100 MHz), often referred to as Maxwell-Wagner polarisation or interfacial polarisation induced by the built-up charge on the interfaces of heterogeneous systems.

To describe the dielectric behaviours of a heterogeneous system caused by the Maxwell-Wagner polarisation, various models have been developed (e.g. Sen et al., 1981, Berryman, 1995, Gelius and Wang, 2008, Ellis et al., 2010, Han et al., 2011, Berryman and Hoversten, 2012, Saevik et al., 2014). Among these models the differential effective medium (DEM) models had the most success in simulating the dielectric behaviour of clay-free sedimentary rocks (Berg, 2007). For example, the Hanai-Bruggeman (HB) equation (Bruggeman, 1935, Hanai, 1960, Hanai, 1961, Bussian, 1983) is one of the DEM models that predicts the bulk dielectric properties of a rock through the dielectric properties of its components, their volume fractions and spatial arrangement described by the cementation factor ($m$). However, the HB model is designed for the isotropic medium only and could not be used for modelling of the anisotropic dielectric properties of shales. The Asami (Asami, 2002) model is another kind of the DEM model that is capable of modelling the dielectric properties of a medium at any given direction relative to the applied electric field. The Asami model is a 2-phase (i.e., solid minerals and fluid) model that assumes all the solid particles are uniformly shaped and aligned, which however, is not the case for the natural shales. Therefore, modelling of the dielectric properties of natural rocks requires the development of a multiphase anisotropic dielectric model where the complex mineral composition and the orientation distribution functions of the clay minerals can be accounted for. The model should also take into account the Stern layer polarisation associated with clay minerals.

In Chapters 5 and 6 of the thesis, I investigate the frequency dependency of anisotropic dielectric properties of shales in relation to the clay content, microstructure of the clay matrix, and chemical composition of connate fluid. The new DEM model for the dielectric properties of shales is presented and successfully applied to a set of the prepared shale samples.

# Chapter 2 – Methodology

## INTRODUCTION

In this chapter, I describe the setup that was used for laboratory mechanical compaction experiments and the set of methods used for property measurements and microstructure characterization. I had to design and machine my own setup as there were no existing analogues that allowed measuring anisotropic elastic properties during the compaction and simultaneously measure permeability. The current setup allows measuring elastic P- and S-wave velocities in three directions, it also allows precisely measuring permeability of a sample at any stage of the compaction via the pressure-oscillation technique. I describe the materials and methodology used for the sample preparation as well as the compaction procedure. Three sections of the chapter are dedicated to the measurements of elastic, hydraulic, and electrical properties of the samples. I also tested and adopted several algorithms for autopicking of the arrival times for the ultrasonic measurements that are generally used in non-destructive testing and seismology. A set of methods for quantitative and qualitative analysis of microstructure are also discussed.

## EXPERIMENTAL SETUP

The compaction setup shown in Figure 1 is specially designed and tailored for the compaction experiments. The oedometer cell and plastic pistons that conduct pressure to the sample are made of Polyether ether ketone (PEEK) plastics. This material can withstand up to 80 MPa of uniaxial stress and up to 40 MPa of hydrostatic pressure within. Constant axial stress is applied vertically on the top piston by the hydraulic actuator connected to the automatic pump.

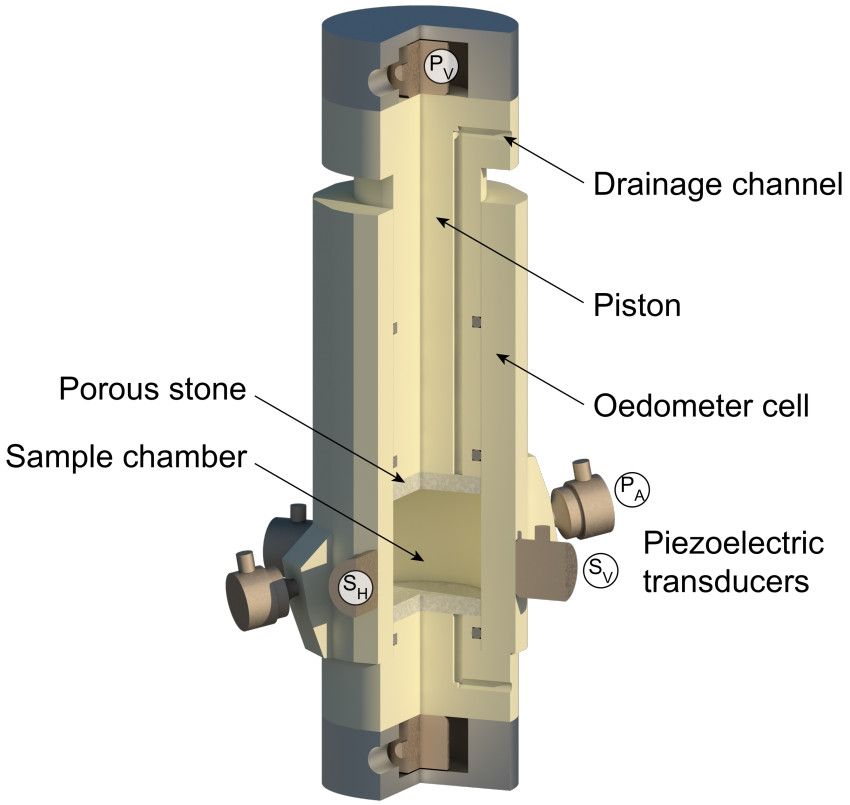


*Figure 1. 3D-section of the compaction oedometer illustrating the key elements and the positioning of piezoelectric ultrasonic transducers: $P_V$, $P_A$ – for measuring the vertical and angular P-wave velocities, $S_V$, $S_H$ – for measuring the slow and fast S-wave velocities, respectively, and the horizontal P-wave.*

The setup allows compacting samples in drained and undrained regimes. The space between the cell and the pistons is sealed with silicone rings to prevent the water leakage. Both pistons have drainage channels connected to the automatic pump via the high-pressure pipelines that allow accurate control of the pore pressure and fluid flow within the sample. Hydrostatic pressure at the top and bottom pistons can be monitored independently via the two piezoelectric pressure gauges installed on either side of the separating valve.

The material of the oedometer cell has a low acoustic contrast with the sample and allows measuring velocities of elastic waves propagating through the sample. Four pairs of high frequency (the central frequency of 1 and 2.5 MHz) ultrasonic piezoelectric transducers, attached to the cell and pistons (Figure 1), allow measuring the propagation times of ultrasonic pulses in three directions within the sample. Thus, two pairs of S-wave transducers are attached to the walls of the cell in the horizontal plane. One pair is polarised along the axis of cell symmetry ($S_V$) while the other one is polarised normal to it ($S_H$). A pair of P-wave transducers ($P_A$) is positioned at the

angle of 80 degrees from the cell symmetry axis. The last pair of P-wave transducers ($P_V$) is attached to the top and the bottom plastic pistons. This combination allows estimating the P-wave velocities in vertical and horizontal directions, and at an arbitrary angle to the sample's symmetry axis along with both slow and fast S-wave velocities. Assuming the vertical polar anisotropy of the sample full tensor of elasticity can be calculated from the measured data at any stage of the compaction process.

## SAMPLE PREPARATION

Quartz and clay powders (e.g. smectite, kaolinite) are used to prepare samples for the mechanical compaction (Figure 2). These minerals are abundant in natural shales. Kaolinite is a clay mineral that is relatively easy to work with due to its stable chemical composition and non-swelling structure compared to the clay minerals of the smectite group. The size of kaolinite aggregates (associations of individual clay platelets) does not exceed 75 μm (Figure 3). Their aspect ratio varies between 0.1 and 1.0. Smectite powder consists of individual smectite platelets with less than 2 μm in diameter and 100 nm in thickness (Figure 4). The crushed quartz powder consists of grains with the mean aspect ratio of 0.5 (oblate spheroids) and size of 2-150 μm (Figure 5). Geometrical parameters of the mixing components are derived from the analysis of SEM and micro-CT images of clay and quartz mineral powders, respectively. These parameters are summarized in Table 3.


*Figure 2. Mineral powders used for preparation of clay-silt mixtures.*

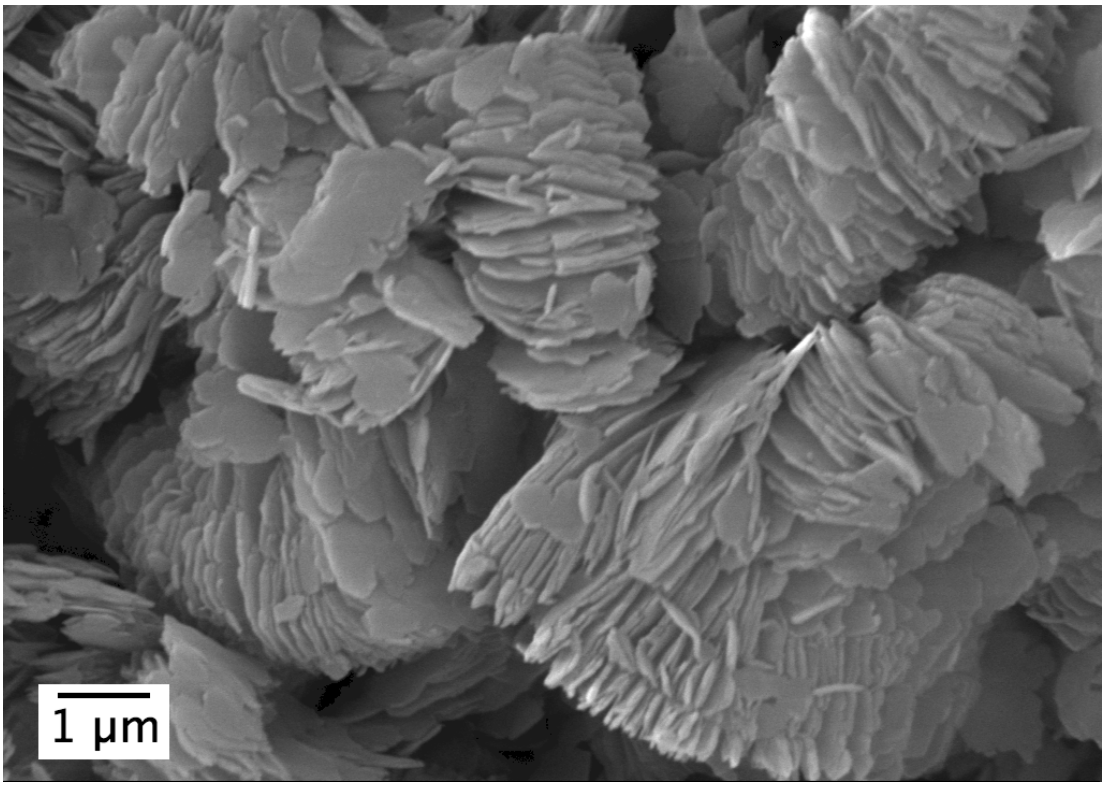


*Figure 3. SEM image of the kaolinite microaggregates consisting of oriented individual clay platelets and ultramicroaggregates.*

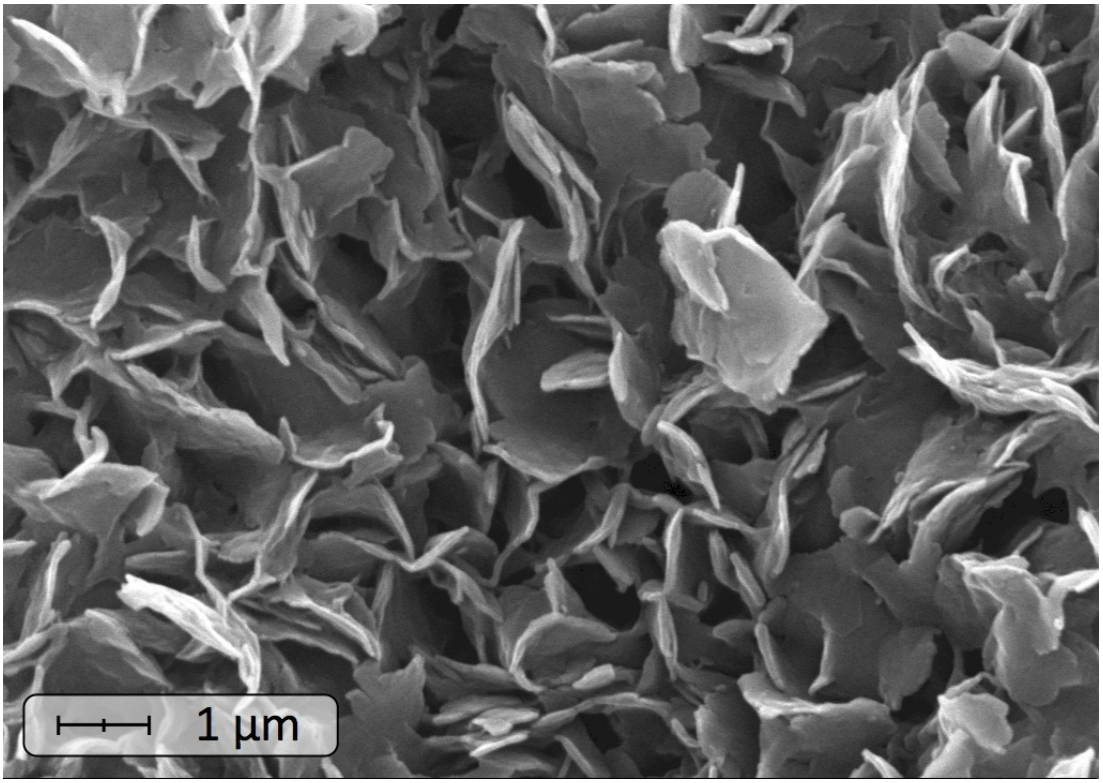


*Figure 4. SEM image of dispersed smectite particles.*

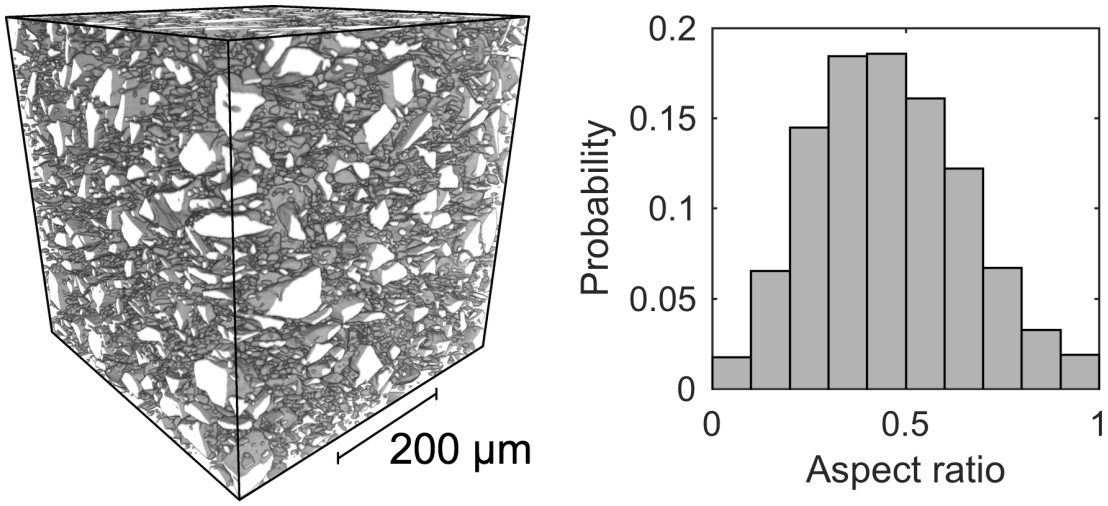


*Figure 5. (Left) 3D micro-CT image of one of the compacted samples with only quartz grains shown; (right) the distribution of quartz grains by aspect ratio.*

*Table 3. Parameters of solid constituents.*

| Component | Size, µm | Aspect ratio | Grain density, g/cc |
|---|---|---|---|
| Kaolinite aggregates | < 75 | 0.1 – 1 | 2.61 |
| Smectite particles | < 2 | | 2.60 |
| Grains of crushed quartz | 2 – 150 | 0.1 – 1 | 2.65 |

## PREPARATION OF MIXTURES WITH DESIRED MICROSTRUCTURE

Depending on the target natural rock, it is possible to predefine the microstructure of an artificial silt-clay mixture in order to simulate diagenesis in different environments (e.g. marine or lacustrine sedimentation basins). Two main parameters that control interactions of unconsolidated sediment constituents are the cation composition of the pore fluid and its pH index.

The water solution of 75 g/l KCl is used to prepare samples with aggregated clay microstructure (ACM). In the presence of salt, the double electric layer surrounding kaolinite particles shrinks that leads to their flocculation and aggregation forming larger clay particles and coating quartz grains (e.g. Osipov, 1976). *Figure 6* shows SEM images of kaolinite microaggregates, consisting of oriented individual clay platelets and ultramicroaggregates (i.e. basic associations of few axially aligned individual clay particles), and thick conforming coats on the surfaces of quartz grains.

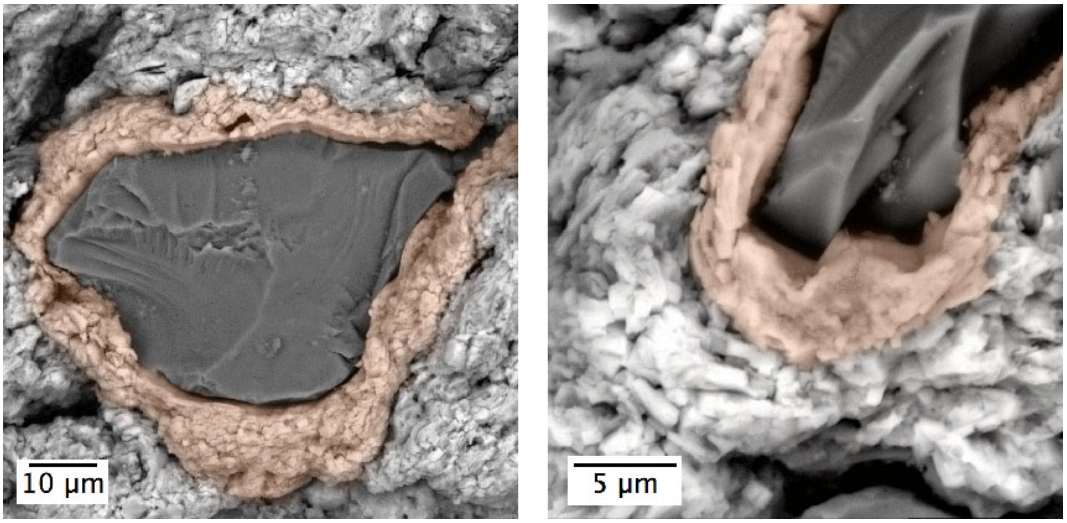


*Figure 6. SEM image of the quartz grains (in dark grey) covered with the coats of conforming kaolinite platelets and aggregates (in orange).*

To prepare samples with dispersed clay microstructure (DCM), the quartz-kaolinite mixtures are boiled with 25 ml of a dispersant, namely, 4% sodium pyrophosphate tetrabasic. During this process, $Na^+$ cations replace other exchangeable cations on the surface of the clay particles and separate existing clay aggregates into ultramicroaggregates and individual clay platelets. Then these large hydrate envelopes of $Na^+$ along the high pH of pore fluid keep the clay platelets separated from each other.

It is important to mention here that the high-pH water solution, corresponding to alkaline medium, also prevents the clay minerals of smectite group from undesired swelling during the compaction experiment.

The detailed process for the preparation of artificial shale samples with desired microstructure is as follows:

- Mineral powders are placed in a drying oven at 105°C for at least 6 hours to assure constant masses;
- The mineral constituents are mixed in a dry state to achieve homogeneous mixture;
- A water solution of desired salinity and pH is used to dilute the mineral mixture and left for saturation for 24 hours: (a) The brine (75 g/l KCl) is added to the quartz-kaolinite mixtures and left for saturation for 24 hours to prepare the ACM samples. (b) The quartz-kaolinite mixture is boiled with 25 cc of 4% sodium pyrophosphate tetrabasic for one hour to prepare the DCM samples. The chemicals used for the preparation clay-silt mixtures are illustrated in Figure 7.


*Figure 7. Chemicals used for the preparation of silt-clay mixtures with a desired clay microstructure.*

Finally, the prepared sample is mixed for another 20 minutes and enclosed inside the oedometric cell by porous alumina plates on either side. The plates are covered

with the filter paper, having a pore size of 2.5 µm, that stops mineral particles and lets fluids to pass through (Figure 8).

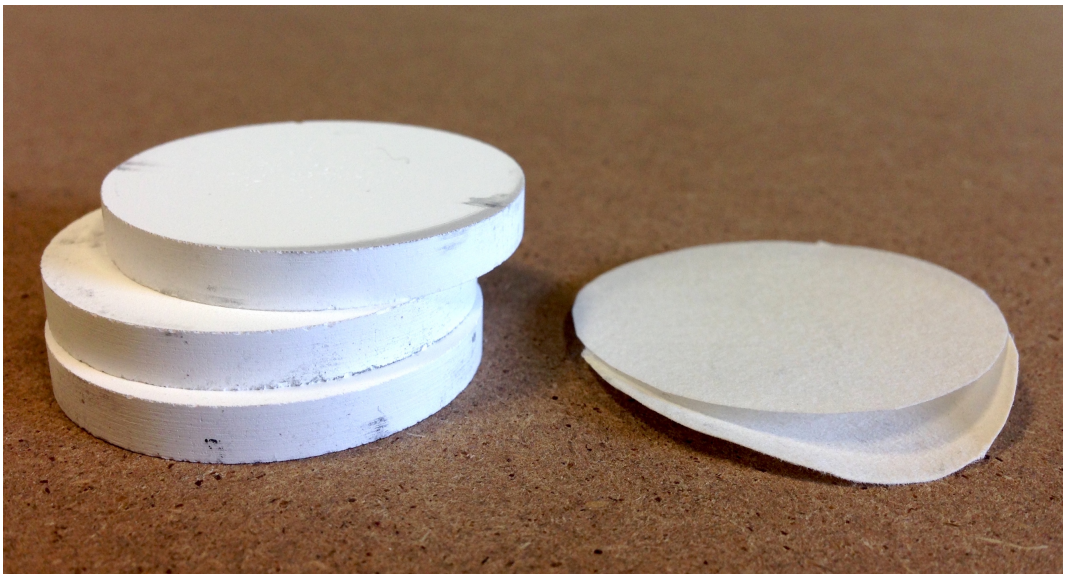

*Figure 8. Porous alumina plates (25% porosity) and filter paper (2.5 µm pore size) used to hold the clay-silt mixtures inside the oedometer.*

## COMPACTION PROCEDURE

Compaction is implemented by steps, where each step consists of three stages:

1. Drained consolidation of the sample under the constant uniaxial stress;
2. Application of the pore pressure equal to the appropriate hydrostatic one;
3. Pore pressure release followed by a residual consolidation of the sample.

During the first stage, the sample porosity is reduced to a predefined value given by:

$$\phi = 1 - \frac{1}{V_0} \sum \frac{m_i}{\rho_i} \tag{1}$$

where $\phi$ is the porosity, $V_0$ (in cc) is the initial bulk sample volume estimated as the volume of the inner cylindrical part of the oedometer cell enclosed between the porous plates, $m_i$ (in g) is the mass of $i^{\text{th}}$ mineral component of the mixture, and $\rho_i$ (in g/cc) is its grain density obtained with the gas displacement methodology (ASTM, 2008).

At each step of the compaction experiment, stress values and the deformation of a sample are registered in the experimental journal. Permeability and ultrasonic measurements take place at each stage of the compaction, when a deformation reaches the stabilization criterion (absolute deformation of a ~25-mm height sample is less than 0.01 mm for 4 hours) and there is no flux in and out of the reservoirs connected to the sample.

When the targeted minimal porosity is reached, the sample is gently ejected from the oedometer, then waxed (Figure 9) and preserved from major desiccation in desiccator at 98% of relative humidity.

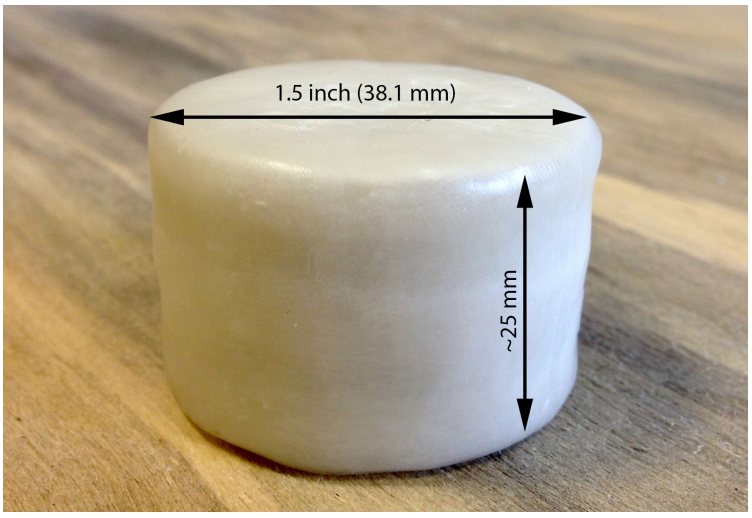


*Figure 9. Compacted artificial shale sample preserved in wax for further analysis of microstructure and dielectric properties.*

## ACQUISITION OF TRAVEL TIMES

Olympus square wave pulser/receiver (model 5077PR) is used to excite the ultrasound waves in all pairs of high frequency transducers. The parameters shown in Figure 10 are used to achieve the best quality signals and minimize the damage to the transducers. Polling rate frequency is set to 100 Hz, that allows acquiring enhanced cumulative signal by averaging of 512 waveforms in ~5 seconds.

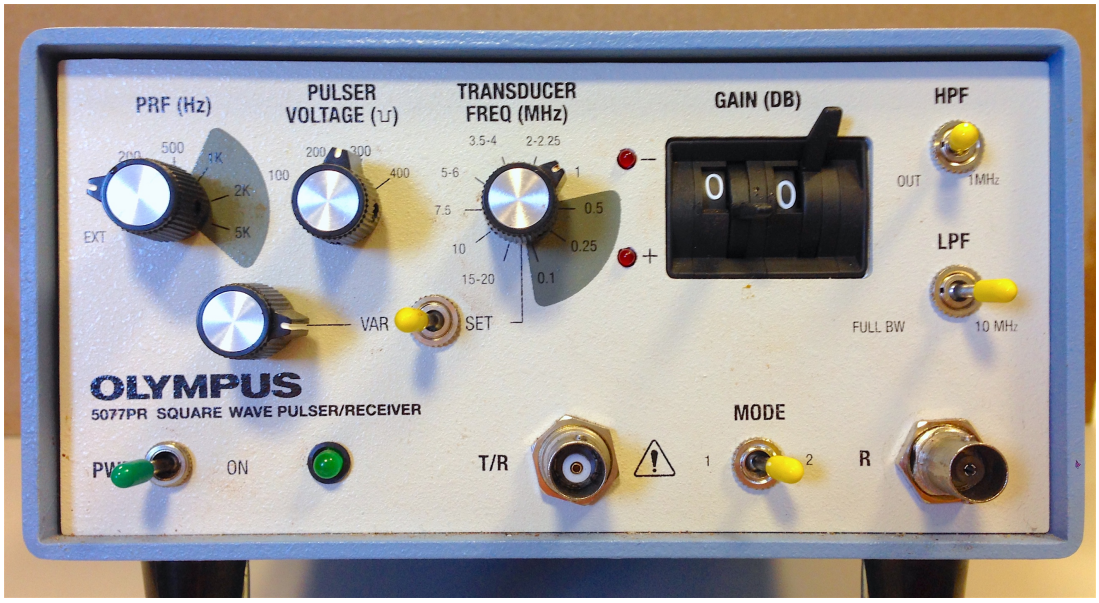


*Figure 10. Square wave pulser/receiver (Olympus 5077PR) used for excitation and registering of ultrasonic pulses with typical setup parameters shown.*

Pulser voltage is usually set to the value of 300 mV as recommended by the transducers' manufacturer. Although the natural frequency of transducer's piezoelectric is specified as 1 MHz, the transducer frequency knob is adjusted manually to correspond to the actual lower frequency of a propagating wave. For example, registered S-wave frequency may degrade up to ~0.1 MHz when the sample is poorly consolidated. The width (period) of a voltage square wave pulse, exciting the oscillations in piezoelectric, should be adjusted to register the strong S-wave amplitudes by constructively interfering the elastic waves produced at the beginning and the end of the square pulse. Signal gain is adjusted at each step of the compaction to be sufficient for registering a weak signal (e.g. at the beginning of the compaction) and to not exceed the dynamic range of the oscilloscope thereby avoiding clipping of the strong amplitudes. Analog high-pass filter is deactivated to preserve the lower frequencies of the transmitted wave as the transducers have a wide bandwidth ranging

from ~0 to 2 MHz. Analog low-pass filter is enabled to attenuate the undesired noise at frequencies above 10 MHz thereby avoiding aliasing effects.

Ultrasonic signals are recorded with digital oscilloscope (Figure 11) using the pulse transmission technique (Birch, 1960). A time window of 400 µs (starting exactly at the trigger time) is selected to record the signal of sufficient length to capture both P- and S-wave arrival times for any pair of the transducers. Tektronix oscilloscope allows sampling of this time window at 10000 equally spaced intervals which provides the necessary sampling frequency of 25 MHz (exceeding that of the low pass analog filter by 2.5 times) to avoid aliasing of high frequency noise into the lower frequency range containing the signal of interest. Signals are recorded to a flash memory for further processing.


*Figure 11. Digital oscilloscope (Tektronix TDS 3034C), capable of recording 10000 equally spaced time samples with maximum frequency of 300 MHz and 512 level averaging.*

## SIGNAL PROCESSING TECHNIQUES

Figure 12 illustrates the typical whole set of waveforms recorded during the compaction experiment with a pair of S-wave ultrasonic transducers and their corresponding envelopes. Although each waveform is an average of 512 signals still some random noise is present. Also the first arrivals of S-waves are strongly contaminated with coherent noise represented here by multiples of P-waves. These negative effects may result in erroneous and thus unreliable detection of first-break arrivals if the manual picking approach is employed.

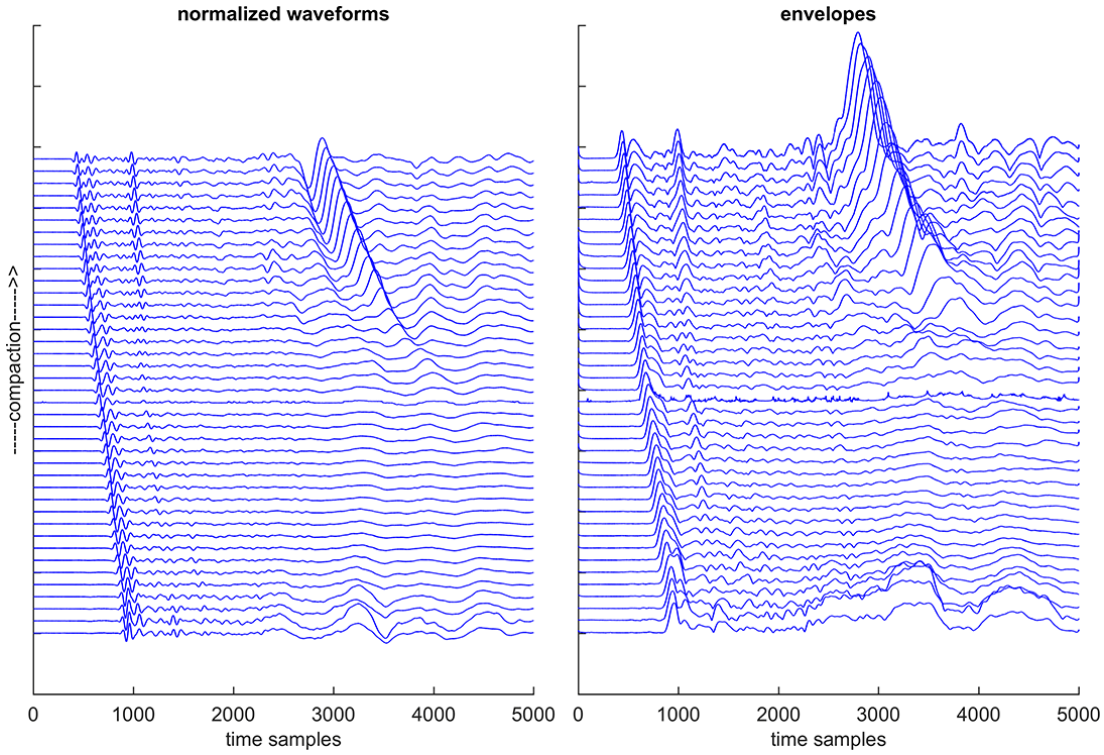


*Figure 12. (left panel) Waveforms recorded with a pair of S-wave transducers during the mechanical compaction and (right panel) their corresponding envelopes. Waveforms and envelopes are normalized by the first break arrivals for ease of visual interpretation.*

Hence, several digital signal processing techniques were tested and adopted for the precise semi-automatic detection of P- and S-wave onset times. These techniques are mainly implemented to remove human factor and acquire statistically reliable first-break picks of both P- and S-waves for the following estimations of elastic properties.

**Automatic P-wave picking algorithm**

The picking of P-wave onset times is first approached by the Short-Term Average over Long-Term Average (STA/LTA) method. For the time series $x_j$, equations for STA and LTA are given by

$$\mathrm{STA} = \frac{1}{ns}\sum_{j=i}^{i+ns} x_j, \tag{2}$$

$$\mathrm{LTA} = \frac{1}{nl}\sum_{j=i-nl}^{i} x_j, \tag{3}$$

where $ns$ and $nl$ are the numbers of input discrete time samples for the calculation of STA and LTA, respectively. Here the STA is sensitive to quick amplitude changes whereas the LTA is representative of the background noise. According to the causality principle, LTA window should precede the STA window. Overlap between the two should be avoided to preserve their statistical independence. Once the STA and LTA are computed the first-break time is selected as a maximum of the derivative of STA/LTA curve.

The window lengths chosen for estimation control the performance of STA/LTA. Appropriate window lengths are selected with respect to the frequency content of the signal of interest and the sampling frequency. From a number of tests the highest accuracy was obtained by selecting a short-window length equal to or slightly greater than one period of the signal oscillation, which is given by:

$$ns = f_s/f_o, \tag{4}$$

where $f_s$ is the sampling frequency and $f_o$ is the centroid frequency of the signal of interest. The long-term window length $nl$ is generally 10 times the length of $ns$.

Although there is a variety of spectral decomposition methods that can be used to automatically identify the frequency content of signals, Stockwell-transform was chosen here due to its better time resolution and sensitivity to the frequency content of a signal. It allows separating P- and S-waves in both time and frequency, and their centroid frequencies can be identified at the local maximums of Stockwell transform as shown in Figure 13.

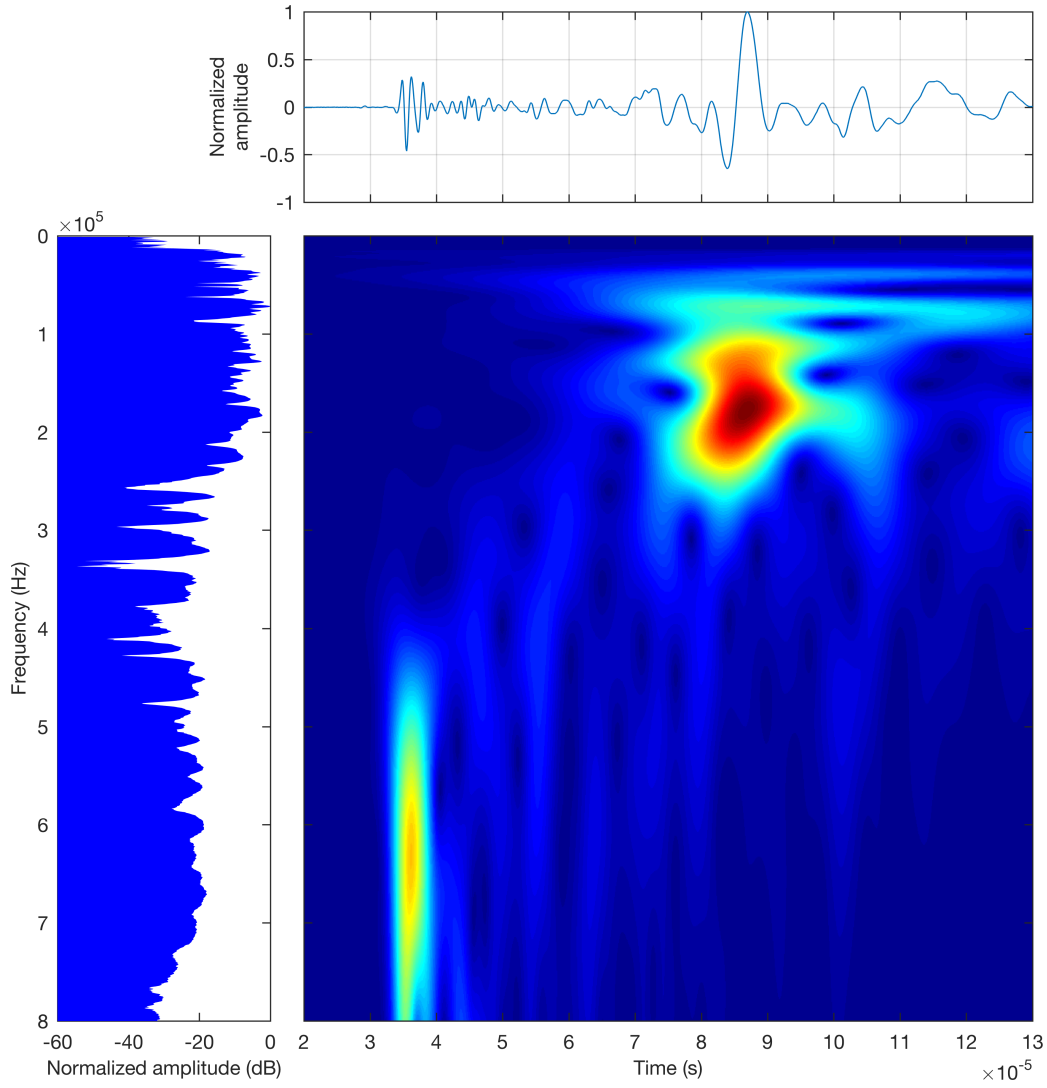


*Figure 13. Raw signal (top panel), its frequency spectrum (left panel) and Stockwell transform showing the variation of absolute signal amplitudes with time at different frequencies (bottom-right panel). Stockwell transform shows clear separation of P- and S-wave energy in time and frequency.*

It was found that the more accurate results are obtained by calculating the STA/LTA on the envelope of a signal instead of its raw waveform. To calculate the signal envelope, the complex analytic signal is first obtained through the Hilbert transform of the raw signal. The continuous form of Hilbert transform $\overline{R}(t)$ of a real time dependent function $R(t)$ is defined as:

$$\overline{R}(t) = \frac{1}{\pi}\int_{-\infty}^{\infty}\frac{R(u)}{t-u}du = \mathcal{H}(R(t)) \tag{5}$$

where $t$ denotes the time and the singularity at $u = t$ is handled by taking the Cauchy principle value of the integral. The Hilbert transform acts like a convolutional filter

introducing a phase shift of $\pi/2$ to a time series. Thus, the envelope time function E(t) can be calculated as an absolute value of a complex analytical signal:

$$\mathrm{E(t)} = \sqrt{\mathrm{R(t)}^2 + \overline{\mathrm{R}}(\mathrm{t})^2} \tag{6}$$

The envelopes of signals recorded by ultrasonic S-wave transducers during a compaction experiment are shown in the right panel of Figure 12. Figure 14 illustrates the raw signal with all the stages of STA/LTA method required to estimate the P-wave onset time.

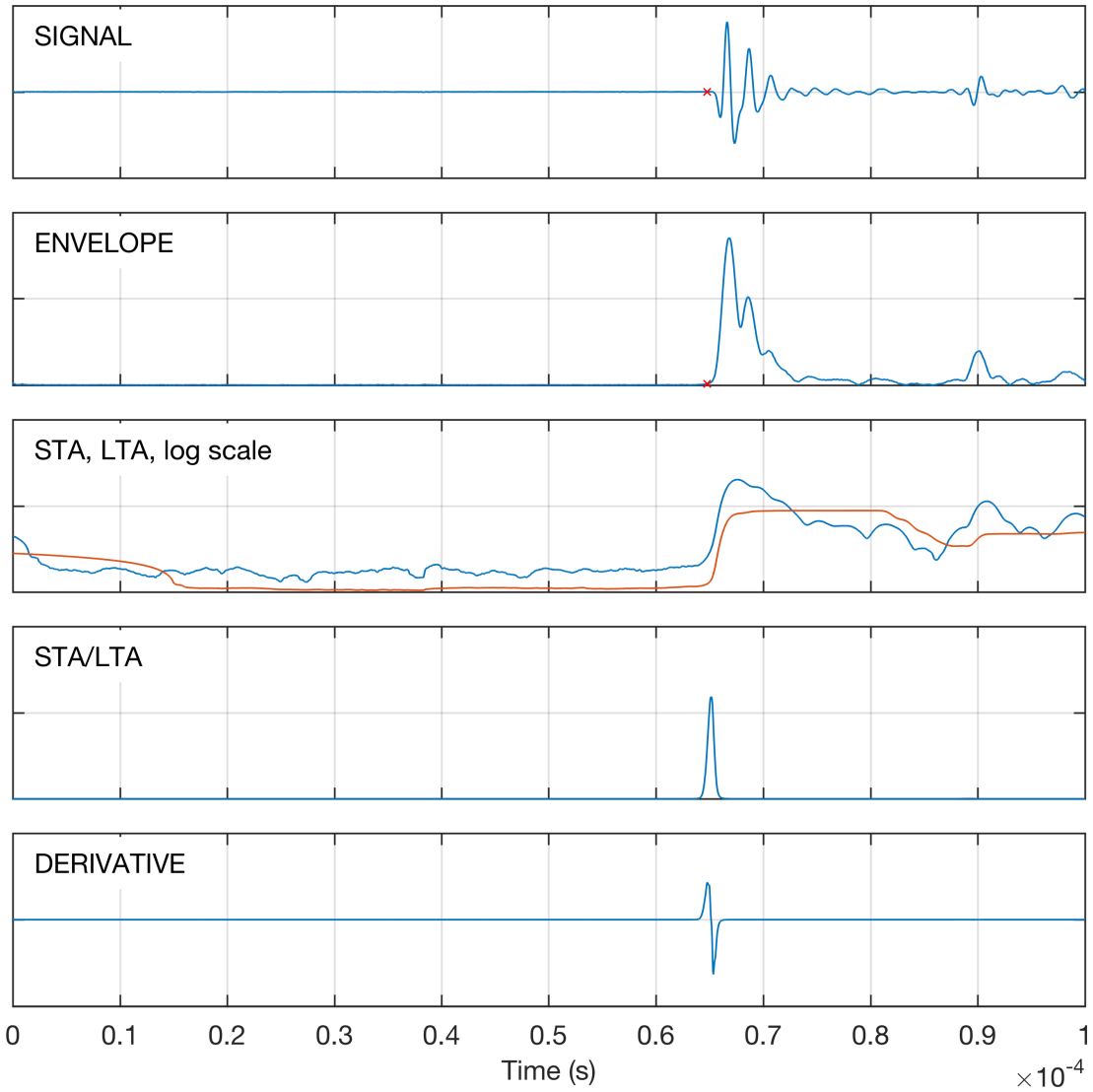


*Figure 14. The consecutive stages of STA/LTA method implementation with the obtained picking shown in the SIGNAL and ENVELOPE panels.*

Although picking obtained by STA/LTA method is of high quality as seen in Figure 15, further enhancement of first arrival detection in the presence of random noise may be achieved by following the application of the statistical Akaike

Information Criterion (AIC) to a short segment of the signal containing the P-wave arrival identified on the previous step.

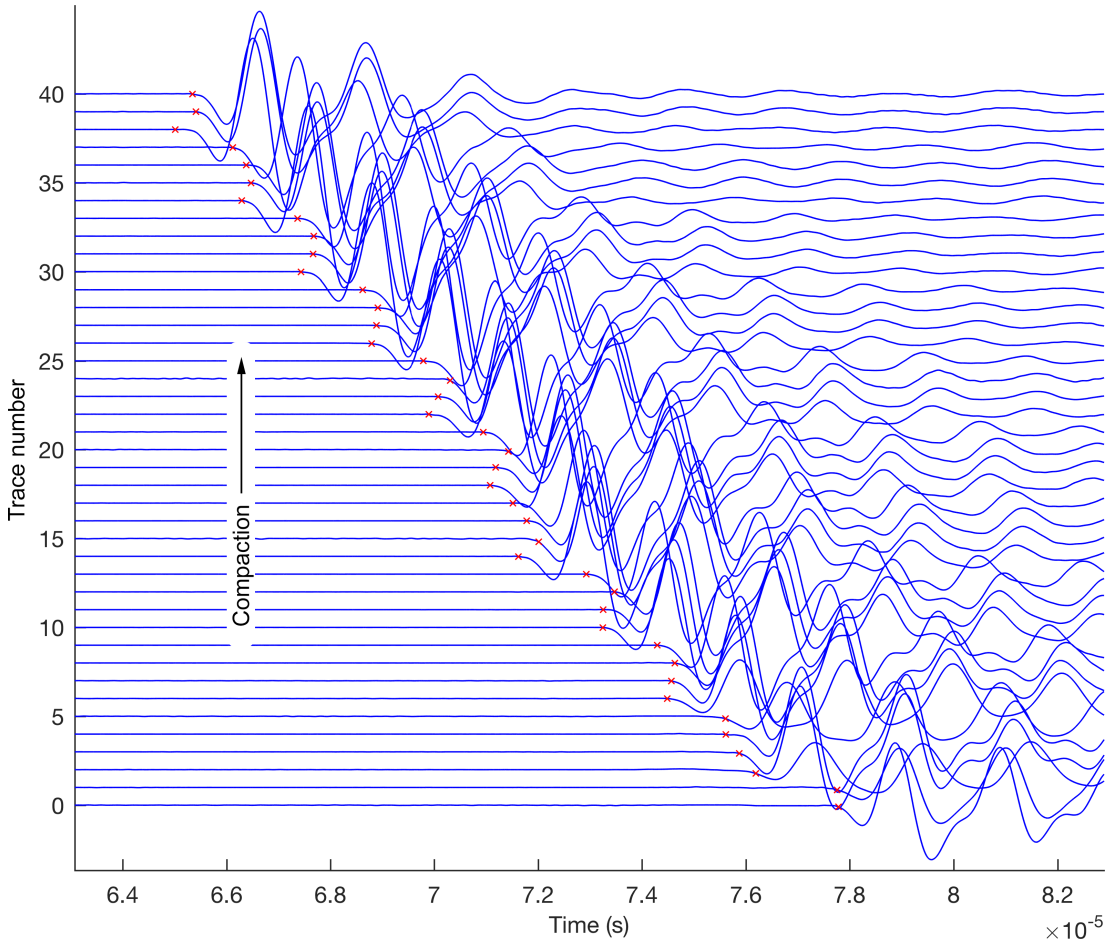


*Figure 15. Example of STA/LTA method implementation for a set of signals recorded with a pair of P-wave ultrasonic transducers at different stages of a compaction experiment. At each stage of the compaction, the P-wave velocity was measured four times: 1) after the drained consolidation, 2) after the application of pore pressure, 3) after the permeability measurements with the pressure-oscillation technique, 4) after the release of the applied pore pressure.*

An autoregressive AIC-picker can also be implemented for the detection of the actual onset time given a time window centred around the approximate P-wave onset. In this case, the envelope is used to prearrange the onset by thresholding. To apply a constant threshold to all signals, each signal envelope is squared and normed. Within the thresholded part of a signal, the exact onset is determined using the AIC-function according to (Krüger et al., 2013):

$$AIC(t) = t\log_{10}(\mathrm{var}\{x(1{:}\,t)\}) + (T - t - 1)\log_{10}(\mathrm{var}\{x(t{:}\,T)\}) \qquad (7)$$

where var is the variance of a given vector. Thus, the AIC function splits the signal in two parts given by vectors $\{x(1:t)\}$ for time 1 to $t$ and $\{x(t:T)\}$ from time $t$ to $T$ expressed in discrete time samples. The essence of the AIC is to characterize the entropy (i.e. information context) by describing the similarity between the two broken parts of the total signal so that the first part contains high-entropy context with uncorrelated noise and the following part includes a low-entropy correlated signal. Thus, the time of the absolute minimum of an AIC function estimated for the selected time window corresponds to the onset of P-wave. Figure 16 demonstrates the use of the AIC arrival time estimation, where a clear improvement is seen compared to an initial guess based on the envelope threshold.

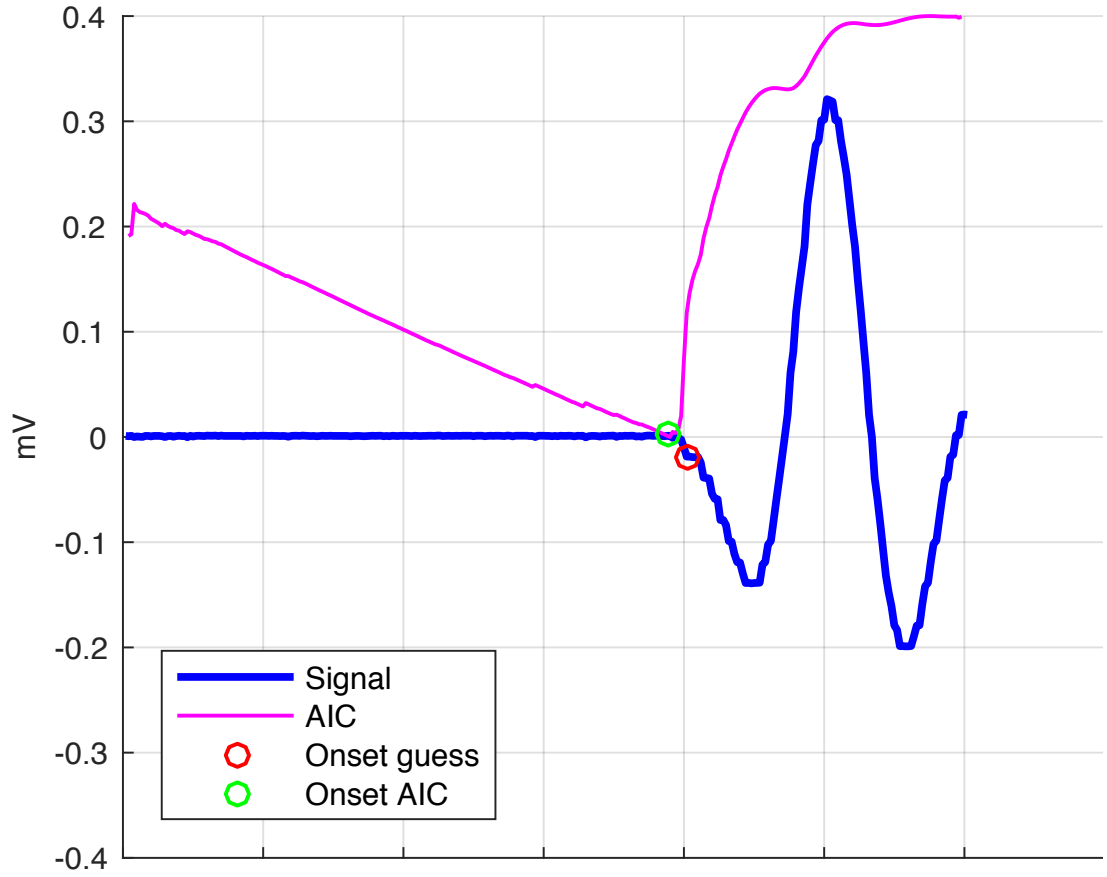


*Figure 16. Example of signal onset estimation using an AIC-based approach. The red circle indicates the initial onset guess for AIC-picker, where the green circle shows the estimated P-wave onset based on the minimum of AIC function.*

The result of AIC picking algorithm applied to the actual waveforms recorded during one of the compaction experiments is shown in Figure 17. The clear improvement in a picking quality is observed. The AIC picking algorithm is very simple and can be utilized independently from the other methods, however best

practise is to apply it after the other robust picking algorithms as it may fail in the presence of coherent noise (e.g. P-wave multiples for the detection of S-wave arrivals).

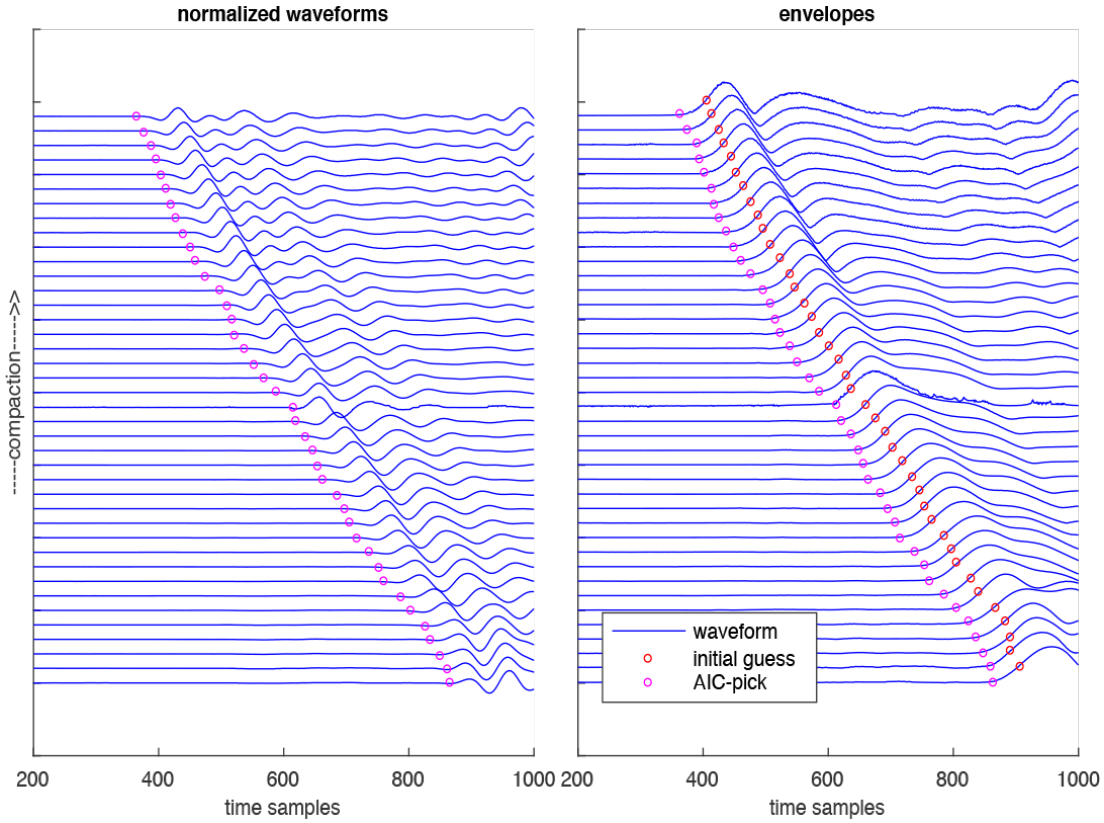


*Figure 17. Waveforms and their envelopes recorded with S-wave transducers during the mechanical compaction. Both panels show the same fragment of the waveforms containing first breaks of P-waves. Red circles show the initial onset guess defined by the threshold of normalized envelopes of the first breaks. Magenta circles show the result of automatic picking acquired by using AIC.*

**Automatic S-wave picking algorithms**

S-wave onset-time picking could be approached differently from the P-wave picking algorithm due to the interfering noise generated by P-wave multiples. Here, the two methods for the estimation of S-wave arrival times in the presence of strong non-random noise are applied: modified energy ratio method (MER) and complex continuous wavelet transform (CWT). MER method is very simple to control and relatively fast whereas the CWT method requires some supervision and refinement but provides the ability to focus on signal features at different frequencies.

It is recommended to process the signal part containing S-wave energy in a window, thereby avoiding picking of P-wave arrivals and its multiples. In highly dispersive samples, the interval of the signal containing an S-wave onset is not readily observable even with the use of the signal envelope. Therefore, I propose to perform Stockwell transform, as described earlier in this section, separating the P- and S-wave arrivals in both frequency and time. Part of the signal containing S-wave onset is then used in MER method. Energy ratio is defined similarly to STA/LTA method having equal window length. The ratio of energies in windows following and preceding the time index $i$ is given by:

$$ER = \sum_{j=i}^{i+ne} x_j^2 \Big/ \sum_{j=i-ne}^{i} x_j^2 \tag{8}$$

If $j < 0$, set $x_j = \frac{x_1 + x_2}{2}$,

If $j > N$, set $x_j = \frac{x_{N-1} + x_N}{2}$.

where $ne$ is the window length expressed in time samples. The onset of the S-wave is then defined as the peak on the energy ratio curve. In the case of a signal strongly contaminated with noise it's recommended to use the modified energy ratio method:

$$MER = \Big(\mathrm{abs}(x_j \cdot ER)\Big)^3 \tag{9}$$

Performance of this method also depends on the window length that can also be calculated using the Equation 4. Similarly, the centroid frequency of an S-wave is derived with Stockwell transform.

An example of the method implementation is shown in Figure 18 for the signal at the end of compaction.

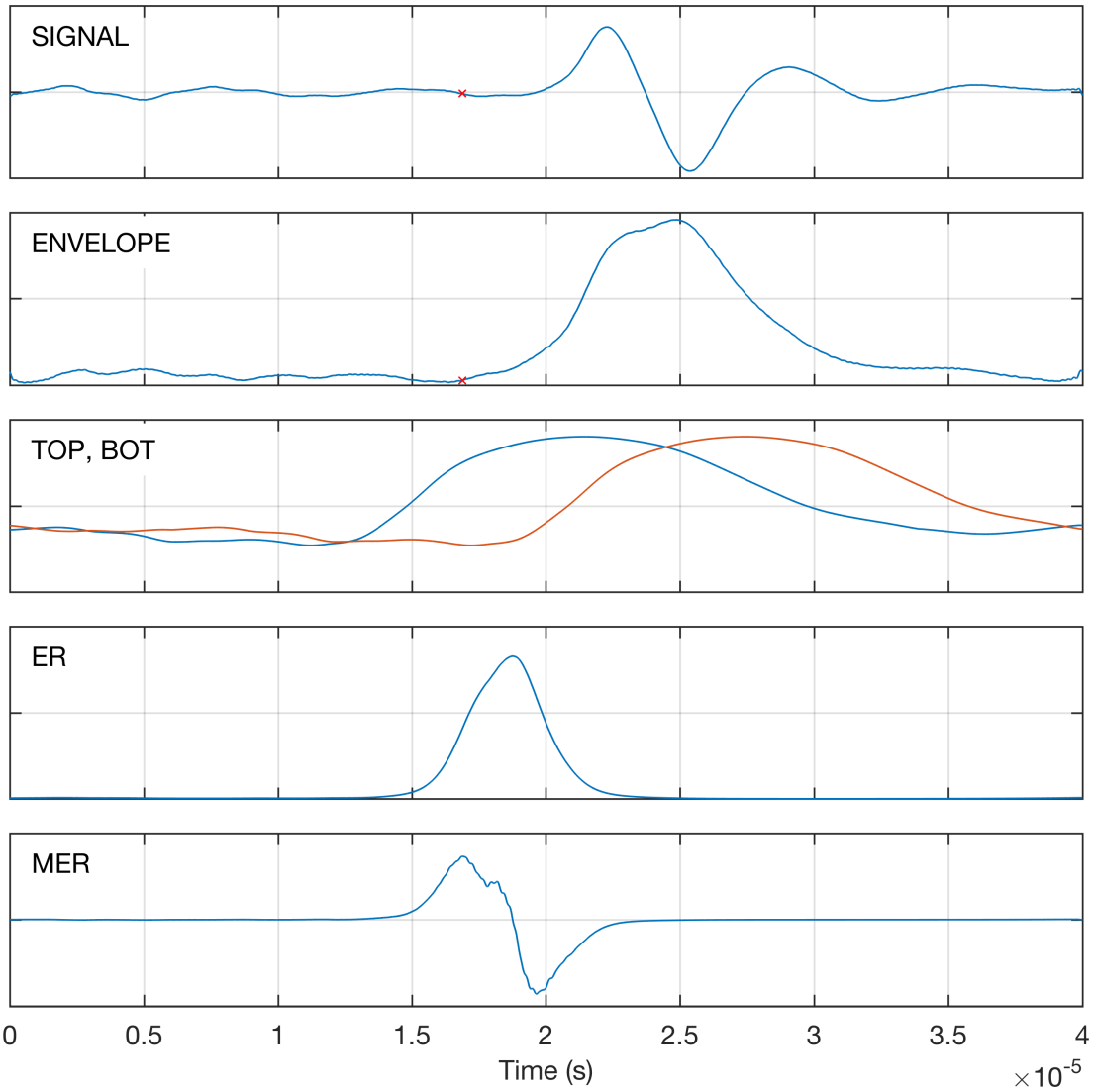


*Figure 18. Example of the MER method for the estimation of an S-wave arrival time. Although one may manually pick the S-wave arrival at a later time (e.g. 2 µs), this will not be correct as can be seen from the envelope of the signal illustrating the earlier arrival of P-wave energy that is precisely picked (red cross) by the MER algorithm.*

The CWT method offers both time and frequency separation of P- and S-wave energies and, therefore, it is more suitable for S-wave onset detection. However, the appropriate wavelet should be chosen to provide the correct picking. Figure 19 illustrates the CWT transformation of the signal recorded with a pair of S-wave transducers at the end of compaction.

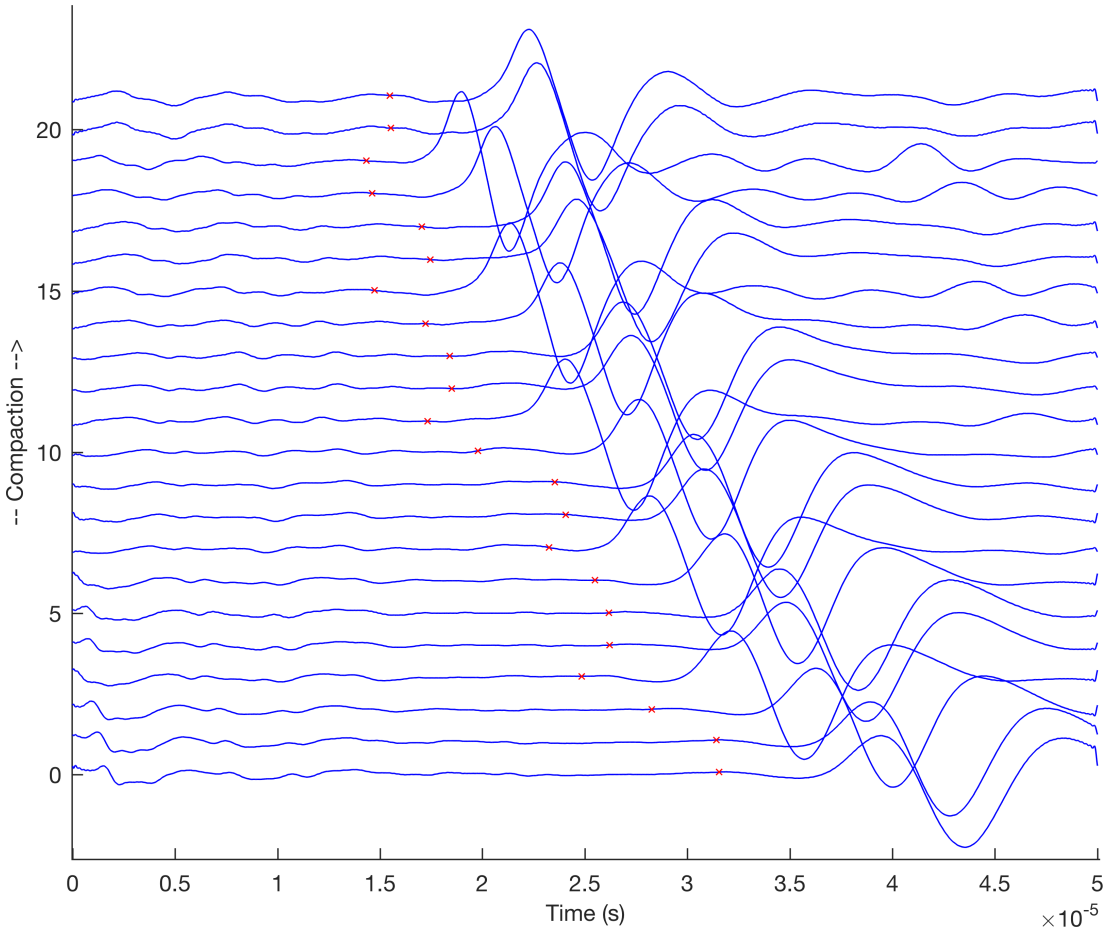


*Figure 19. Example of the energy ratio method implementation for a set of signals recorded with a pair of S-wave ultrasonic transducers at different stages of a compaction experiment.*

The following calculation of the S-wave onset time mainly takes two conditions as a basis. First, it is presumed that when using shear wave transducers, the predominant part of the impulse energy is transmitted with the shear wave and not the accompanying primary wave. Furthermore, the frequency contents of shear and primary waves most likely differ from each other. Meeting these two conditions allows identifying maximum and minimum values in a certain window in a wavelet graph at the extremum values of the induced shear wave (Figure 20). The distance on the time axis between the two extrema corresponds to a half of the oscillation period of a shear wave. For the Gaussian wavelet of order three, subtracting the full length of an oscillation period from the time of the maximum value yields the onset time of the signal.

To reduce calculation time and to avoid picking the P-wave instead of the S-wave it is better to reduce the window in which the extreme values are picked.

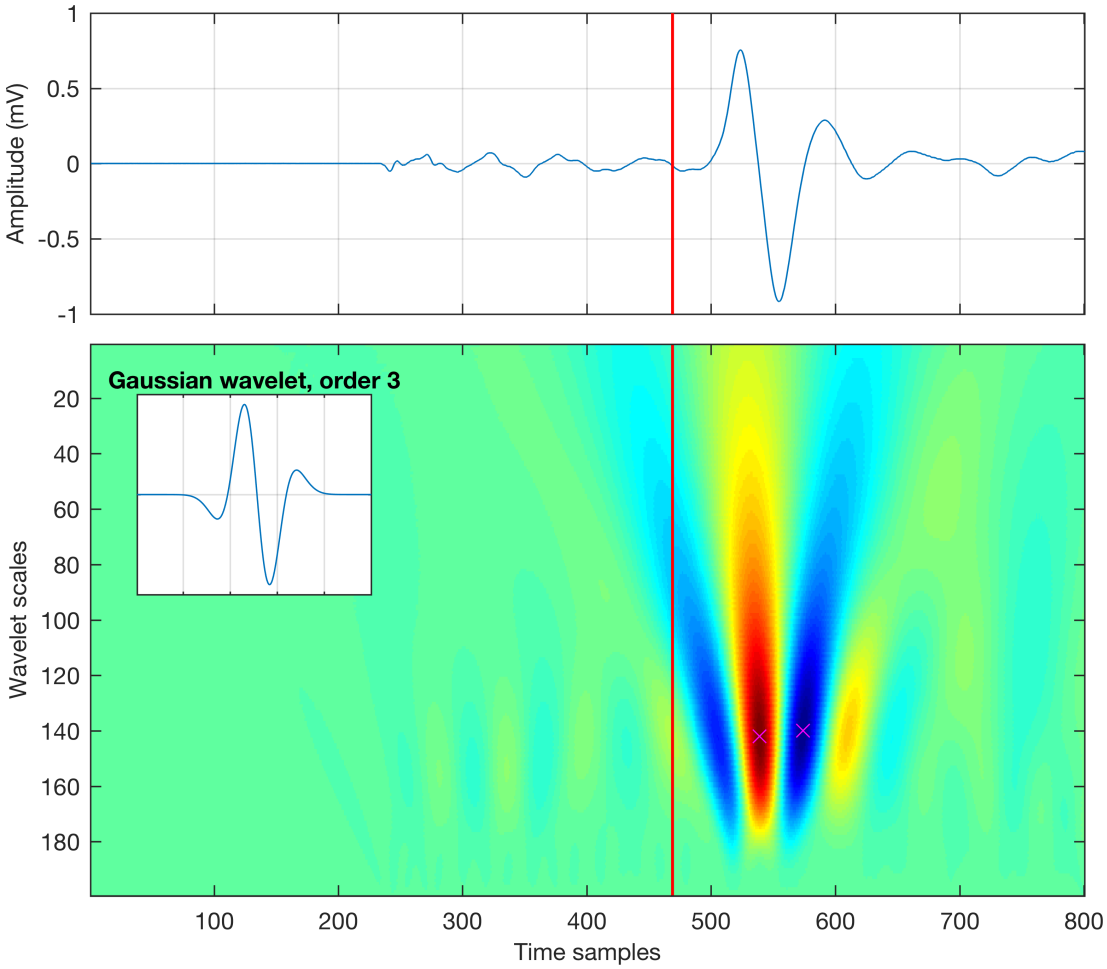


*Figure 20. S-wave arrival-time picking using continuous wavelet transformation (CWT). Unprocessed signal record in the top panel, and the CWT of the signal in the bottom panel. Gaussian wavelet of order 3 is used. Crosses on the CWT plot show the maximum correlation of the wavelet with the negative and positive amplitudes of the S-wave signal. The red line illustrates the estimated S-wave onset.*

The signal processing algorithms described in this chapter have been designed, tested, and applied to a set of recorded ultrasonic signals acquired during the compaction experiments described in Chapter 4 of the thesis. I found that the most stable, precise, and easy to implement picking is obtained with the use of STA/LTA and MER algorithms for automatic detection of P- and S-wave onsets, respectively. However, the described AIC and CWT algorithms might be used to further improve the picking quality and tackle noise-contaminated signals. To conclude automated picking algorithms should be used to reduce the uncertainty in ultrasonic velocity measurements as they provide more precise and statistically reliable results compared to the manual picking.

## ESTIMATION OF ELASTIC PROPERTIES

To estimate the velocities within the sample, it is necessary to account for the wave propagation through the parts of the compaction oedometer device. Therefore, the travel times within the sample are estimated as the difference between the onset time of elastic waves obtained with the picking of the recorded ultrasonic signal and the calculated travel times within the material of the setup components laying on the path of propagating elastic wave. Herewith the deformations of the pistons and the delay times of transducers are taken into account, while the deformation of the oedometer cell normal to the direction of a compaction stress is negligibly small ($< 0.01$ mm) and is not considered. Phase velocities of P- and S-waves are easily evaluated for horizontal and vertical directions by dividing the chosen dimension of a sample by the calculated time of wave propagation within the sample in that direction.

In the experiments, I only able to measure the group angular velocity within the sample as the distance between transducers is significantly larger than their diameter (Dellinger and Vernik, 1994). Angular phase velocity is calculated from the measured group one as suggested by Miller et al. (2012).

## PERMEABILITY MEASUREMENTS

For permeability measurements, I use the pressure-oscillation technique that is comprehensively described in the works of Song and Renner (2007), Bernabé et al. (2006), Fischer (1992), Kranz et al. (1990) and summarized by Hasanov (2014). Schematics of the experimental setup for permeability measurements is shown in Figure 21. A sample chamber is connected to the upstream and downstream reservoirs at its top and bottom faces respectively. Prior to the experiment reservoirs are connected through the valve between them; this allows equilibrating the initial pore pressure within the sample and both reservoirs.

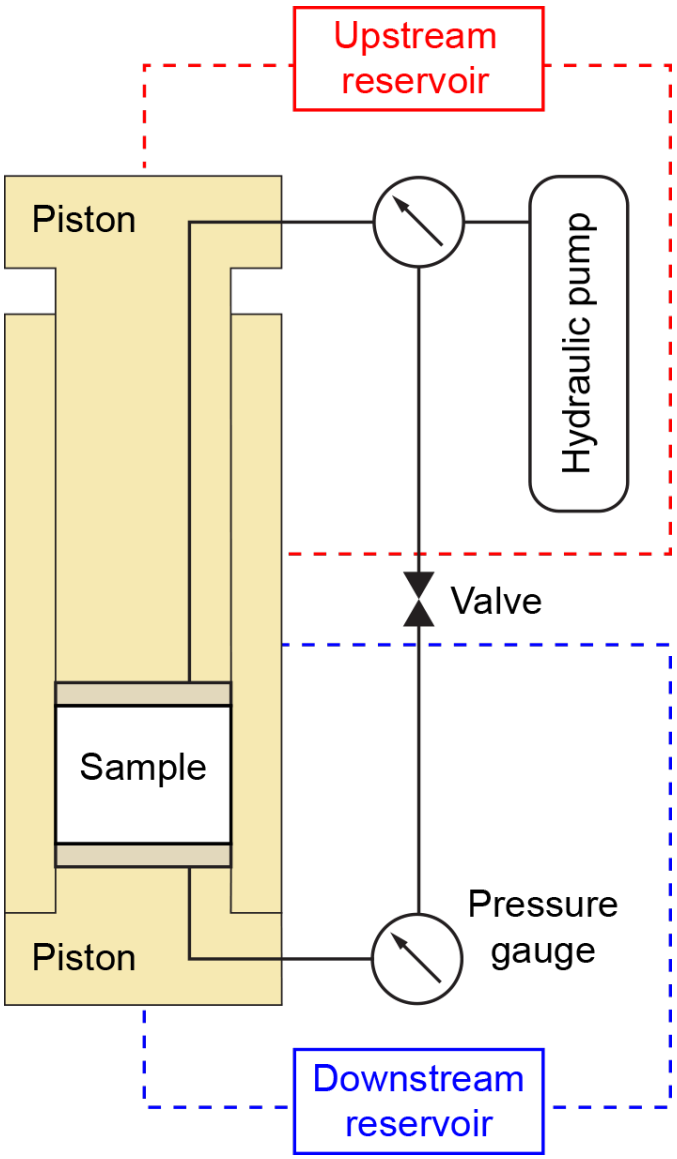


*Figure 21. Principle scheme of the experimental setup used for permeability measurements via pressure-oscillation technique.*

After the equilibrium is reached the valve is closed to ensure the independent monitoring of input and output pressure changes in upstream and downstream reservoirs, respectively.

The pump connected to the upstream reservoir is programmed to induce the harmonic pressure oscillations given a discrete sinusoid (Figure 22) in the following form:

$$P_U = A_U \sin\,(2\pi f_o t_s n), \tag{10}$$

where $A_U$ is the pressure oscillation amplitude in the upstream reservoir set to be equal 5% of the initial steady state pore pressure within the sample at a given compaction step. $2\pi f_o$ is the oscillation frequency in radians per second and $f_o$ is the oscillation frequency in Hz. $t_s$ is the sampling period in seconds, and $n$ is an integer time index in a range of 0 to $N$, where $N$ is the length of one full period of oscillation in time samples.

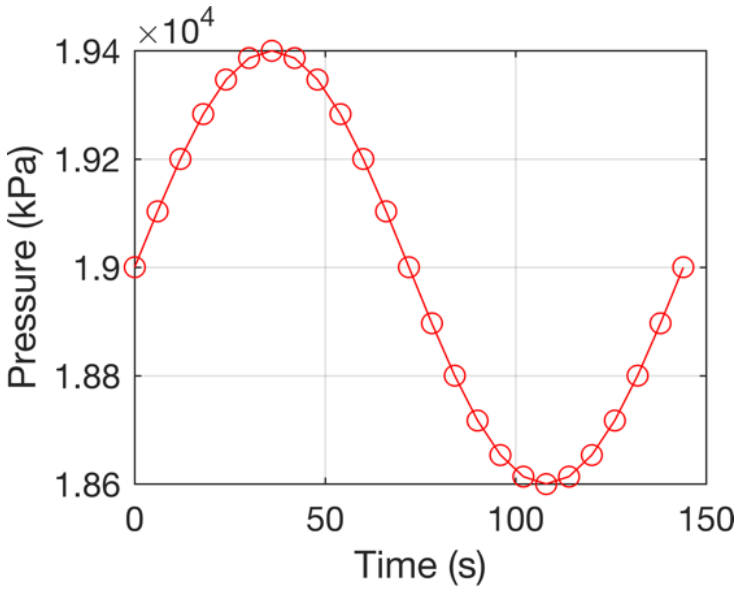


*Figure 22. Example of an oscillation program for the pump in a form of a discrete sine with the period of 144 s and amplitude of 400 kPa. The solid line represents the desired sine oscillation while the circles are the actual discrete pressure values used to program the pump.*

The period of an oscillation is set to be sufficient for registering the oscillation at the downstream reservoir $P_D = A_D \sin\,(2\pi f_o t_s n + \theta)$. Although short oscillations are desirable, it is not always possible to register harmonic pressure change at the downstream reservoir due to the fast decay of a pressure pulse amplitude with the

increase of frequency as illustrated in Figure 23. Thus, the frequency ($f_o$) of the input pressure oscillations is chosen experimentally for each compaction step.

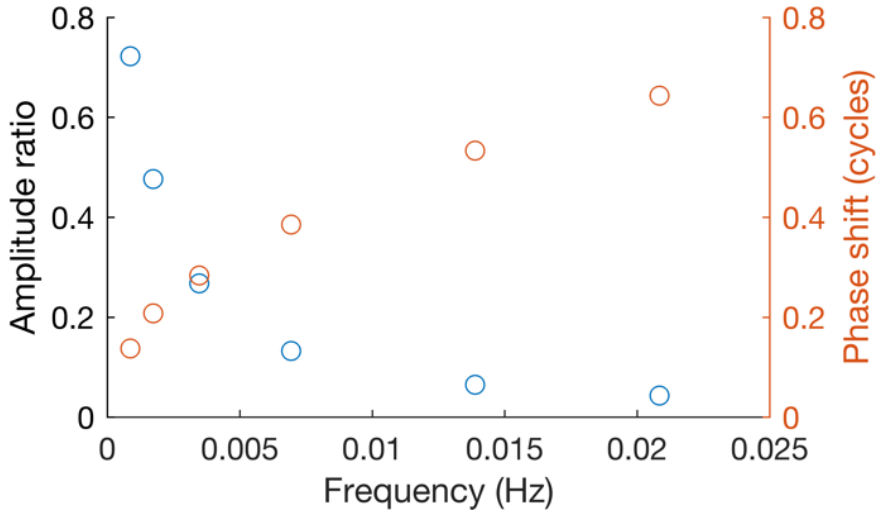


*Figure 23. Evolution of the amplitude ratio* $(A_r)$ *and the phase lag* $(\theta)$ *between the recorded upstream and downstream pressure oscillations with the increase of frequency obtained for the same sample at the same compaction stage.*

Further enhancement can be done to simplify the search of the upstream oscillation frequency and, if possible, improve the estimation of hydraulic properties. It is proposed to excite the cumulative pressure oscillation in the upstream reservoir. This cumulative oscillation is simply a sum of discrete sine waves of different frequencies having a whole number of periods in a given time interval (Figure 24). Therefore, if high-frequency oscillation attenuates significantly, it is still possible to register the lower frequency amplitudes at the downstream reservoir. In the case where the multiple oscillations of different frequencies are registered the statistical reliability of the method may be enhanced through averaging of the obtained amplitude ratios and phase lags.

Further hydraulic properties of a sample are calculated from the amplitude ratio ($A_r = A_U/A_D$) and phase lag ($\theta$) between the pressure oscillations in upstream and downstream reservoirs (*Figure 25*). To this end, a few tens of oscillations are recorded and the first few cycles in which the phase shift and amplitude ratio are unstable are discarded. The rest of the signals is processed in the frequency domain to supress the noise and accurately obtain the amplitude ratio and the phase lag.

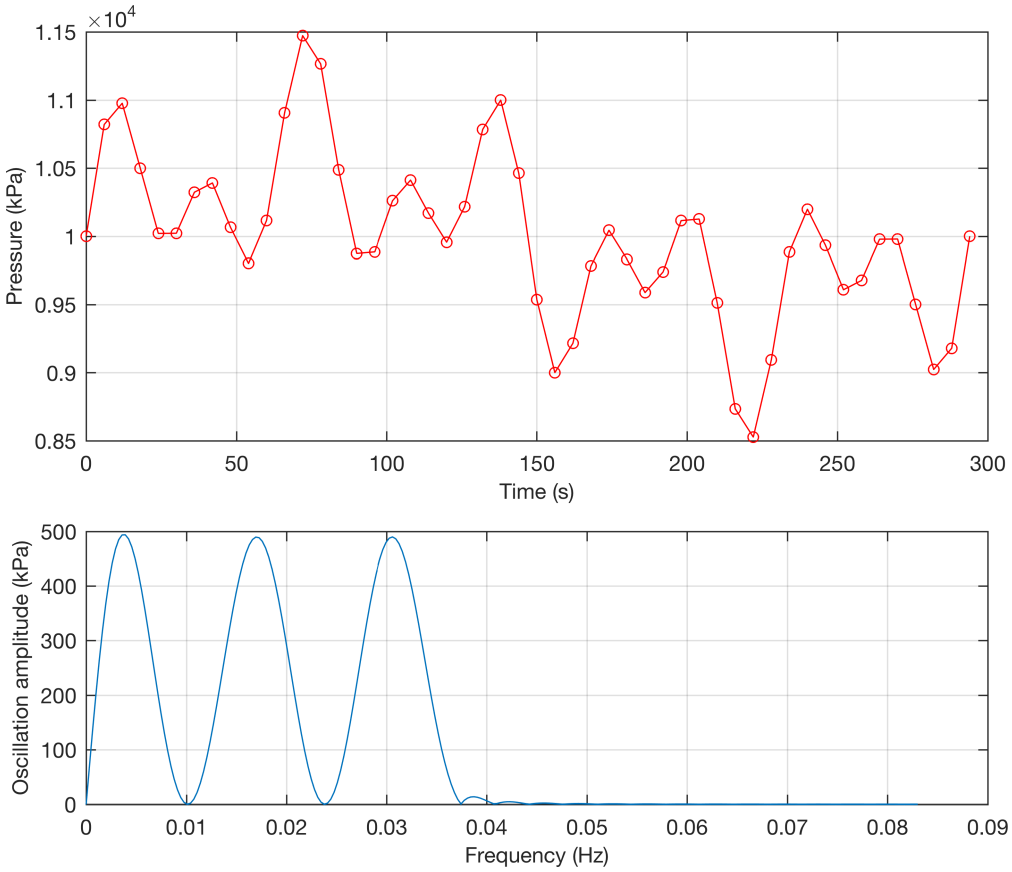


*Figure 24. (Top panel) Cumulative oscillation program composed of three sine waves with different frequencies. (Bottom panel) Frequency magnitude response of the cumulative oscillation.*

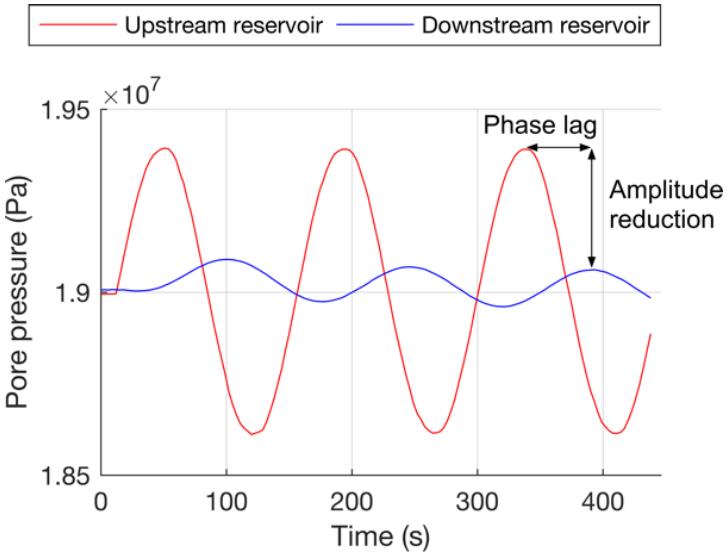

*Figure 25. Pressure oscillations in the upstream and downstream reservoirs versus time. The significant amplitude reduction and phase lag are clearly visible between the harmonic pressure records.*

The analytical solution for the pressure diffusion equation is given by Bernabé et al. (2006) in the following form:

$$A_r e^{-i\theta} = \left( cosh\left[\sqrt{\frac{\xi}{\eta}}(1+i)\right] + \frac{1+i}{\sqrt{\xi\eta}} sinh\left[\sqrt{\frac{\xi}{\eta}}(1+i)\right]\right)^{-1}, \quad (11)$$

where $A_r$ and $\theta$ are the experimentally obtained amplitude ratio and phase lag, respectively. The dimensionless parameters: storage capacity $\xi$ and permeability $\eta$ in Equation 11 are defined by

$$\xi = \frac{AL\beta_{st}}{\beta_d}, \eta = \frac{2Ak}{\omega L\mu\beta_d}, \quad (12)$$

where $A$ is the sample cross-section area, $L$ the sample length, $\beta_{st}$ the sample storativity, $\beta_d$ the downstream reservoir storage, $k$ the sample permeability, and $\mu$ the dynamic viscosity of the pore fluid. To obtain permeability, Equation 11 is solved numerically to derive the dimensionless permeability and storativity by minimizing the mismatch function of the following type

$$C(\xi_i, \eta_i) = w\left[\frac{\log10(A_{ri})}{\log10(A_r)} - 1\right]^2 + (1-w)[\theta_i - \theta]^2, \quad (13)$$

where $w$ is a weight assigned the value of 0.5, $A_{ri}$ and $\theta_i$ are the parameters calculated with Equation 11 on a numeric grid defined by $\xi_i$ and $\eta_i$, and $i$ is an index number of a grid element. In my experiments, the estimated dimensionless storativity is estimated as ~-0.1 for all the samples due to the small volume of the downstream reservoir compared to the volume of a sample. This value of the dimensionless storativity doesn't fall within the physical range of the solution space plot (Figure 26) of the pressure diffusion equation, which makes it impossible to estimate the storage capacity of the samples. However, the permeability can still be determined accurately, using the Equation 12 for the dimensionless permeability.

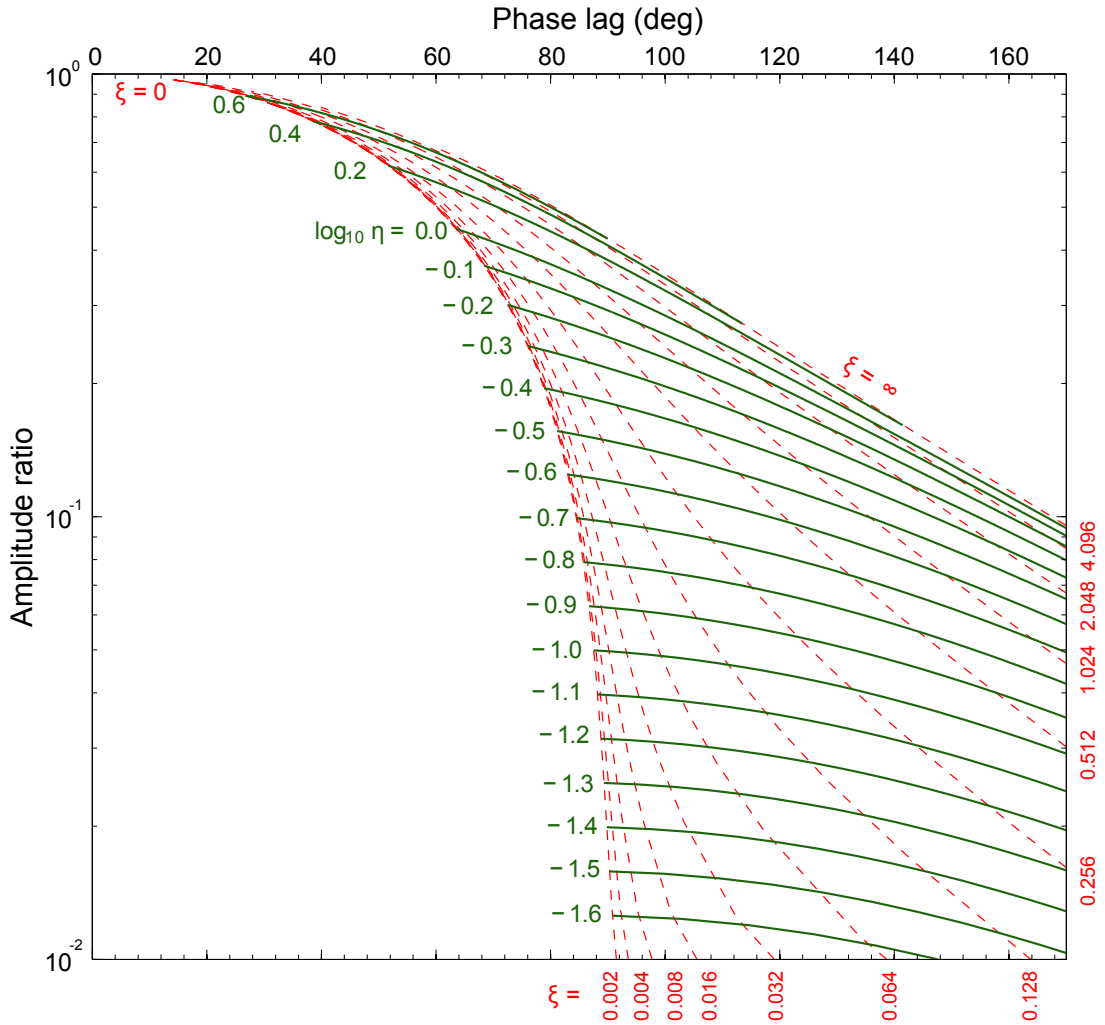


*Figure 26. Solution space of the pressure diffusion equation (modified from Hasanov (2014).*

## MICROSTRUCTURE CHARACTERIZATION

Subsamples for SEM and micro-CT analysis are cut from the central part of the compacted samples. A cylindrical subsample with the length of ~5 mm and diameter of ~1.5 mm is used to acquire 3D microtomographic images with high resolution (up to 0.6×0.6×0.6 $\mu m^3$) on a micro-CT scanner XRadia VersaXRM-500. Analysis of the micro-CT images is performed with "Fiji" software (Schindelin et al., 2012) to obtain shape preferred orientations (SPO) of quartz particles. The quartz grains are first segmented from each image, using "Trainable Weka Segmentation" plugin, and their shapes are approximated by ellipsoids using "BoneJ" plugin (Doube et al., 2010). To plot SPO of quartz particles by the angle from the bedding plane, I calculate the angle between the longest axis of each ellipsoid and the symmetry axis (normal to bedding) of the sample.

The preferred orientation of clay particles within the compacted samples was measured using the neutron diffraction spectroscopy using the fact that crystallographic c-axis is normal to the clay platelet basal plane (Figure 27). Therefore, the crystal preferred orientation (CPO) of clay platelets is also a proxy for its SPO. The micro-CT analysis cannot be used for that purpose as the particle size of clay minerals is on the edge of micro-CT scanner resolution.

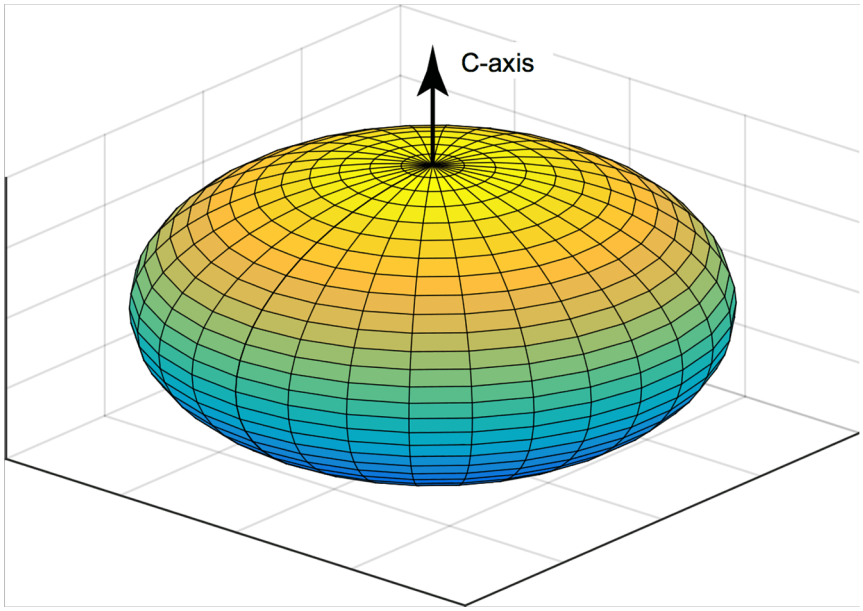


*Figure 27. Schematic model of a clay aggregate having the shape of an oblate spheroid with its C-axis oriented normal to the basal plane.*

The orientation distribution function of clay component is performed on the residual stress and texture diffractometer KOWARI at the OPAL research reactor

(Bragg Institute, ANSTO, Australia). The neutron wavelength ~2.84Å is used to measure primarily kaolinite (002) reflection (basal plane) at 47° using the position sensitive detector. Since the detector has 15°-coverage in both horizontal and vertical dimensions, as a by-product quartz (100) diffraction peak is also measured.

Samples for the neutron experiment are cubes of 10×10×10 $mm^3$ extracted from the compacted artificial shales. This size is a compromise between maximizing diffraction signal (requires increasing volume) and minimizing neutron absorption effects (requires reducing volume). Neutron absorption has to be taken into account because of the hydroxyl ($OH^-$) groups abundant in clay minerals.

In a textured sample, upon rotation of the sample the overall diffraction peak intensity changes and from these intensity variations for different lattice planes the pole figures in the sample coordinate system can be obtained. In my experiments, a two-circle Eulerian goniometer is used to rotate a sample during measurements through the angles $\chi$ and $\phi$ with 5° steps which after later transformations into coordinate system of the sample results into full pole figures with polar coordinates $\alpha$ and $\beta$ with close to regular 5°×5° mesh (Figure 28).

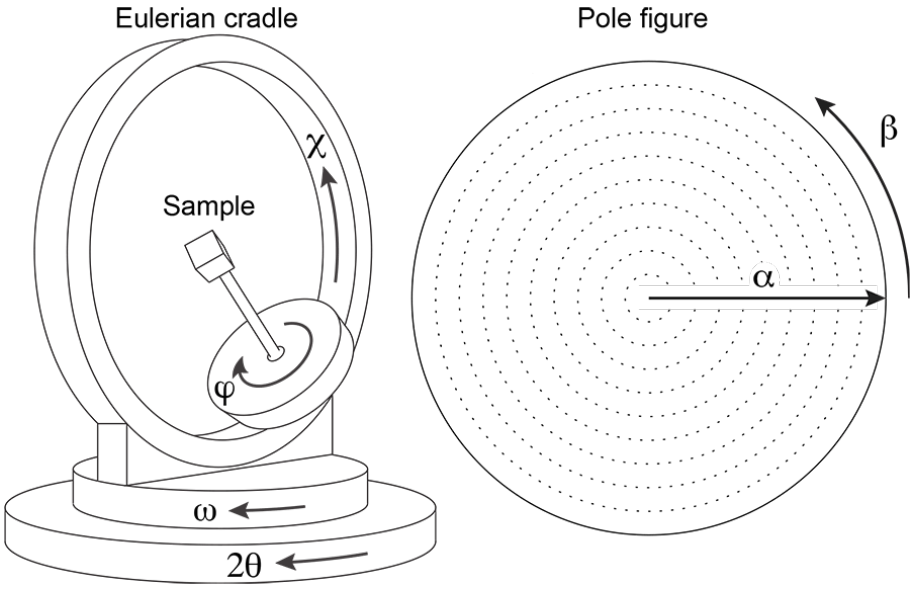


*Figure 28. (Left) Eulerian cradle with the rotation axes φ, χ; (right) scanning grid of a pole-figure with the corresponding polar angles α, β. Modified from Hofler et al. (1988).*

The experimental pole figures are corrected for small misalignments of samples (when cutting them and mounting to the goniometer) and cylindrical symmetry is imposed to reduce 2D distributions (pole figures) to 1D distributions (angular plots) also improving the quality of data and its statistical reliability.

The described set of methods was used in chapters 3, 4, and 5 of the thesis to characterize the mineral components of artificial shales and to quantify the parameters of the microstructure of compacted samples. Experimental pole figures obtained with the neutron diffraction goniometry were used to derive the orientation distribution functions of clay minerals needed for the modelling of anisotropic elastic and dielectric properties of shales.

## DIELECTRIC MEASUREMENTS

The anisotropic dielectric properties of shales were measured in a parallel plate dielectric rig (Figure 29). Parallel plate dielectric measurements (Von Hippel, 1954) are ideal in a frequency range from 10 kHz up to 110 MHz.

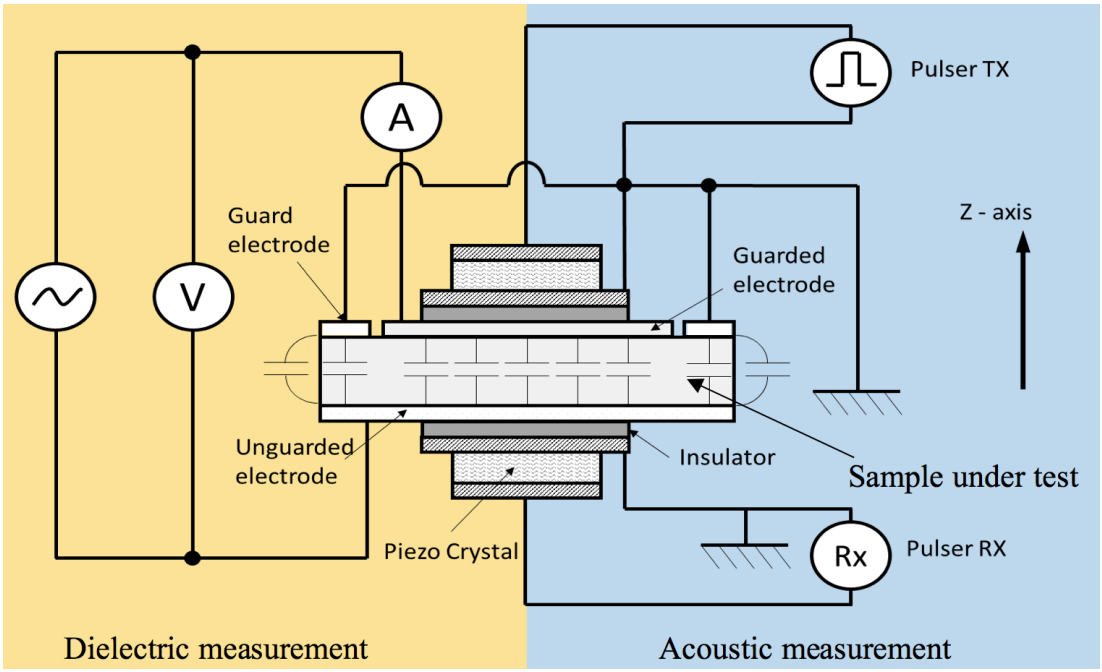


*Figure 29. Principal scheme of the parallel plate measurement setup, modified from (Josh, 2017).*

Two subsamples were cut from each of the compacted samples in two perpendicular directions: parallel and normal to the bedding plane. To ensure the proper coupling between the electrodes of the measurement cell and maintain a parallel electric field normal to the faces of the subsample disc, it was polished on a diamond surface grinder to achieve the parallel faces with 30 μm tolerance. The thickness of an average sample should not exceed one fifth of its diameter. The subsample discs were each placed in the parallel plate measurement cell where they were measured with an impedance analyzer. The two following methods for running this device were employed. The bare coupling was used to measure the effective conductivity of the compacted samples. The disc subsample is simply placed between the parallel plate electrodes so they are in direct contact with the bare faces of the subsample. For shales, this method provides a good conductive coupling between the rock surface and the electrodes. Also, the coupling with an insulating film was used to block the current flow and enhance the relative contribution of polarisation effects so that the frequency

dispersion of real and imaginary parts of relative dielectric permittivity can be determined accurately.

The parallel plate setup was used to derive the anisotropic dielectric properties of compacted samples in Chapter 5 of the thesis. These results were used to validate the new differential effective medium model for the anisotropic dielectric properties of shales in Chapter 6 of the thesis.

# Chapter 3 – Microstructure and Elastic Properties of Artificial Shales[1]

## INTRODUCTION

Two sets of compaction experiments were conducted on quartz-kaolinite mixtures with 100%, 75% and 60% of kaolinite by dry weight. In the first set, I used the KCl brine solution to saturate the mixtures that led to the aggregation of existing clay particles with each other and quartz silt particles. In the other set, I treated mixtures with a dispersant to separate existing clay aggregates into individual platelets. The mixtures have been further compacted in an oedometer cell at uniaxial stresses up to 30 MPa. Compressional (in vertical and horizontal directions) and shear (in vertical direction) ultrasonic wave velocities have been measured during these compaction experiments and the P-wave anisotropy has been estimated. The effect of the chemical composition of a pore fluid on shale microstructure was studied using the micro-CT and SEM image analysis. Neutron diffraction experiments were conducted to understand the orientation of clay platelets at the final stage of the compaction.

Two types of initial clay microstructures, namely aggregated (ACM[2]) and dispersed (DCM[3]), are described. Velocity and velocity anisotropy compaction trends for all the prepared samples are obtained. The influence of the microstructure on the formation of elastic properties and anisotropy of artificial shales during the mechanical compaction is investigated. The influence of silt content and type of clay microstructure on the orientation distribution functions of clay particles is also discussed.

---

[1] This chapter is an extended version of a scientific paper by BELOBORODOV, R., PERVUKHINA, M., LUZIN, V., DELLE PIANE, C., CLENNELL, M. B., ZANDI, S. & LEBEDEV, M. 2016. Compaction of quartz-kaolinite mixtures: The influence of the pore fluid composition on the development of their microstructure and elastic anisotropy. Marine and Petroleum Geology, 78, 426-438.

[2] ACM – aggregated clay microstructure

[3] DCM – dispersed clay microstructure

## RESULTS

### Compaction

The compaction experiments and measurements of the properties of artificial shales were conducted following the methodologies described in Chapter 2 of the thesis. Table 4 contains detailed information on the prepared mineral mixtures.

*Table 4. Specifications of the artificial samples.*

| Sample* | Quartz to kaolinite wt% ratio | Chemical agent | pH | Salinity, g/l | Initial clay microstructure |
|---|---|---|---|---|---|
| A0100 | 0/100 | Deionized water + KCl | 6.7 | 75 | Aggregated |
| A2575 | 25/75 | | | | |
| A4060 | 40/60 | | | | |
| D0100 | 0/100 | Deionized water + $Na_4P_2O_7$ + 100°C | 9.0 | – | Dispersed |
| D2575 | 25/75 | | | | |
| D4060 | 40/60 | | | | |

* – sample names have specific nomenclature, where the first letter stands for either aggregated (A) or dispersed (D) clay microstructure and following numbers indicate the weight percent ratio of quartz and kaolinite constituents.

The compaction curves representing porosity variations with vertical uniaxial stress are shown in Figure 30. The porosity reduction trends show significantly different behaviour for ACM and DCM samples. The effective stress required to compact the ACM samples to the same porosity is about twice higher than that for the DCM samples of the same composition. Within the groups, pure kaolinite samples are the least compressible, and the increase of the quartz fraction leads to the higher degree of the compaction at the same value of applied stress. A crossplot of wet clay porosity (i.e. porosity of the clay matrix) versus stress allows comparing the degree of compression of the clay matrix itself (Figure 30). Again, the difference in sizes of structural elements makes the clay matrices of the DCM samples the most compact. Additionally, the increase of silt fraction leads to a lower degree of clay matrix

compaction at the same stress, i.e. allows clay matrix to retain more water than in the pure kaolinite mixture at the same stress.

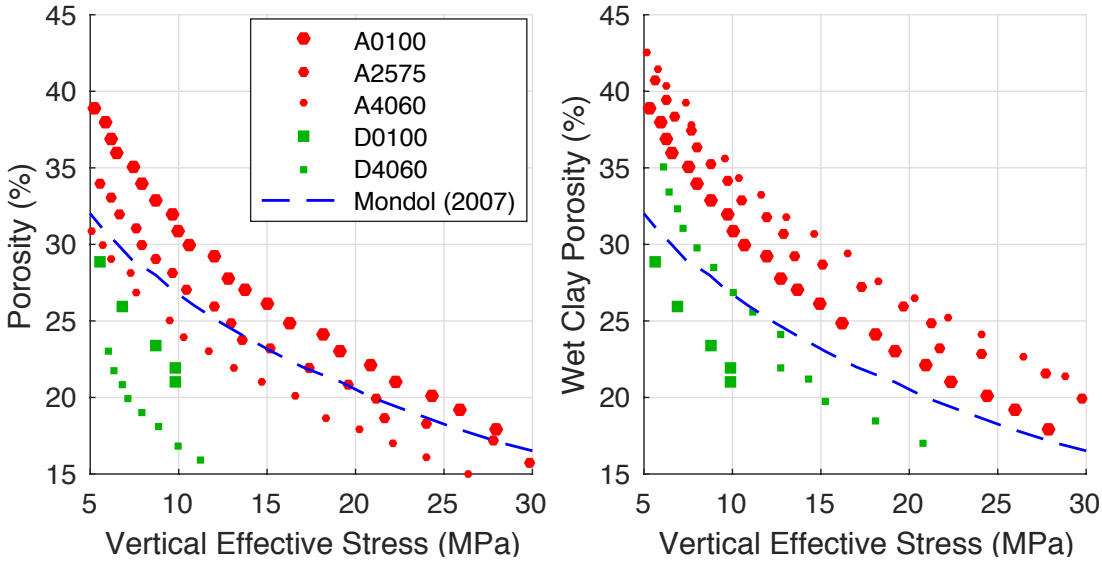


*Figure 30. Experimental mechanical compaction of quartz-kaolinite mixtures with aggregated (in red) and dispersed (in green) clay microstructure under uniaxial compression strain: (left) porosity and (right) wet clay porosity variations as a function of vertical effective stress. Experimental data of (Mondol et al., 2007) for pure kaolinite mixture is shown in blue.*

Figure 30 also shows the compaction curve for the pure kaolinite sample compacted by (Mondol et al., 2007). The porosity and wet clay porosity of their sample are bounded between the results for pure kaolinite mixtures with aggregated and dispersed microstructure. The kaolinite microstructure was not assessed by Mondol et al. (2007) but it is reasonable to assume that the trends of pure kaolinite mixtures with ACM and DCM are the upper and lower bounds for the compaction trends of kaolinite mixtures with any given mineralogy.

**Velocity versus porosity trends**

Crossplots of velocities measured for each sample versus porosity are shown in Figure 31. All the samples have equal horizontal $V_P(90)$ and vertical $V_P(0)$ compressional velocities of ~1.5 km/s at the beginning of the compaction at 70% porosity. Compaction leads to the gradual growth of the compressional velocities in both directions. Note that S-wave does not appear while the mineral mixtures remain liquid. The compressional velocities follow similar trends during compaction of all the samples: at first, they gradually increase and then, at some specific porosity, they split

so that horizontal $V_P$ becomes higher than vertical one (i.e. samples develop elastic anisotropy). The difference of 5% between $V_P$ in vertical and horizontal directions is shown with the red line on the plots. This characteristic point occurs at higher porosities in the ACM samples compared with the DCM ones having the same composition. The samples with the higher quartz content exhibit the P-wave anisotropy of 5% at lower porosities than the pure clay samples. At approximately this porosity, the S-wave starts to propagate in all the samples except the D4060, where it appears at slightly lower porosity values. This porosity, at which the samples become rigid, is hereafter referred to as critical porosity (Nur et al., 1998).

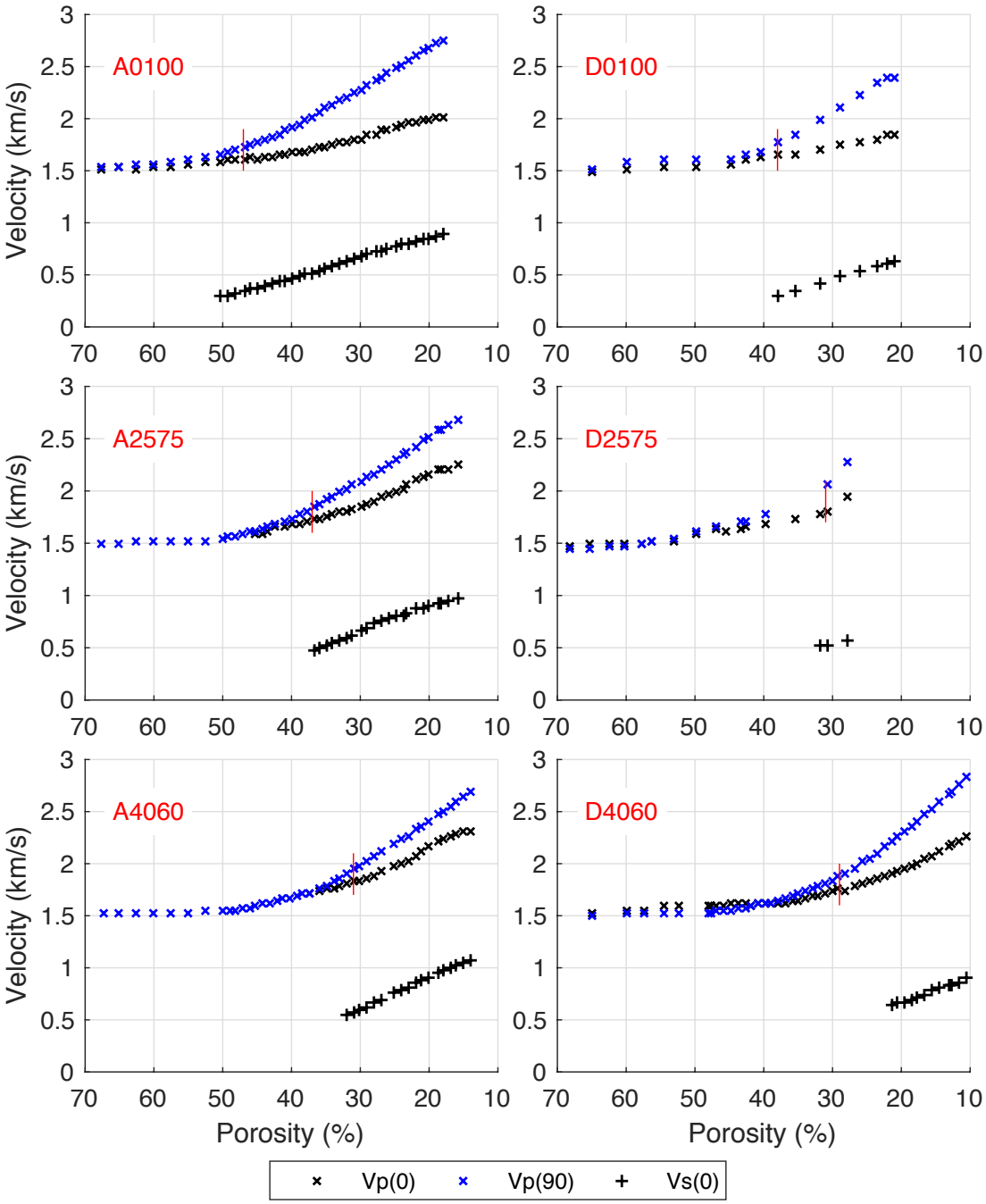


*Figure 31. Crossplots of the compressional wave velocities in vertical $V_P(0)$ and horizontal $V_P(90)$ directions and velocity of slow shear wave $V_S(0)$ versus porosity. The red line on the plots indicates the porosity value at which the difference between $V_P$ (0) and $V_P$ (90) becomes greater than 5%.*

Compaction experiments of all ACM samples A0100, A2575, A4060 and DCM sample D4060 are stopped at 18%, 16%, 14% and 10% of porosity, respectively, wherein a further increase of uniaxial pressure no longer induces any detectable deformation of the samples. Due to mechanical problems with the compaction setup,

compaction of the samples D0100 and D2575 is stopped at higher porosities of 21% and 28%.

Comparing values of compressional wave velocities at 21% porosity (Table 5), the P-wave velocities in the ACM samples are about 10% higher than in the DCM samples; S-wave velocities show even higher differences up to 20%. The drop of $V_P(90)$ from 2.65 km/s to 2.36 km/s and the slight growth of $V_P(0)$ from 2.00 km/s to 2.11 km/s is attributed to the increase of the quartz content from 0 to 40 wt% in the ACM group. DCM samples show the same behaviour where $V_P(90)$ and $V_P(0)$ change from 2.40 km/s and 1.85 km/s to 2.21 km/s and 1.90 km/s, respectively. The increase of the quartz content also diminishes the difference between the values of compressional wave velocities in vertical and horizontal directions. This difference equals 0.65 km/s and 0.55 km/s in pure kaolinite samples from ACM and DCM groups and it drops to 0.25 km/s and 0.31 km/s, respectively, in the samples with 40 wt% of quartz.

*Table 5. Comparison of the velocities of the compacted samples at 21% porosity.*

| Type of the clay microstructure | Quartz-kaolinite wt% ratio | Velocities (km/s) | | |
|---|---|---|---|---|
| | | $V_P$ vertical | $V_P$ horizontal | $V_{SV}$ |
| Aggregated | 0/100 | 2.00 | 2.65 | 0.80 |
| | 40/60 | 2.11 | 2.36 | 0.89 |
| Dispersed | 0/100 | 1.85 | 2.40 | 0.63 |
| | 40/60 | 1.90 | 2.21 | 0.66 |

At critical porosity, shear wave velocities have approximately the same values in the samples with the different type of initial clay microstructure and the same quartz fraction. However, shear wave velocities are different at critical porosity in the samples with different quartz fraction; for instance, $V_S(0)$ of the pure kaolinite samples is equal to 0.29 km/s and samples with the highest quartz content of 40 wt% have twice higher velocity of ~0.6 km/s. The growth of $V_S$ with the porosity reduction is characterized by almost linear trends with a greater slope for the samples with higher quartz content. At 21% porosity (Table 5), $V_S$ increases with the increase of quartz content from 0.80 km/s to 0.89 km/s in the ACM samples and from 0.63 km/s to 0.66 km/s in the DCM samples.

**Elastic anisotropy**

Elastic anisotropy is generally expressed in terms of Thomsen's anisotropy parameters (Thomsen, 1986).

$$\varepsilon = \frac{C_{11} - C_{33}}{2C_{33}},$$
$$\gamma = \frac{C_{66} - C_{44}}{2C_{44}}, \tag{14}$$
$$\delta = \frac{(C_{13} + C_{44})^2 - (C_{33} - C_{44})^2}{2C_{33}(C_{33} - C_{44})},$$

where the $C_{ij}$ are the corresponding elastic constants in the conventional two-indices notation. Here only the development of P-wave anisotropy $\varepsilon$ can be monitored as the velocity of S-wave is measured only in one direction and the velocity of the compressional wave propagating at 45 degrees to the bedding plane is not measured.

The evolution of Thomsen's anisotropy parameter $\varepsilon$ during the compaction is shown in Figure 32. In both ACM and DCM groups of the samples, the anisotropy constantly grows with the increase of a vertical stress. The increase of the quartz content results in a significant drop of the elastic anisotropy and this effect is stronger in the aggregated samples. The DCM sample with 40 wt% of quartz shows the anisotropy of 0.25, whereas in the ACM sample with the same quartz content, the anisotropy reaches only 0.17. It is worth noting that the rate of the change of the elastic anisotropy in the DCM samples is greater than that of the ACM samples at porosity values less than 30%.

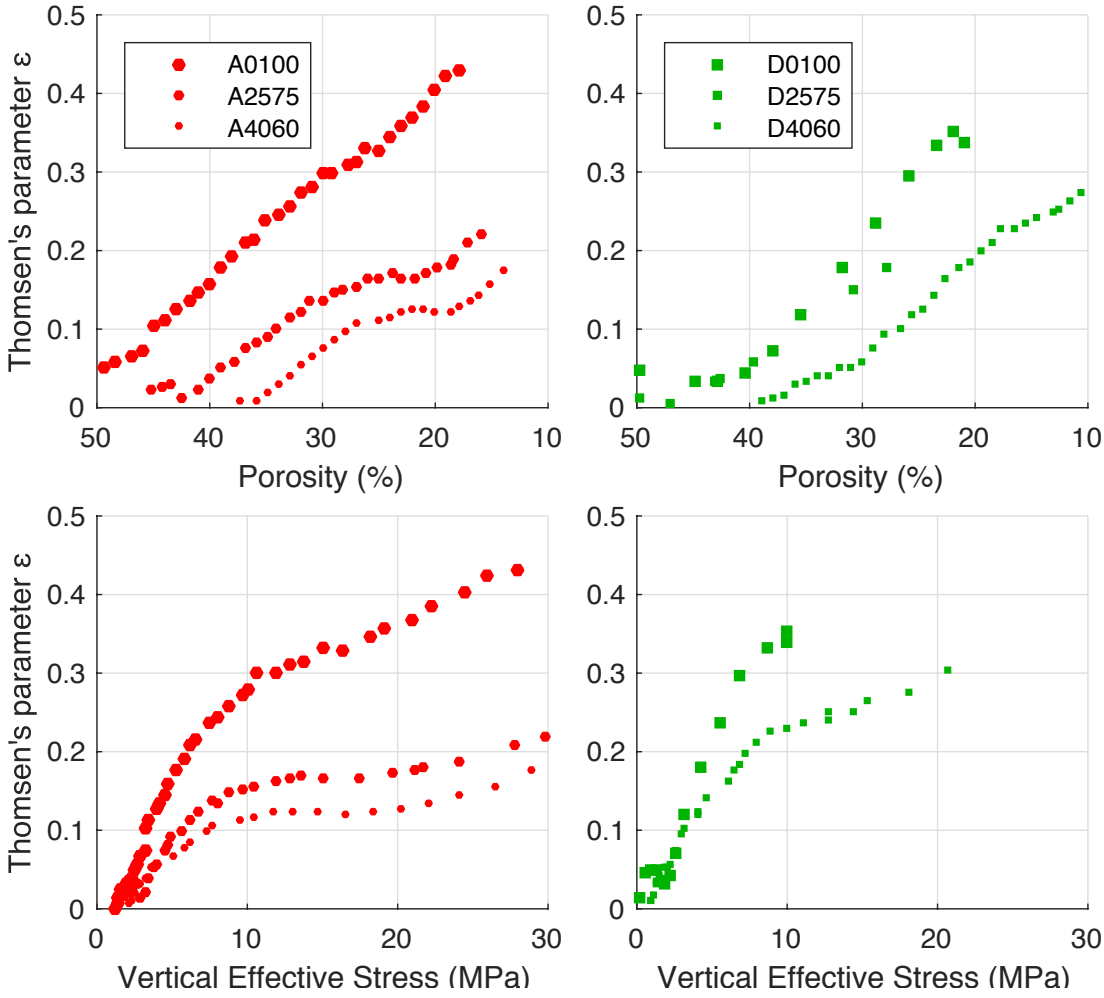


*Figure 32. (Top row) Thomsen's anisotropy parameter ε versus porosity and (bottom row) vertical effective stress given for the samples with different types of clay microstructure.*

Comparing the anisotropy vs stress trends between the two groups, one can see that 10 MPa of vertical effective stress is required to achieve the anisotropy of 0.36 and 0.27 in the DCM and ACM pure kaolinite samples, respectively. With the increase of quartz content to 40 wt%, this difference become remarkable: at 20 MPa of applied stress Thomsen's anisotropy parameter $\varepsilon$ is equal to 0.13 in the ACM sample while in the DCM sample it reaches 0.30. Vice versa compared to the DCM sample, five times higher effective stress is needed for the ACM sample to get the value of P-wave elastic anisotropy of 0.15.

**Orientation distribution of clay fraction**

Results of neutron diffraction experiments are shown in Figure 33, please refer to the Chapter 2 for details on experimental technique. The Gaussian-like shape of the distribution is similar in all samples with a single maximum at the centre of the pole

figure (i.e. normal to bedding), although the height and the width of the integrated polar angle profiles differ from sample to sample (Figure 33 bottom). Distribution density is expressed in multiples of random distribution (m.r.d). A typical accuracy for this method in application to clay is estimated as 0.1 m.r.d. The ACM samples are characterized by 6.7 m.r.d. and 5.2 m.r.d. for the pure kaolinite and quartz-kaolinite (40 wt% of quartz) samples, respectively. In the DCM group, the orientation distribution of the clay fraction follows the same trend and decreases with the increase of quartz fraction, namely, the highest distribution density of 7.4 m.r.d. is shown by the pure kaolinite sample and the sample with 40% quartz exhibits the distribution density of 4.3 m.r.d.

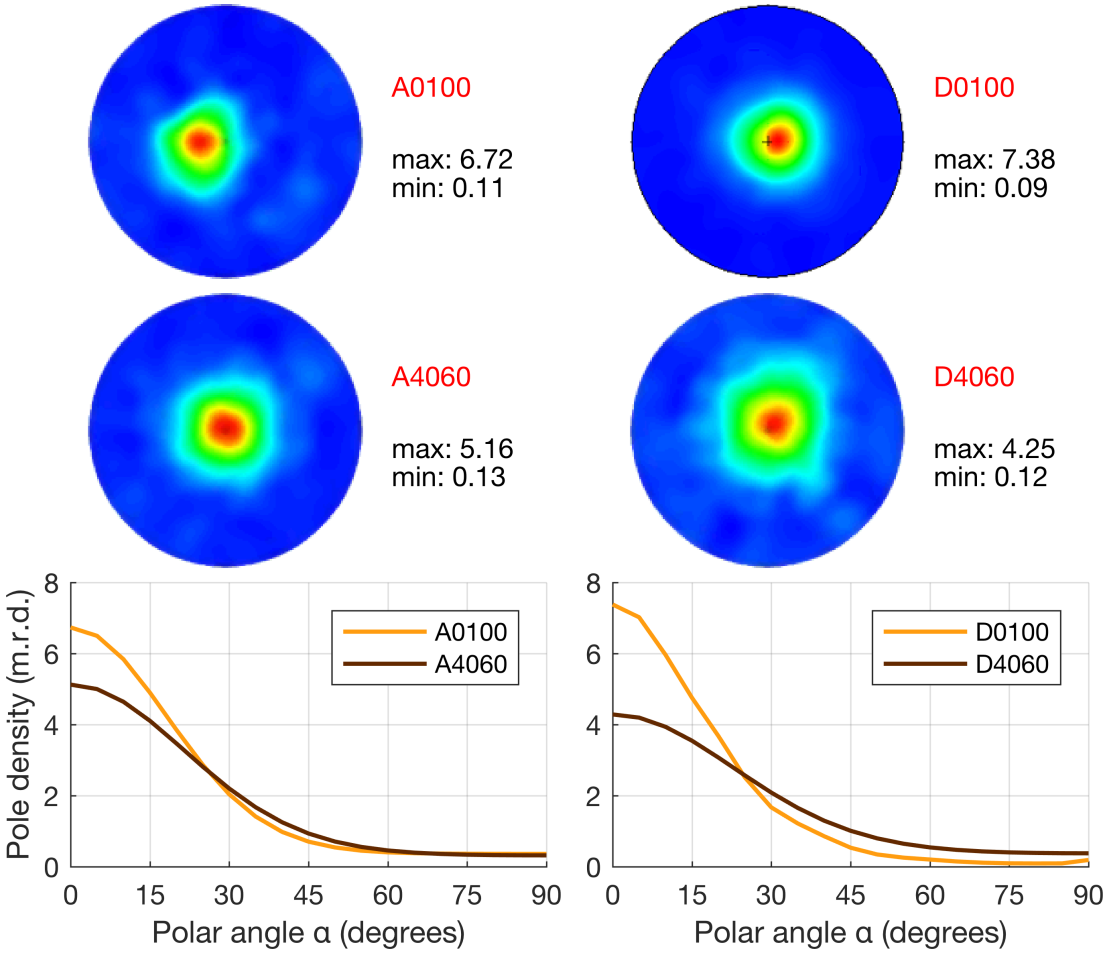


*Figure 33. Experimental c-axis pole figures of the kaolinite with corresponding integrated polar angle profiles. Distribution density is expressed in multiples of*

*random distribution (m.r.d). Maximum and minimum values of distribution density, also expressed in m.r.d., are shown on the right of the corresponding pole figures.*

**Orientation distribution of quartz inclusions**

The orientation distribution of quartz particles is estimated for all the samples containing quartz (Figure 34). The samples with 25 wt% of quartz show insignificant variations in percentage of grains oriented within the 0° to 45° range from the symmetry plane; the percentage quickly drops with the increase of the angle from 45° to 90°. About the same percentage of quartz grains, namely,24% and 29% in the samples with ACM and DCM, respectively, is oriented within 0°-15° range from the symmetry plane in the samples with the relatively low silt fraction of 25%. Hereafter, the particles oriented within 0°-15° range from the symmetry plane are referred to as oriented in a subhorizontal plane. Quartz particles in the samples with 40 wt% fraction of quartz show the much stronger orientation anisotropy as well as significant difference in fractions of the particles aligned in the subhorizontal plane in the samples with ACM and DCM, namely, 57% and 38%, respectively. Possible reasons of this difference will be discussed further in the Discussion section.

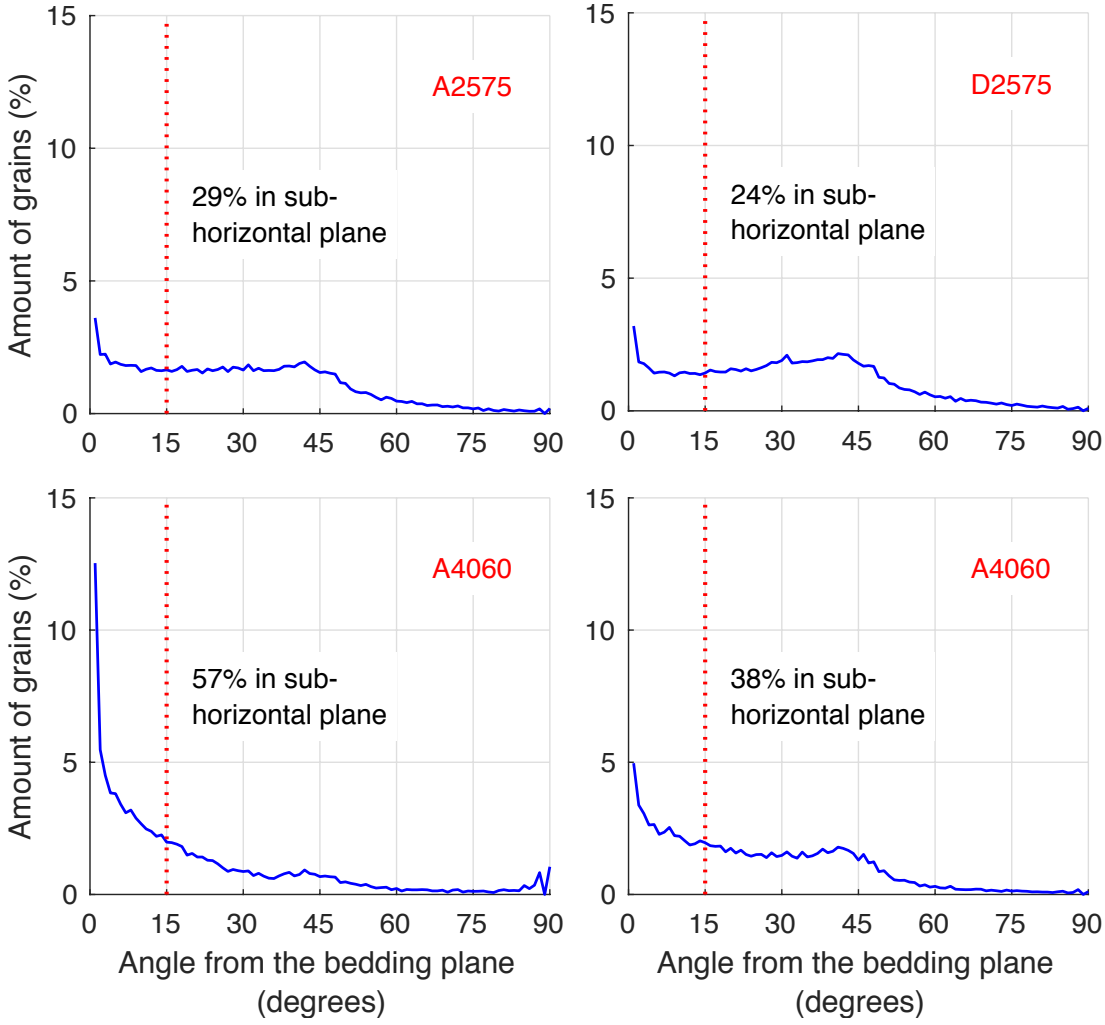


*Figure 34. The histograms of quartz grains orientation acquired from the micro-CT images of the subsamples after compaction. The dashed red line at 15 degrees denotes the limit of subhorizontal orientation of the particles.*

Despite this noticeable alignment of quartz particles, neutron diffraction measurements demonstrated an absence of CPO identified by a random (100) pole figure of quartz. In contrast to the clay particles with total correlation of CPO and SPO, the quartz grains have no such correlation. The quartz fraction should be considered as isotropic phase and quartz CPO cannot be responsible for the observed anisotropy. However, quartz SPO can cause some anisotropy through interaction with the clay phase, e.g. local realignment of clay particles around quartz grains.

**Modelling of the elastic properties**

Effective medium approaches are commonly used to model the effects of silt inclusions on elastic properties of shale (Pervukhina et al., 2015a). To do this, elastic properties of clay are assumed to be known from measurements using nanoindentation

technique (Ortega et al., 2007) or using inversion results (Bayuk et al., 2007) and to be independent of a silt fraction. Here the dependence of elastic properties of clay on porosity is investigated and the assumption that elastic properties of clay are independent of the silt fraction is verified.

To this end, the differential effective modelling approach suggested by Nishizawa (1982) is applied to simulate the elastic properties of shale as a mixture of clay matrix with quartz inclusions. It was assumed that all the samples become transversely isotropic during the compaction, the degree of the compaction is uniform in all parts of the sample at each porosity level, and quartz grains may be approximated with oblate spheroids with a mean aspect ratio of 0.5. As the measurements of quasi-longitudinal velocity at 45° to the symmetry axis were not done during compaction, it was assumed that the anisotropy in the samples is elliptical. Using this assumption the $V_P(45^\circ)$ was calculated at each step of the compaction to get all five elastic constants characterizing the VTI medium of clay matrix. The elastic properties of clay matrix calculated from velocities and density measured at each compaction step of the experiment for the sample A0100 were used as the elastic moduli of clay. Bulk and shear moduli of quartz were chosen as 37 GPa and 44 GPa, respectively. The volumetric content of quartz in the samples A2575 and A4060 was calculated at each step of compaction. The mean aspect ratio of grains in the used quartz powder was derived from the analysis of 3D micro-CT images.

The modelling results are shown in Figure 2 in comparison with experimental data. In the case of sample A2575, the modelled elastic moduli are in good agreement with the measured one (Figure 35a). Perturbation of the aspect ratio of inclusions from 0.3 to 1 results in only small fluctuations around the experimental data. Thus, in the case of relatively small concentration of quartz inclusions, elastic properties of clay and silt mixture at all compaction steps can be modelled using DEM approach and clay moduli may be assumed to be independent of the silt fraction. Moreover, the anisotropy of the shale rock with low quartz content is mainly controlled by the anisotropy of clay matrix, whereas the presence of anisometric inclusions has a minor effect on the elastic anisotropy.

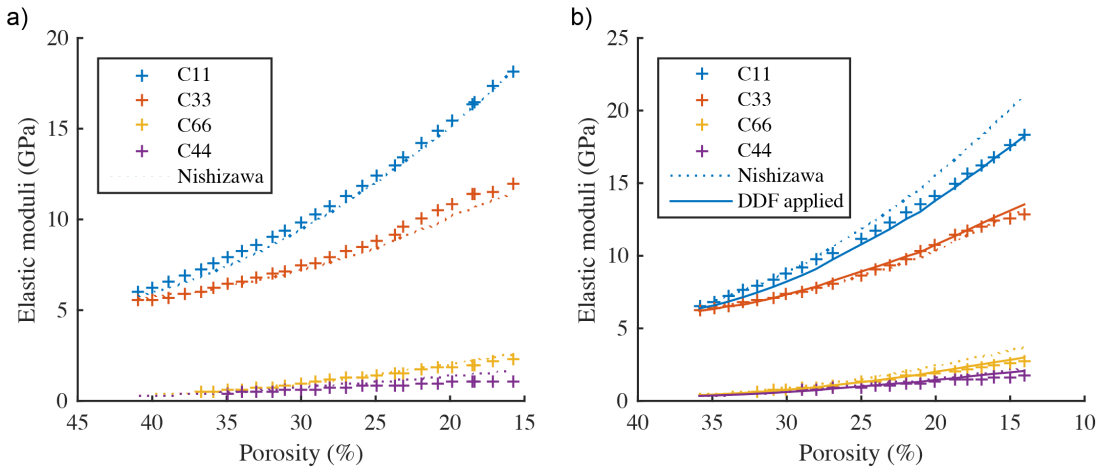


*Figure 35. Elastic constants for the samples a) A2575 and b) A4060 obtained from experiment, modelling using Nishizawa's differential effective medium (DEM) approach and applying directional distribution function (DDF) for compaction.*

In the case of sample A4060 with high quartz content, the modelled $C_{11}$ and $C_{66}$ moduli significantly overestimate the experimental ones at porosities below 25% (Figure 35b). One possible explanation is that when the concentration of quartz inclusions is high, elastic moduli of clay are not constant anymore, and elastic moduli of pure clay sample A0100 cannot be used for the prediction of elastic properties of shale. This can be explained by the fact that in the shale with aggregated clay microstructure, clay platelets tend to cake silt inclusions (Figure 36). If the concentration of such silt inclusions is high, the orientation distribution function (ODF) of clay platelets will significantly deviate from the ODF in the case of pure clay sample A0100 and the elastic moduli of the clay in the A4060 sample will also be different.

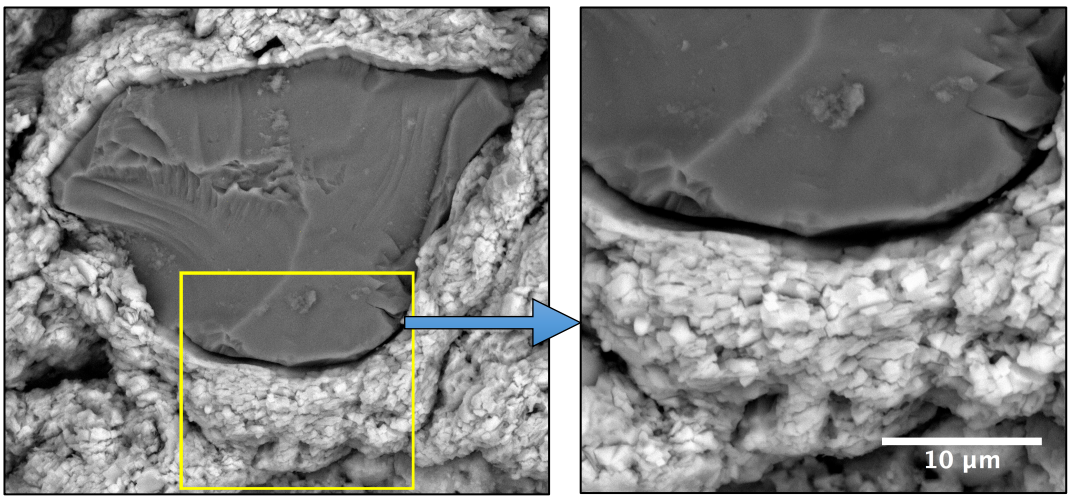


*Figure 36. SEM image of quartz grain covered with kaolinite coats.*

The directional distribution function (DDF) proposed especially for mechanical compaction (Owens, 1973, Baker et al., 1993) is used to model the elastic moduli of clay in sample A4060 with a high concentration of clay inclusions:

$$f(\theta) = \frac{1}{4\pi} \frac{a^2}{(\cos^2\theta + a^2 \sin^2\theta)^{3/2}} \tag{15}$$

where $\theta$ is the angle between the VTI symmetry axis and the normal of the clay platelet and $a > 1$ is the aspect ratio of the strain ellipse, i.e. the ratio of the initial to the final height of the sample. When elastic properties of clay modelled taking into account Equation 15, DEM modelling results are in good agreement with the experimental data (Figure 35b).

# DISCUSSION

## Applications in hydrocarbon exploration

Shales are notorious for their strong polar anisotropy, the elastic anisotropy with the vertical axis of symmetry (e.g. Thomsen, 1986, Sayers, 2005). As shales typically serve as natural seals of conventional oil and gas reservoirs, knowledge of this polar anisotropy is of practical importance for improved reservoir characterization, namely, accurate seismic to well tie, reliable surface seismic data interpretation and enhanced amplitude versus offset analysis. Knowledge of shale anisotropy is equally important for oil and gas shales, the quickly growing realm of unconventional reservoirs, due to extremely high values of observed Thomsen's anisotropy parameters (e.g. Pervukhina et al., 2015b, Vernik and Nur, 1992). While the elastic anisotropy of layered media, typical for sedimentary basins, can be estimated using Backus averaging (Backus, 1962), the shale polar anisotropy is rather unpredictable. It shows no correlation with seismic velocities and exhibits a significant scatter for the shale samples extracted from the same depth (e.g. Pervukhina and Rasolofosaon, 2015). All the attempts to model elastic anisotropy results in descriptive models with a large number of adjustable parameters that only work for locations that they were built for. Powerful predictive anisotropy models for shales can only be built if the key processes that are responsible for the development of anisotropic properties of shale are understood.

## Factors influencing pore fluid and mechanical compaction in newly deposited sediments

The processes of the development of microstructural anisotropy in clay sediments are complex and take place during all stages of sedimentation and diagenesis (e.g. Osipov et al., 2004, Strakhov, 1967). The formation of microstructure begins in natural colloidal water solutions during the initial deposition of clay particles, continues with their partial alignment caused by burial stress and resumes with the further temperature and pressure increase in the form of either smectite-to-illite transformation or cementation (e.g. Thyberg et al., 2009, Freed and Peacor, 1989, Pollastro, 1993, Peltonen et al., 2009, Delle Piane et al., 2015, Day-Stirrat et al., 2008).

Freshly deposited clay particles exist in either dispersed or aggregated state depending on the chemical composition of the saturating water (e.g. Osipov et al.,

1989, Chuhrov, 1955, Efremov, 1971, Dong and Wang, 2008). For instance, the aggregation of individual clay particles occurs due to the lack of stability in the colloidal system in the presence of an electrolyte such as sea water. If the system is heterogeneous in terms of particle sizes (i.e., in typical shale, silt size ranges from 2 to 75 μm and clay particle sizes do not exceed 2 μm (ASTM, 2007), the aggregation also leads to the formation of clay coats on the surfaces of coarse mineral grains due to the 400-500 times faster adhesion of small clay particles to bigger silt grains (Efremov, 1971). Thus, the deposition of shales with ACM can be expected in a marine environment. The dispersed state of the colloidal system can be stabilised by the presence of organic matter which leads to high pH above 6 and neutralizes the surface potential of the clay particles (Osipov et al., 1989). The clay particles, separated from each other in such stable colloidal systems, are deposited individually and independently from the silt particles. Such shales with DCM are anticipated in lacustrine ecosystems with low sedimentation rates and in the presence of high-molecular compounds of humic acids.

In this experimental study, the processes of mechanical compaction are simulated on clay mixtures with initially aggregated or dispersed states of clay microstructures. As the clay powder that is used in the experiment consists of aggregated particles, the clay with DCM is prepared by boiling clay mixtures with sodium pyrophosphate tetrabasic. This chemical treatment of kaolinite mixtures and accurate control of the concentration and cation composition of water solutions along with their pH scales allowed producing two sets of artificial samples with the aggregated and dispersed clay microstructure. Each set contains a pure kaolinite sample to monitor the compaction behaviour of a clay fraction alone and two samples with 25 wt% and 40 wt% of quartz silt. The pure kaolinite shale does not exist in natural sediments and is compacted for modelling needs, but the silt fractions in other two samples are within the ranges described in the literature for natural marine sediments (e.g. Hamilton, 1979, Hamilton, 1980).

The silt sized grains of used crushed quartz powder are characterized by the mean aspect ratio of 0.5 and have an oblate spheroidal shape, as the low-aspect ratio silt inclusions seems to be typical for natural shales. The micro-CT images of the three natural shales from Mancos, Kimmeridge and Pierre formations are shown in Figure 37. They all have the anisometric inclusions with aspect ratios below unity. Quartz grains tend to orient normal to the stress within the clay matrix even at low silt

concentrations (Figure 34, top row). The increase of the quartz content in both groups of mixtures is accompanied by the better alignment of quartz grains in the bedding plane of the samples (Figure 34, bottom row). This effect is more obvious for the aggregated samples (Figure 34, bottom left) as in this case the size of the quartz grains is increased by the coats formed by kaolinite platelets on their surfaces (see, Figure 36).

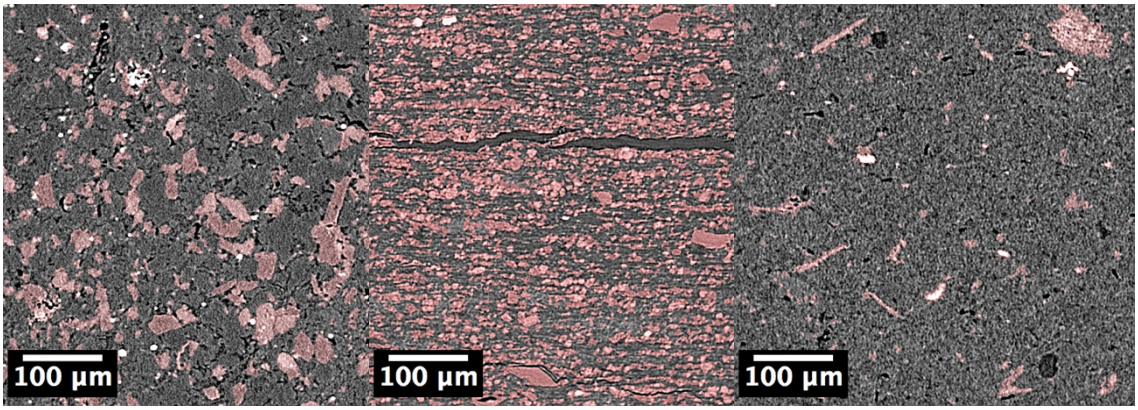


Mancos shale Kimmeridge shale Pierre shale

*Figure 37. Micro-CT images of natural shales with the bedding plane in horizontal direction. Dense, elongated inclusions of non-clay minerals are highlighted in red.*

**Formation of microstructure**

SEM images of the samples with ACM show that they consist of silt quartz grains covered with thick conforming kaolinite coats (Figure 36), and axial clay aggregates (Figure 38, Figure 39, left). On the contrary, the samples with DCM exhibit individual clay platelets and ultramicroaggregates forming continuous turbulent microstructure with the bare quartz grains embedded in it (Figure 39, right). In samples with ACM, clay coats cover the quartz grains and increase the dimensions of an average silt grain by ~40% (Figure 36). Thus, the quartz grains interact only through the surrounding clay coats during the compaction and, as a result, they are well separated from each other on the SEM images. The individual clay aggregates have a shape of oblate spheroids with the symmetry axes normal to the bedding. (Figure 38). The internal structure of these aligned particles seems to be preserved during compaction as the textured blocks with the same alignment of clay particles are clearly observed in Figure 40.

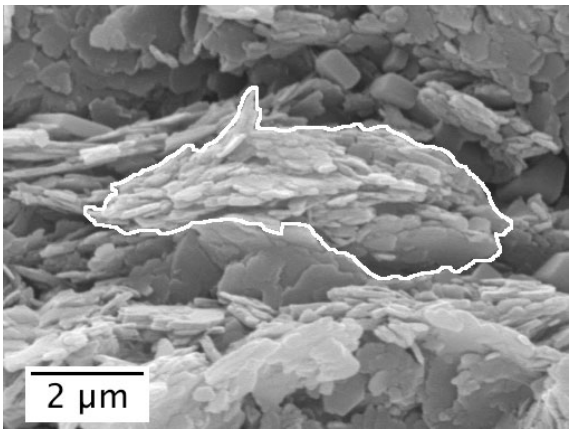


*Figure 38. SEM image of the clay aggregate consisting of aligned individual clay platelets (Sample A2575).*

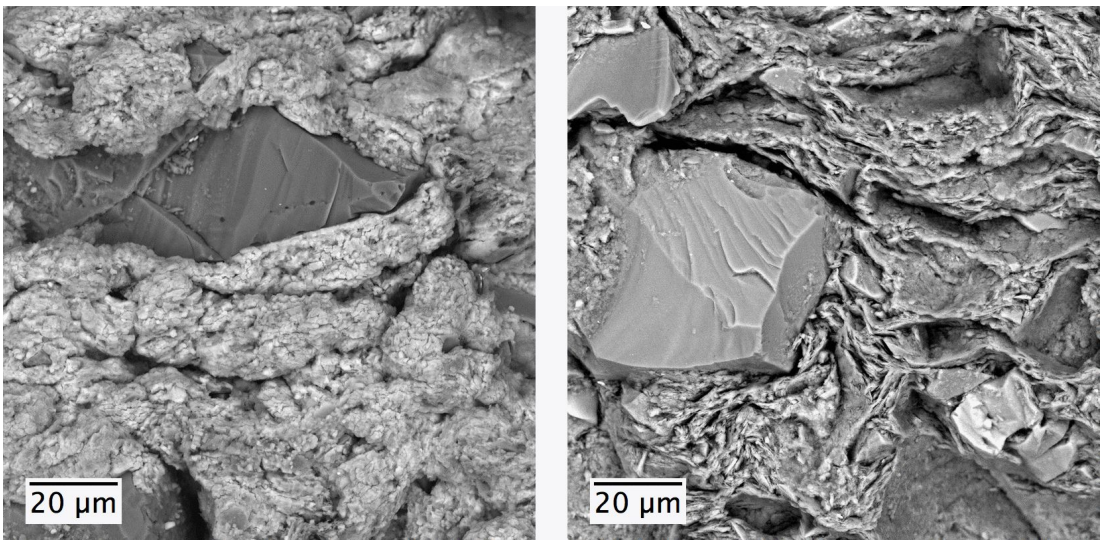


*Figure 39. SEM images of the compacted samples prepared with a) aggregated and b) dispersed clay microstructure.*

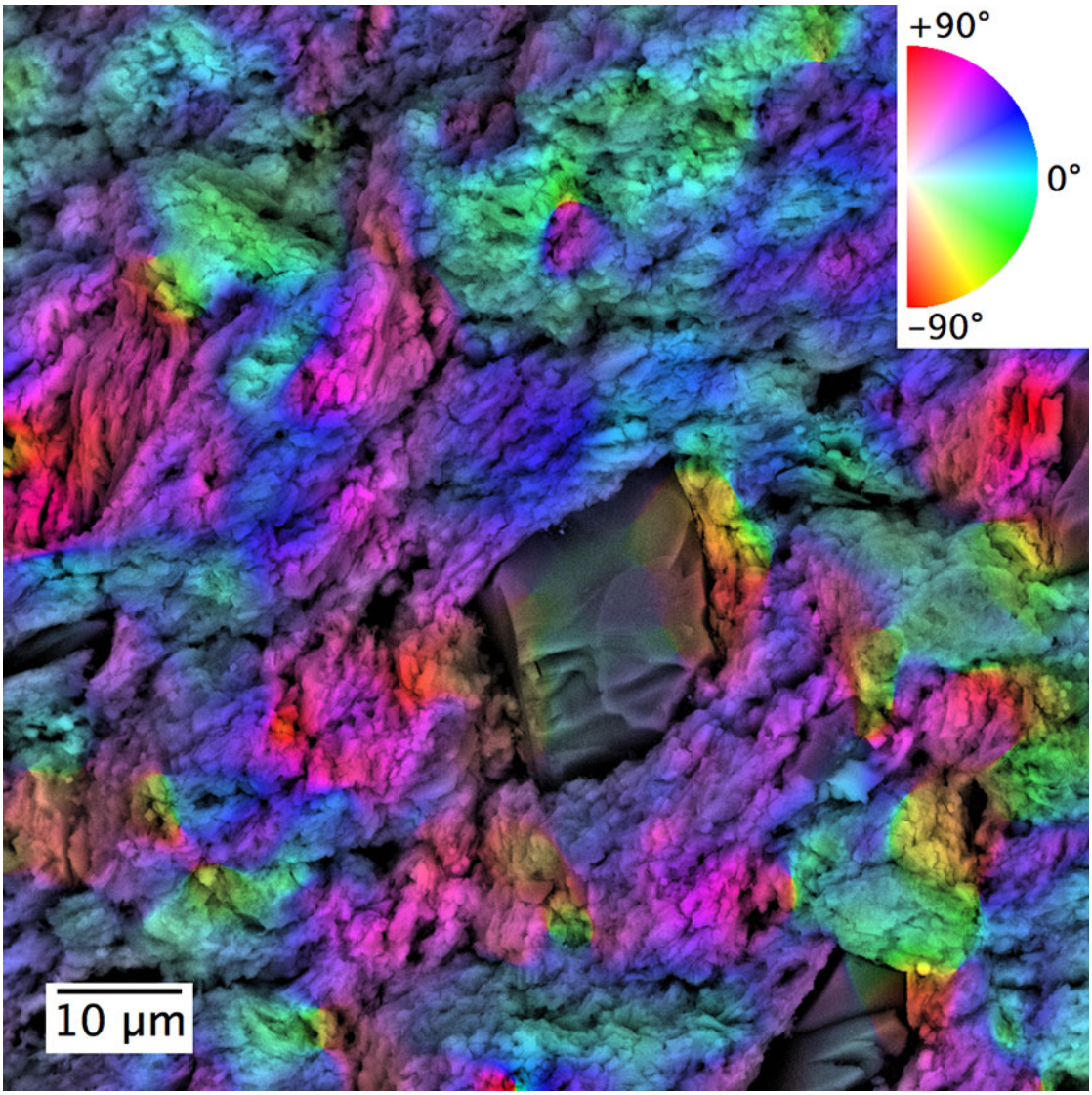


*Figure 40. Distribution map of clay preferred orientations in the sample A2575 with the corresponding colour wheel showing angles relative to the bedding plane.*

Analysis of neutron diffraction data confirms the strong alignment of clay particles in the plane normal to the compaction stress in both pure kaolinite samples. However, the pure kaolinite sample with DCM shows the much better alignment of clay particles compared to the pure kaolinite sample with ACM. This might be explained by the higher rotational mobility of individual clay platelets, compared to that of clay associations in the aggregated sample.

The presence of 40wt% quartz decreases the degree of clay alignment, however this effect is different in the samples of both groups. The silt leads to the significant drop in clay platelet alignment in the dispersed sample explained with the high rotational mobility of the dispersed clay platelets, which pivot around the quartz grains Figure 41. At the same time clay particles in the aggregated sample with the same

quartz fraction do not lose their alignment to that extent (5.2 m.r.d. vs. 4.3 m.r.d. in the dispersed sample, see Figure 33 for more details). Further investigation of shale samples with DCM and ACM with different silt fractions is necessary to understand the critical quartz particle fraction at which a load bearing quartz skeleton is formed and its effect on the clay particle orientation.

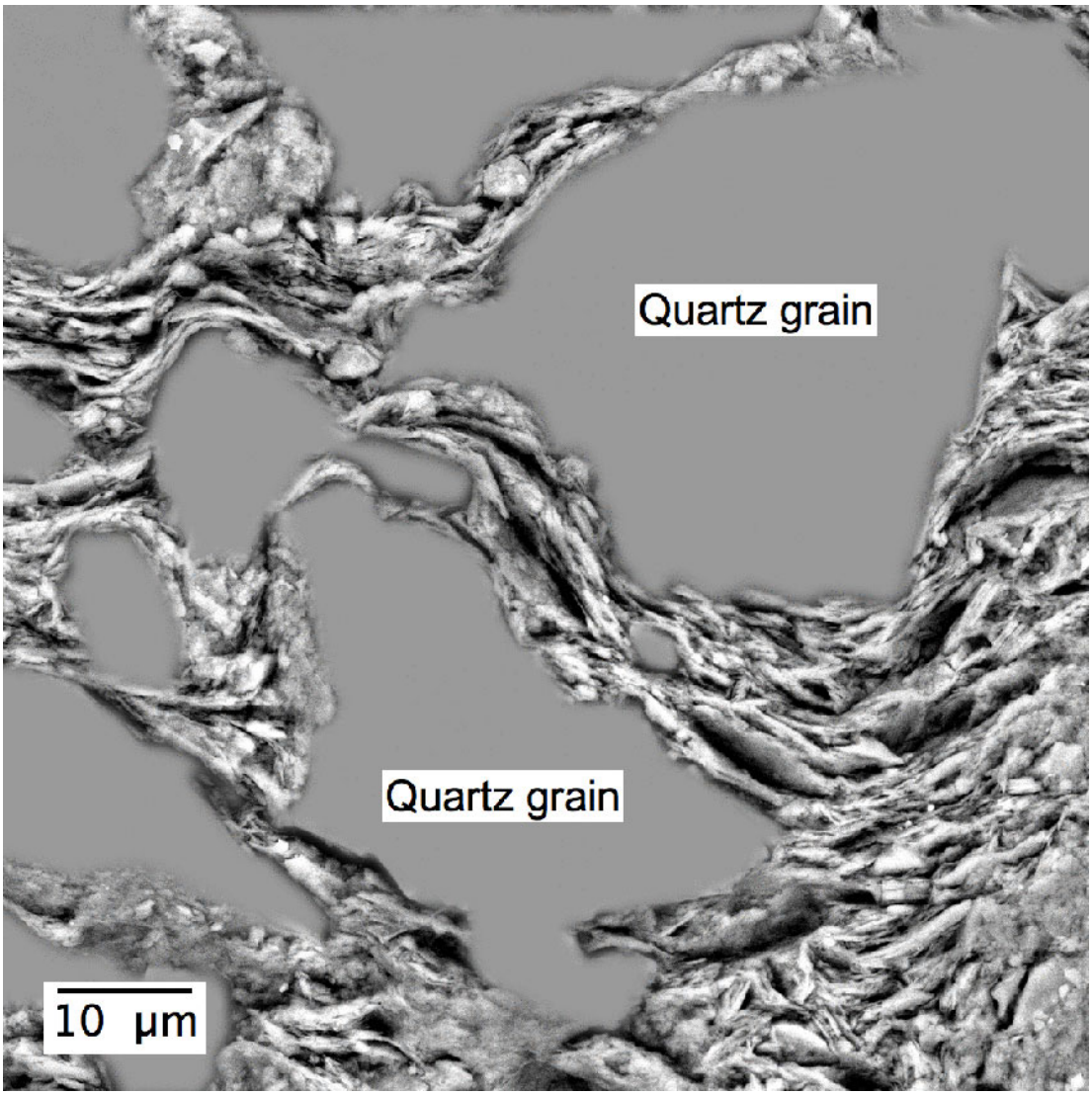


*Figure 41. SEM image of the clay platelets squeezed among the silt-sized quartz grains shaded in grey (sample D4060).*

**Elastic anisotropy and compaction trends**

The critical porosity, at which the artificial shale samples become rigid and elastic anisotropy starts developing, depends on clay fraction and microstructure. An increase of quartz-kaolinite ratio shifts critical porosity towards lower values. This effect is stronger in ACM samples where clay particles merge to create bigger structures and these structures become load-bearing at higher porosities. Therefore,

the elastic anisotropy develops at higher porosity values in the ACM samples compared to the DCM ones. The further porosity reduction results in a faster growth of anisotropy in DCM compared to ACM samples; thus, it reaches higher values at low porosities.

All the comparisons in Results section are given for the same porosity values for the samples from both groups. The difference in elastic properties becomes even more significant if compared at the same effective stress values. To achieve the same porosity and anisotropy values in samples with ACM they must be subjected to 2 – 5 times higher stress compared to DCM samples. Therefore, natural shales deposited in marine and lacustrine environments will have different compressibility and, consequently, compaction trends even if their mineralogy is the same.

The experimentally observed development of elastic anisotropy can be explained through interaction of several microstructural features in the samples. For the pure clay samples, the whole anisotropy is rooted into CPO of the clay particles and the micro-mechanical interaction between clay particles. The P-wave anisotropy $\varepsilon$ in Figure 32 (that also can be seen as a split between $V_P(90)$ and $V_P(0)$ in Figure 31) is controlled by a balance between these two mechanisms. Although, CPO is stronger for DCM than for ACM (7.4 m.r.d. vs 6.7 m.r.d.), the overall effect of anisotropy in the compacted samples is dominated more significantly by the micro-mechanical interaction. Within each group of samples, ACM and DCM, with essentially the same particle interaction mechanism, the anisotropy development as function of degree of compaction is apparently due to development of CPO. Since c-axis of clay particles are preferably aligned vertically, while c-axis slowest velocity direction in the single crystal, the vertical direction also shows slower wave velocity in the compacted samples. In the same way of consideration, within each group, ACM and DCM, the effect of anisotropy is partially weakened by introducing essentially isotropic quartz grains and therefore the anisotropy is decreased with the higher quartz content.

## SUMMARY OF CHAPTER 3

The chemical interaction between clay and saturating fluid is an important part of mechanical compaction and the chemical composition of saturating fluid affects the properties of compacted sediment along the traditionally considered factors such as clay mineralogy and silt fraction. A unique set of compacted artificial shales with the same clay mineralogy though with different clay microstructure has been prepared and investigated in this study. The microstructural differences in these samples, analysed using SEM, micro-CT and neutron diffraction methods, have helped to explain different trends of the elastic anisotropy development during compaction. The main findings can be summarised as follows:

- The analysis of the SEM images indicates various structural elements in the two studied groups of the samples. The mixtures prepared with the KCl brine (i.e. ACM samples) comprise oblate aggregates of clay particles and quartz grains covered with conforming clay coats. The mixtures prepared with dispersant (i.e. DCM samples) consist only of individual clay platelets, their small associations (ultramicroaggregates) and quartz grains.
- The data obtained with micro-CT scanner show that quartz particles exhibit better alignment in mixtures with aggregated clay microstructure as quartz grains are covered with thick layer of clay extending their dimensions. Moreover, the higher the quartz content the better quartz grains are aligned in subhorizontal plane.
- The neutron diffraction experiment confirms that the development of elastic anisotropy is mainly controlled by the two major effects: the CPO of clay fraction and micro-mechanical interactions of the clay particles, and both are affected by the chemical composition of the pore fluid. The silt fraction diminishes the total elastic anisotropy due to the random CPO of quartz particles. However, in ACM samples, the negative influence of silt fraction on their elastic anisotropy is partially reduced by the mutual effect of stronger SPO of quartz grains normal to the compaction strain and better alignment of surrounding clay platelets.
- The velocities in both directions increase with compaction; the elastic anisotropy starts to develop as the critical porosity is reached. The increase of the quartz content decreases the critical porosity; it also leads to the higher values of P-wave velocity in the vertical direction retaining the same values of horizontal one at the same porosities that consequently results in the weaker anisotropy of the sample.

- Although at the beginning of the compaction, the elastic anisotropy is observed at higher porosity values in the samples with ACM, the samples with DCM have exhibited higher elastic anisotropy at low porosities (<25 %).
- The samples with the aggregated and dispersed clay microstructure are characterized by different compressibility behaviour. The ACM samples require 2–5 times higher stress to achieve the same porosity (and anisotropy) than the DCM samples.
- Compaction experiments on kaolinite-quartz mixtures with aggregated clay microstructure have been successfully modelled using differential effective medium approach. Modelling results show that the elastic properties of clay can be considered independent of the concentration of quartz inclusions when the latter is low. Clay properties depend on the silt fraction when the concentration of quartz inclusions is relatively high (40% by dry weight in this case). Clay platelets cake the silt particles at any silt concentration, however, at the high concentration of inclusions this process results in different ODF of clay platelets and different elastic properties of clay, which have been successfully modelled with directional distribution function proposed for mechanical compaction.
- Further studies of artificial samples with clay mineralogy different from kaolinite are necessary to understand whether chemical interaction of saturating fluid and clay is ubiquitous in the process of shale compaction.

# Chapter 4 – Compaction Trends of Full Stiffness Tensor and Fluid Permeability in Artificial Shales[4]

## INTRODUCTION

This chapter is dedicated to the investigation and correlation of all five elastic coefficients of a transversely isotropic (TI) medium and its permeability in the direction parallel to the symmetry axis during mechanical compaction experiments. The approach is applied to synthetic shale samples to investigate the effect of composition and applied stress on their elastic and transport properties. Compaction trends for the five elastic coefficients that fully characterize TI anisotropy of artificial shales are obtained on a porosity range from 40 % to 15 %. A linear increase of elastic coefficients with decreasing porosity is observed. The permeability acquired with the pressure-oscillation technique exhibits an exponential decrease with decreasing porosity. Strong correlations are observed between an axial fluid permeability and seismic attributes, namely, the $V_P/V_S$ ratio and acoustic impedance, measured in the same direction. These correlations might be used to derive permeability of shales from seismic data given that their mineralogical composition is known.

[4] This chapter is an extended version of a scientific paper by BELOBORODOV, R., PERVUKHINA, M. & LEBEDEV, M. 2018. Compaction trends of full stiffness tensor and fluid permeability in artificial shales. Geophysical Journal International, 212, 1687-1693.

## RESULTS

The sample preparation technique, methods for measuring the hydraulic and anisotropic elastic properties of shale samples during the mechanical compaction, as well as the signal processing techniques used to derive the elastic properties of the samples are summarized in Chapter 2 of the thesis. Five artificial shale samples were investigated in this work. Three samples are kaolinite-based mixtures with 0, 20, and 40 weight percent of quartz. Two mixed-clay samples (1:9 smectite-kaolinite weight ratio) are made with 0 and 20 percent of quartz.

### Elastic properties

The five independent elastic constants and Thomsen's anisotropy parameters $\varepsilon, \gamma$, and $\delta$ (Thomsen, 1986) are calculated from the measured velocities and densities for the five artificial shale samples (Figure 42). All the elastic constants exhibit almost a linear increase with the porosity reduction from 0.40 to 0.15. The moduli $C_{11}$, $C_{66}$ that correspond to P- and horizontally polarised S-wave velocities measured in the horizontal direction noticeably exceed the moduli $C_{33}, C_{44}$ calculated from the velocities measured in the vertical direction. The P-wave anisotropy parameter $\varepsilon$ increases almost linearly with the porosity reduction. In contrast, the S-wave anisotropy parameter $\gamma$ initially characterized by significant values of 0.5-0.7 decreases with the compaction. The anisotropy parameter $\delta$ fluctuates around some constant value so that $\delta < |0.2|$. The increase of quartz content leads to a substantial decrease in the absolute values of the anisotropy parameters via the stiffening of the clay matrix in the direction normal to the bedding and weakening of the clay particle orientation. This effect may be observed in both kaolinite-based (Figure 42a, b, c) and mixed-clay-based samples (Figure 42d, e).

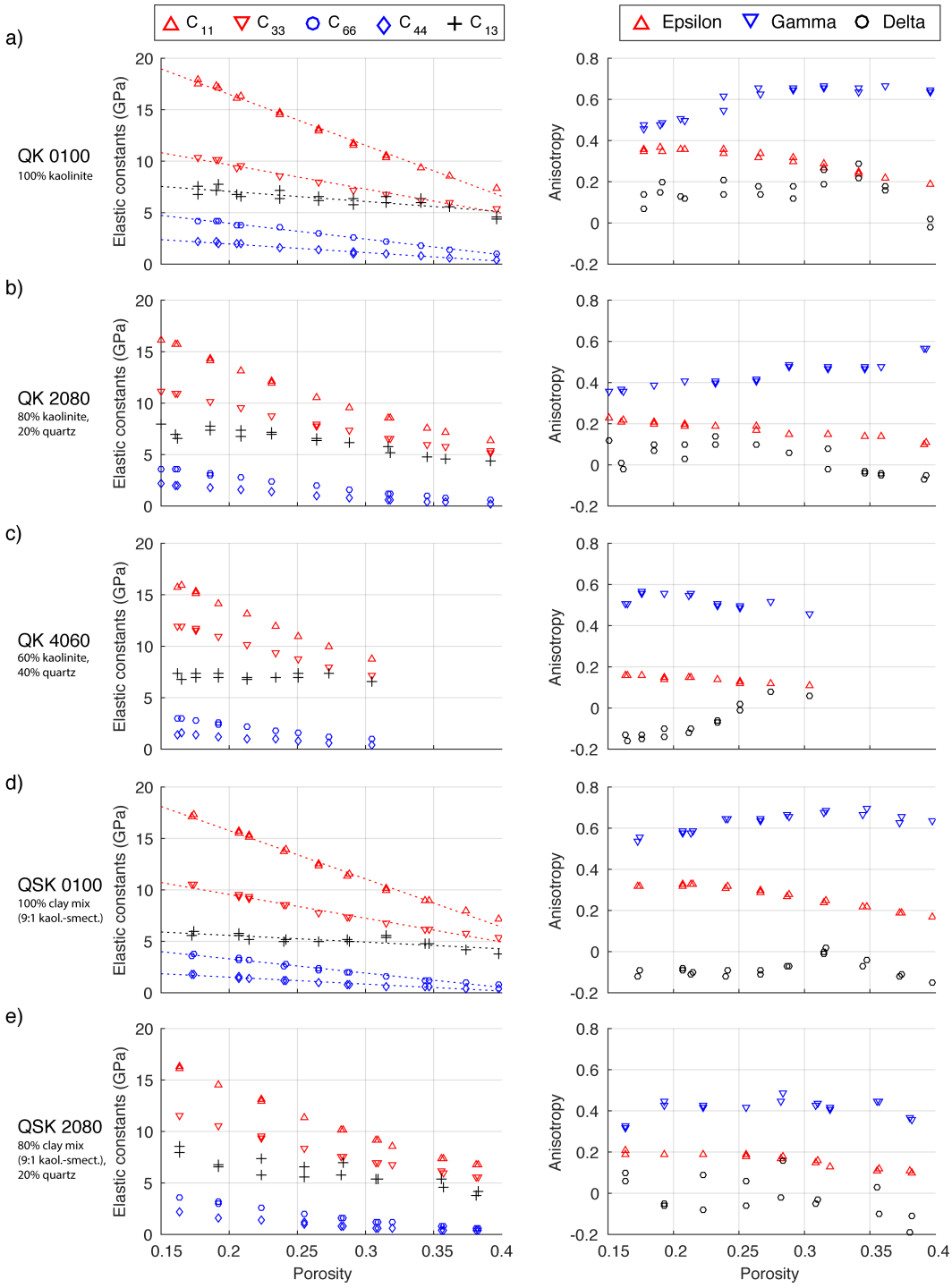


*Figure 42. Elastic constants (left hand side) and Thomsen's anisotropy parameters $\varepsilon, \gamma, \delta$ (right hand side) versus porosity for five artificial shale samples. Dashed lines show the best linear fit for the elastic constants of the pure clay samples.*

## Permeability

The variations of permeability with porosity in the direction perpendicular to the bedding plane obtained for the five samples are shown in Figure 43 in semi-

logarithmic scale. Permeability decays exponentially by an order of magnitude in all the samples during the compaction. In the pure kaolinite sample, permeability drops from $10^{-19}$ to $2 \cdot 10^{-20}$ m$^2$ while porosity decreases from 0.40 to 0.18. The pure clay kaolinite-smectite sample shows lower permeability values that decrease from $4 \cdot 10^{-20}$ to $9 \cdot 10^{-21}$ m$^2$ over the porosity range of 0.35–0.17. The increase of quartz content by 20 wt% results in an increase of the permeability by approximately half an order of magnitude in both the kaolinite and mixed-clay based samples.

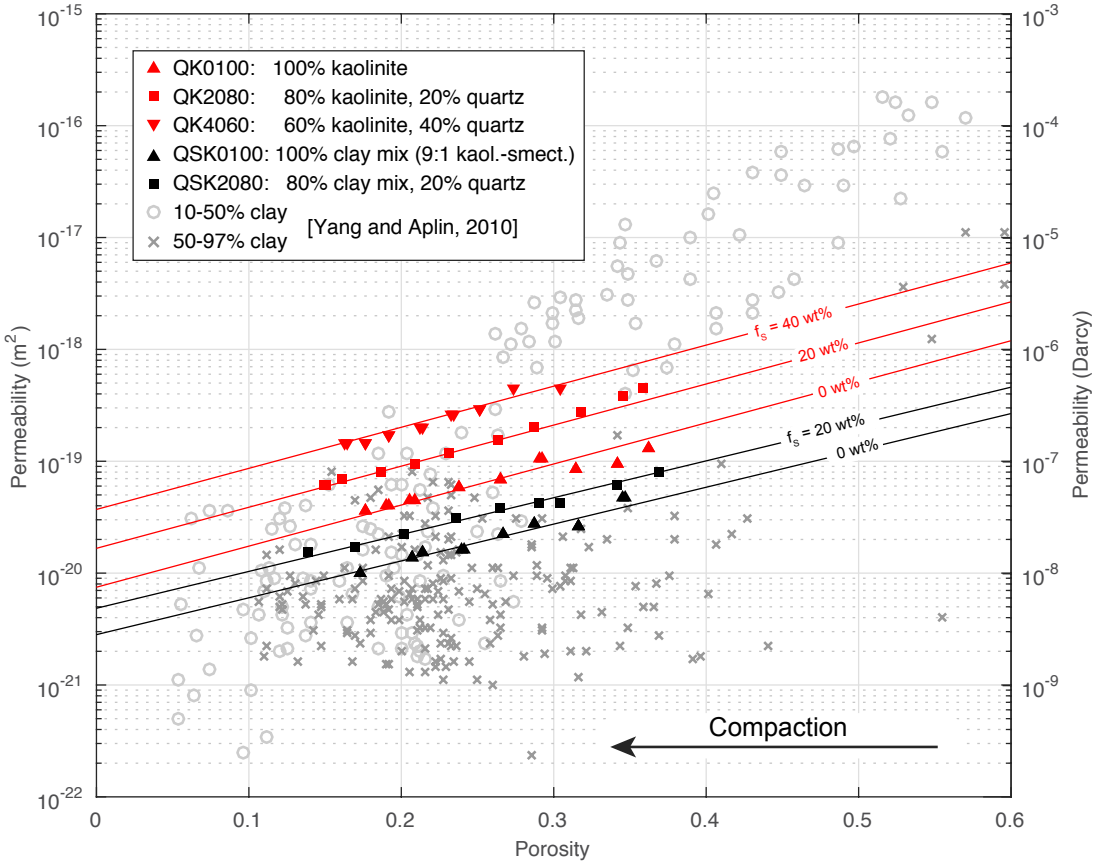


*Figure 43. Hydraulic permeability compaction trends in the artificial shale samples in comparison with Yang and Aplin (2010) data on permeability-porosity relationships in natural mudstones and shales. Solid lines, red for kaolinite-based samples and black for the clay mix based samples, show multiple linear regression fit calculated for given values of quartz content ($f_s$) and porosity values.*

The higher permeability of the quartz-bearing samples might result from the additional porosity formed on quartz-kaolinite interfaces (Keller et al., 2011) and this porosity may have a dominating effect on their bulk permeability. At the same porosity level, the alignment of clay aggregates is weaker in the samples containing quartz (Beloborodov et al., 2016b) that assures the lower tortuosity of their pore network in

the direction normal to the bedding. Similarly, the wet clay porosity (i.e. porosity of the clay matrix) is also higher that implies larger pore throats within the pore network.

Previously measured and modelled porosity-permeability relations for natural argillaceous rocks and shallow marine sediments (Yang and Aplin, 2010) are also shown in Figure 43 also illustrates experimentally obtained and modelled porosity-permeability relations for natural argillaceous rocks and shallow marine sediments (Yang and Aplin, 2010). Although the permeabilities measured on the quartz-kaolinite artificial shales lay within the permeability-porosity range of natural rocks, they overestimate the permeability of the natural mudstones with high clay content (50–97 %). This fact can be explained by the difference in mineralogical composition between the kaolinite based artificial shales and natural shales as the latter almost always contain some amount of smectite clay minerals that strongly reduce the permeability due to their swelling nature and vast specific surface area of ~800 $m^2/g$ compared to ~40 $m^2/g$ of kaolinite. As implied by the Kozeny-Carman equation, permeability is inversely proportional to the square of the specific surface area. Here I show that additional 10 % of smectite in pure clay sample reduces the permeability by half an order of magnitude compared to pure kaolinite sample at the same porosity. Moreover, some deeply buried natural shales could have undergone a high-temperature chemical compaction that initiates the formation of autogenic minerals into a pore space, the process that further reduces their permeability.

**Correlations of elastic properties and permeability**

The hydraulic and elastic properties of the artificial shales, for the first time acquired simultaneously during the laboratory mechanical compaction, allow us to investigate the correlations between these properties. Figure 4 illustrates the variation of acoustic impedance ($AI$), calculated from the density and vertical compressional P-wave as follows $AI = \rho V_P$, and the ratio of compressional and shear velocities normal to bedding ($V_P/V_S$) versus permeability. Strong correlations ($R^2 > 0.95$) of $AI$ and $V_P/V_S$ ratios with logarithm of hydraulic permeability are observed for all the samples. At the same $AI$, an increase of the quartz fraction shifts the permeability compaction trend to higher permeabilities, while the increase in smectite content results in lower permeabilities. In turn, a $V_P/V_S$ vs permeability plot clearly separates

the samples with the different composition of a clay fraction, whereas variations in quartz content show no significant separation.

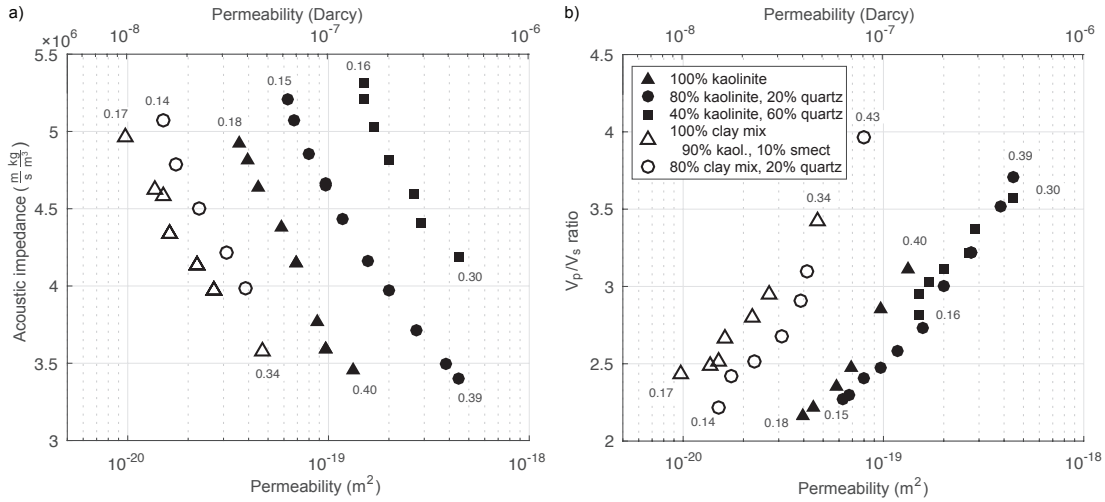


*Figure 44. Correlation of seismic parameters and hydraulic permeability for the compacted samples: a) Acoustic impedance vs permeability and b) $V_P/V_S$ ratio vs permeability. Initial and final porosities are shown by numbers at the endpoints of each sample.*

## DISCUSSION

The unique experimental data on simultaneous evolution in elastic and hydraulic properties of clay rocks during the compaction experiments might be further used to develop rock physics models to describe and predict seismic responses and sealing properties of mudstones at different compaction stages. Modelling of elastic properties of shales generally involves a number of measurable or fitting parameters (e.g. Hornby et al., 1994, Sayers, 2005, Ortega et al., 2010, Vasin et al., 2013, Pervukhina et al., 2011). Some authors build their models on a large number of parameters, which include "exotic" parameters that are rarely measured in laboratories (for instance, orientation distribution function (ODF) of clay platelets) or fitting parameters that are not measurable at all such as aspect ratios of fluid inclusions. Other authors reduce the number of parameters to two or three measurable ones, such as porosity and silt fraction to ensure predictive power of their models. Regardless of the chosen tactic and the claimed number of fitting parameters, all these models require knowledge of elastic properties of pure clays that cannot be experimentally measured as it is not found in nature. A number of attempts have been made to derive these properties from experimentally measured data (e.g. Pervukhina et al., 2008), to measure them directly on a microscale (e.g. Ortega et al., 2010) or to calculate from the first-principles based on the density functional theory (e.g. Militzer et al., 2011).

The compaction trends of the five independent elastic coefficients of a pure clay matrix can be consistently approximated by a linear relationship ($R^2 > 0.8$) at a porosity range of 15–40 %:

$$C_{ij} = a_{ij} - b_{ij}\ \phi. \tag{16}$$

Here the elastic coefficients are in GPa and the porosity is in fractions. The coefficients $a_{11}, a_{33}, a_{13}, a_{44}$, and $a_{66}$ (all in GPa) are equal to 29.7 (28.2), 14.9 (14.8), 9.6 (8.5), 4.7 (3.6), and 8.9 (7.6); and $b_{11}, b_{33}, b_{13}, b_{44}$, and $b_{66}$ are 58.5 (55.8), 25.3 (25.1), 12.1(10.6), 11.3 (8.9), and 20.4 (18.2), where the coefficients for a smectite-kaolinite mixture are shown in brackets. The silt fraction also has a first order effect on the elastic coefficients of shales as can be seen in Figure 42 (b, c, and e). As was shown by Beloborodov et al. (2016a), the effect of up to 25 % of the silt fraction on the elastic coefficients can be accurately modelled using anisotropic differential effective medium approach (Nishizawa, 1982) and the ODF of clay platelets (that was

illustrated to be somewhat perturbed by silt inclusions) has a noticeable impact on elastic coefficients at silt fractions of $> \sim 40$ %.

Modelling studies predict that elastic anisotropy of mudstones increases with mechanical compaction (e.g. Dræge et al., 2006, Bachrach, 2011). My experimental results show that while P-wave anisotropy does increase with the porosity reduction, S-wave anisotropy might decrease with compaction (Figure 2, right hand side plots). This fact implies that the alignment of anisotropic clay particles that improves with compaction (and can be quantified by measuring their ODFs) is not the only factor that contributes to their elastic anisotropy. The decrease of anisometric (spheroidal or penny shaped) porosity is a factor that can be responsible for the elastic anisotropy decrease with compaction. These two competing factors might lead to incoherent changes in P-wave and S-wave anisotropy. Another factor that reduces both ε and γ is the increase of the silt fraction. While porosity decrease from 0.35 to 0.15 results in the increase of ε from 0.2 to 0.4 (Figure 2a), the increase of the silt fraction from 0 to 0.2 decreases ε back to 0.2 at porosity of 0.15. This effect as well as differences in depositional environments that result in drastically different shale anisotropy (Beloborodov et al., 2016b) prompt Pervukhina and Rasolofosaon (2017) to conclude that compaction does not have a first order effect on elastic anisotropy of shales. The presence of 10 % of smectite does not significantly affect the elastic anisotropy, however the effect of clay mineralogy on anisotropy should be more thoroughly investigated.

The permeability of the compacted shales shows an exponential decay with the decrease in porosity and strongly depends on silt fraction and clay mineralogy. The multiple linear regression (MLR) was used to quantitatively capture the effects of porosity, silt fraction and mineralogy on permeability. As the effect of silt fraction is definitely different in the case of smectite presence, I build separate MLR models for shales with different clay mineralogy, namely, for 100 % kaolinite clay matrix:

$$\log_{10}(\kappa) = -20.13 + 3.67\phi + 0.02 f_s, \tag{17}$$

and for 90 % kaolinite and 10 % smectite:

$$\log_{10}(\kappa) = -20.55 + 3.29\phi + 0.01 f_s. \tag{18}$$

where $\kappa$ is permeability in $m^2$, $\phi$ and $f_s$ are porosity and silt fraction, respectively.

The porosity (i.e., degree of compaction) and silt fraction have a first order effect on elastic coefficients and hydraulic permeability of shales. Elastic coefficients of clay

matrixes exhibit linear trends with compaction from porosity of $> 35$ to 15 %. Hydraulic permeability shows an exponential decay with the decrease of either porosity or silt fraction. A small fraction of 10 % of smectite added to a kaolinite clay matrix decreases permeability by half an order of magnitude and flattens the increasing trends with the increase of porosity and silt fraction. On the contrary, 10 % of smectite added to the kaolinite clay matrix does not strongly affect elastic coefficients or anisotropy parameters, but noticeably increases the $V_P/V_S$ ratio at the same porosity.

## SUMMARY OF CHAPTER 4

A newly developed experimental rig enables full characterization of the evolution of anisotropic elastic properties in shales during the mechanical compaction. The pressure-oscillation technique has been used for acquisition of the permeability compaction trends in shales.

Hydraulic permeabilities of artificially compacted shale samples are comparable to the natural ones. Permeability drops exponentially with compaction. Silt fraction and clay mineralogy are the two key parameters that might be responsible for broad variations of permeability in shales at the same porosity. I show the feasibility and provide examples of obtaining the empirical equations for calculating the permeability if porosity and silt fraction are known.

Elastic coefficients of clay matrix exhibit positive linear trends with the porosity decrease. The presence of 10 % of smectite in a clay matrix has a minor effect on the absolute values of elastic coefficients or anisotropy but leads to a noticeable increase in the ratio of compressional to shear velocity ($V_P/V_S$) normal to the bedding at the same porosity. Finally, the strong correlations ($R^2$ above 0.95) of the hydraulic permeability with the acoustic impedance and $V_P/V_S$ ratio are observed for all the prepared samples. These trends are different for the samples with different mineral composition, illustrating the impossibility of predicting the permeability of shales from seismic data without prior knowledge on their mineral composition.

# Chapter 5 – Experimental characterization of the dielectric properties of artificial shales[5]

## INTRODUCTION

High dielectric contrast between water and hydrocarbons provides a useful method for distinguishing between producible layers of reservoir rocks and the surrounding media. The dielectric response at high frequencies is related to the moisture content of rocks. Correlations between the dielectric permittivity and specific surface area are also helpful for the estimation of the elastic and geomechanical properties of rocks. Another valuable application of dielectric properties is the design of modern techniques for hydrocarbon extraction in unconventional reservoirs, where the knowledge of dielectric loss-factor and relaxation frequency in the rock is critically important for effective production. Although capabilities of this method are intriguing, the data interpretation is very challenging due to many factors influencing its behaviour. For instance, the dielectric permittivity is determined by the mineralogical composition of a solid fraction, volumetric content and chemical composition of saturating fluid, rock microstructure and geometrical features of its solid components and pore space, temperature and pressure. In this chapter, I investigate the frequency dependent dielectric properties of artificial shale rocks prepared from silt-clay mixtures via mechanical compaction. Samples are prepared with various clay content and pore fluids of different salinity and cation compositions. Measurements of dielectric properties are conducted in two orientations to investigate the dielectric anisotropy as the samples acquire strongly oriented microstructures during the compaction process.

[5] This chapter is an extended version of a scientific paper by BELOBORODOV, R., PERVUKHINA, M., HAN, T. & JOSH, M. 2017. Experimental Characterization of Dielectric Properties in Fluid Saturated Artificial Shales. Geofluids, 2017, 8.

## RESULTS AND DISCUSSION

Twelve artificial shale samples are prepared via the laboratory mechanical compaction. The preparation of the samples and measurement setup is described in Chapter 2 of the thesis. All the samples were measured with parallel plates technique normal to the bedding plane (Figure 45a) and parallel to it (Figure 45b) to investigate the dielectric anisotropy.

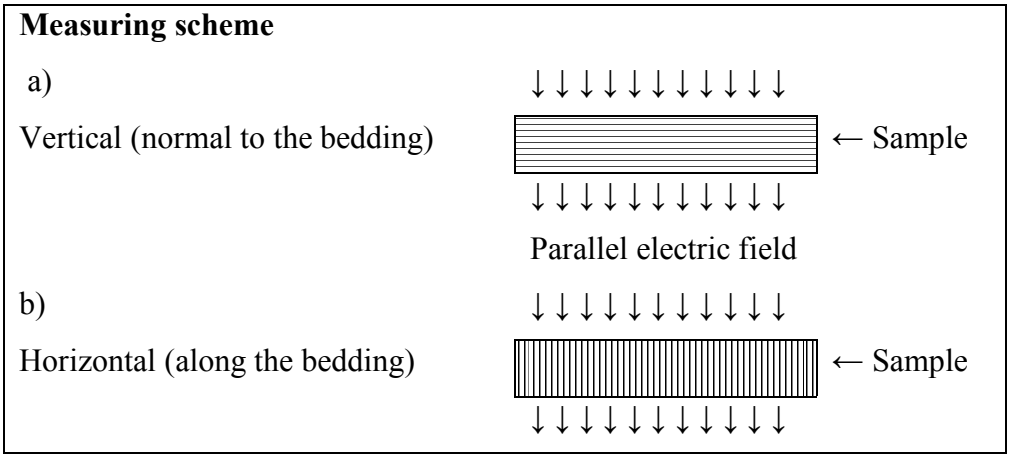


*Figure 45. Parallel plate measurement schematics.*

Summary of all the prepared mixtures is shown in Table 6. Sample names have specific nomenclature where the first letter stands for either aggregated (A) or dispersed (D) clay microstructure, the following numbers indicate the weight ratio of quartz to kaolinite constituents in percent, and the last number shows the salinity of pore fluid in g/l.

*Table 6. Specification of the samples*

| Name | Type of clay microstructure | Clay content (%) | Porosity (%) | Salinity (g/l) | Salt |
|---|---|---|---|---|---|
| D0100_0 | Dispersed | 100 | 21 | 0 | – |
| D4555_0 | Dispersed | 55 | 10 | 0 | – |
| C4 | Dispersed | 75 | 28 | 0 | – |
| C5 | Dispersed | 60 | 23 | 0 | – |
| A1090_0 | Aggregated | 90 | 13 | 0 | – |
| A0100_10 | Aggregated | 100 | 10 | 10 | NaCl |
| A0100_34 | Aggregated | 100 | 26 | 34 | NaCl |
| A0100_75 | Aggregated | 100 | 18 | 75 | KCl |
| A2575_75 | Aggregated | 75 | 16 | 75 | KCl |
| A4060_75 | Aggregated | 60 | 14 | 75 | KCl |
| C2 | Aggregated | 75 | 23 | 75 | KCl |
| C3 | Aggregated | 60 | 24 | 75 | KCl |

Dielectric properties are presented in Figures 46–53 for different parameters, namely, the salinity of pore fluid, its cation composition, clay content, and the type of initial clay microstructure. Figure 46 illustrates the positive linear trends of real dielectric permittivity vs porosity for the samples prepared with brine and fresh water separately. The dielectric response at frequencies of > 1 GHz range is usually attributed to the dipole polarisation of water molecules and might be used to estimate the amount of water in the pore space. Linear correlation decreases with a decrease in frequency from $R^2 = 0.95$ at 100 MHz to $R^2 = 0.70$ at 10 MHz due to contributions from other polarisation mechanisms occurring at lower frequencies (e.g. surface-charge polarisation). Although it is believed that the brine salinity has no effect on the dielectric response of saturated rock samples at high frequencies, our experimental results show clearly separated trends for the two groups of the artificial shale samples prepared with brine and fresh water. This difference is attributable to the changes occurring in the electric double layer of clays in the presence of electrolyte. In the samples saturated with highly concentrated brine the positive ions of Na and K compensate the free charges on the surfaces of clay particles. Therefore, the diffuse layer of weakly bound water around the clay particles significantly shrinks (Bohinc et al., 2001, Brown et al., 2016) and leaves more free water molecules that are easily polarisable within the sample. On the other hand, the samples prepared with fresh water exhibit thick hydrate envelopes around the clay particles thereby hindering the large amount of water dipoles from polarisation in the presence of an electric field. In my experimental results, the described effect results in one order of magnitude difference between the samples saturated with brine and fresh water samples on a wide range of porosity at megahertz frequencies. It is also important to note that the number of active cations in brine saturated samples seem to have a negligible effect on dielectric permittivity in the dipole polarisation frequency range as all the samples prepared with different concentrations and compositions of brine follow the same linear trends. Using the linear trends described above, it is possible to compare different samples at the same porosity. These trends are used to investigate the effects of clay content, salinity and microstructure.

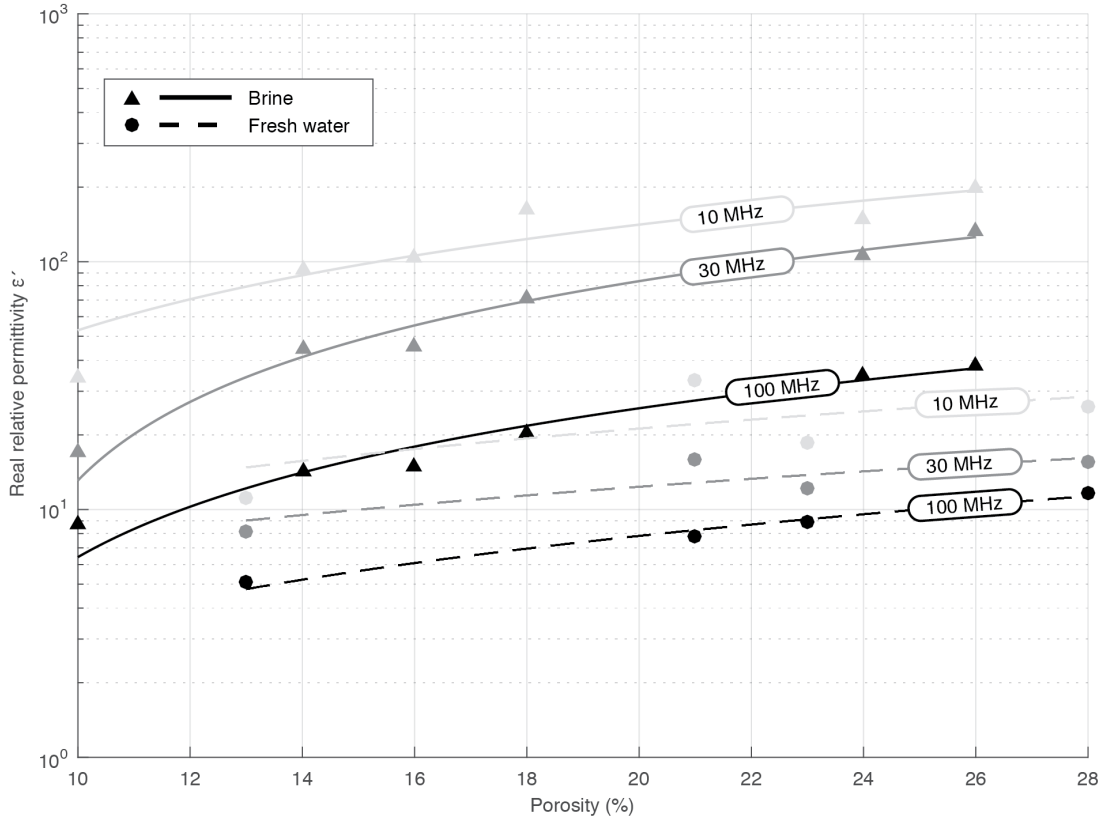


*Figure 46. Dielectric response of brine saturated and fresh water samples at 100, 30, and 10 MHz.*

Figure 47 shows that across the wide range of frequencies horizontal conductivity in different samples is almost always higher than the vertical one. Previously we showed that the particles of clay and silt tend to orient with compaction normal to the direction of an applied compaction stress (Beloborodov et al., 2016b, Beloborodov et al., 2015). Therefore, the interconnected pore network in artificial shale samples is also more oriented in the bedding direction and provides an effective pathway for charge carriers, whereas in the direction normal to the bedding the conductive pathways exhibit greater tortuosity and obstruct the movement of charges. The conductivity anisotropy also increases with porosity reduction as the microstructure becomes more oriented in the horizontal direction. Both horizontal and vertical conductivities increase with increasing porosity. At high frequencies, the influence of fluid conductivity grows with the increase of the pore volume occupied with water solution.

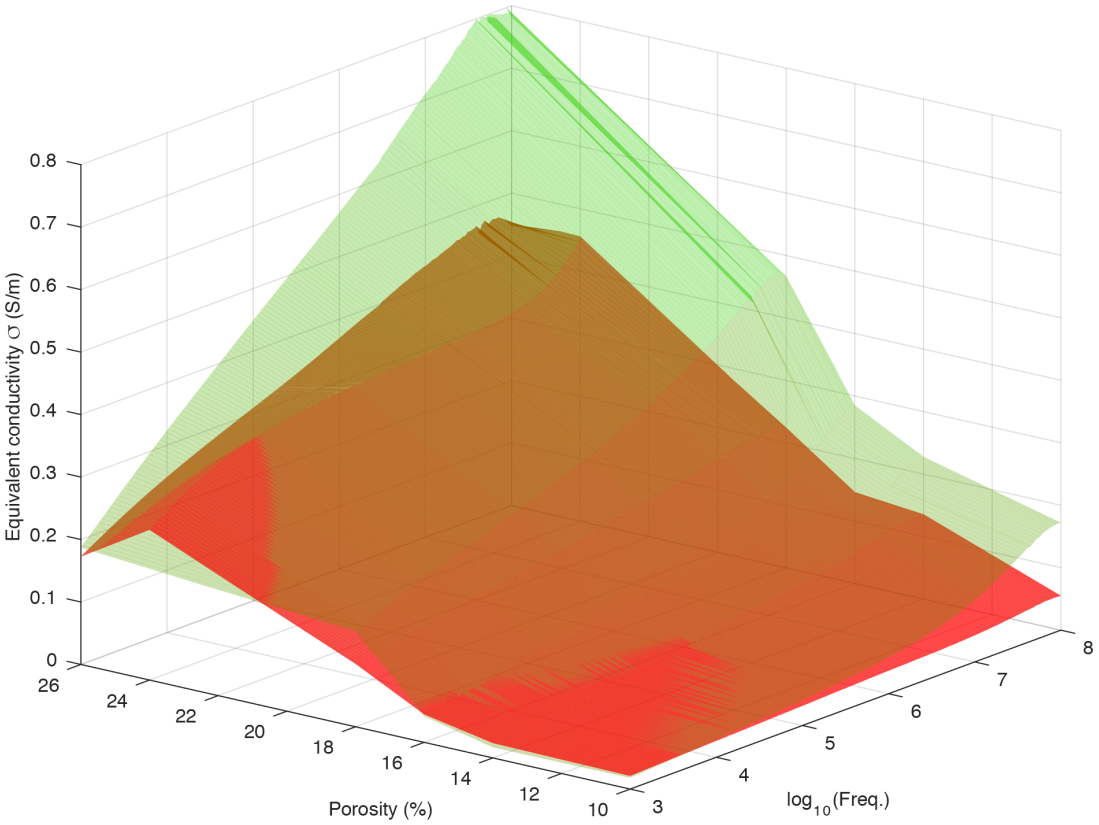


*Figure 47. Surface plot of conductivity, measured parallel (in green) and normal (in red) to the bedding, vs porosity and frequency in 6 brine saturated artificial shale samples.*

The frequency dependent dielectric anisotropy in eight artificial shale samples is shown in Figure 48. The dashed line on the plot corresponds to the isotropic system, while all the points above and below this line correspond to the anisotropic system with polarisation effects dominating in horizontal and vertical directions, respectively. It is important to note that the fresh water samples are always better polarised in horizontal direction and reside above the isotropy line, whereas the brine saturated samples are better polarised in the vertical direction at lower frequencies and exhibit inversion of the anisotropy with crossover points in megahertz range.

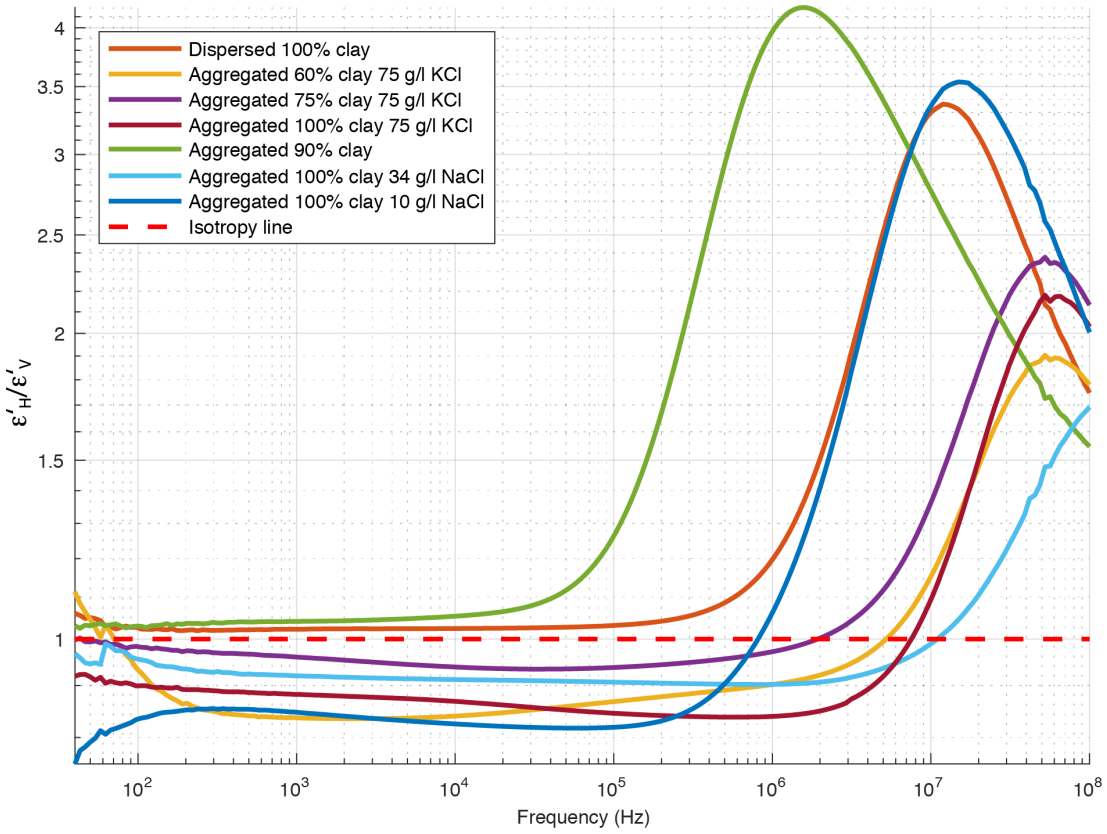


*Figure 48. Dielectric anisotropy vs frequency in brine saturated and fresh water samples.*

The anisotropy curves for all the samples exhibit peak values in megahertz range and their maximum values and frequency distributions are determined by the type and concentration of salt ions in the saturating fluid. Thus, the samples prepared with fresh water or low concentration fluids show the highest anisotropy peaks located at the lower end of megahertz range. Then follow the three peaks at the same frequency of ~60 MHz corresponding to the samples saturated with KCl brine. The lowest peak belonging to the sample saturated with NaCl brine occurs at frequencies above 100 MHz. The crossover points with the isotropy line in brine saturated samples are also distributed across the megahertz frequency, similarly to the peak values, but at lower frequencies.

This anisotropic behaviour may be explained by electric double layer theory. Given that the clay particles in fresh water samples have thick hydrate envelopes of weakly bound water, the dipole polarisation of water molecules is achieved more easily in the parallel to the bedding plane simply due to the fact that the clay particles in all the samples are mostly oriented in the horizontal direction. Hence, water molecules are oriented with their hydrogen atoms towards the surfaces of clay particles

and are easily skewed sideways under the influence of an electric field parallel to the bedding but resist the influence of normal electric field. In the brine saturated samples this effect is less pronounced across the wide frequency range due to the significantly thinner diffuse part of the double electric layers where the above phenomenon occurs. Therefore, considering the distinctive features of dielectric anisotropy in artificial samples, one might infer that the anisotropy analysis can help with the understanding of composition and concentration of saturating fluids in clay rocks. However, more data on artificial and natural rocks need to be analysed to confirm the discussed relationships.

Figure 49 shows that the increase of clay content at the same porosity results in greater conductivity in both vertical and horizontal directions. This behaviour is caused by the surface conduction mechanisms characteristic to clay particles. It has been shown that the counter ions located in the Stern layer of clay particles are the dominant contributors to surface conduction and in brine saturated rocks with salinity above 1 mol/l the mobility of K and Na ions develops 1/10 of that in the free fluid and is independent of the salinity (Revil and Glover, 1998). Therefore, in our experiments replacing the fraction of quartz with clay particles having much more uncompensated charge results in proportionally stronger surface conduction.

Figure 50 shows that the conductivity of the samples prepared with dispersed clay microstructure is always higher than that of the aggregated sample in both directions independently of the silt content and porosity. This is due to the greater surface conduction in the Stern layer of the dispersed samples where the clay particles are separated from each other and have greater free surface than their associations in the aggregated sample.

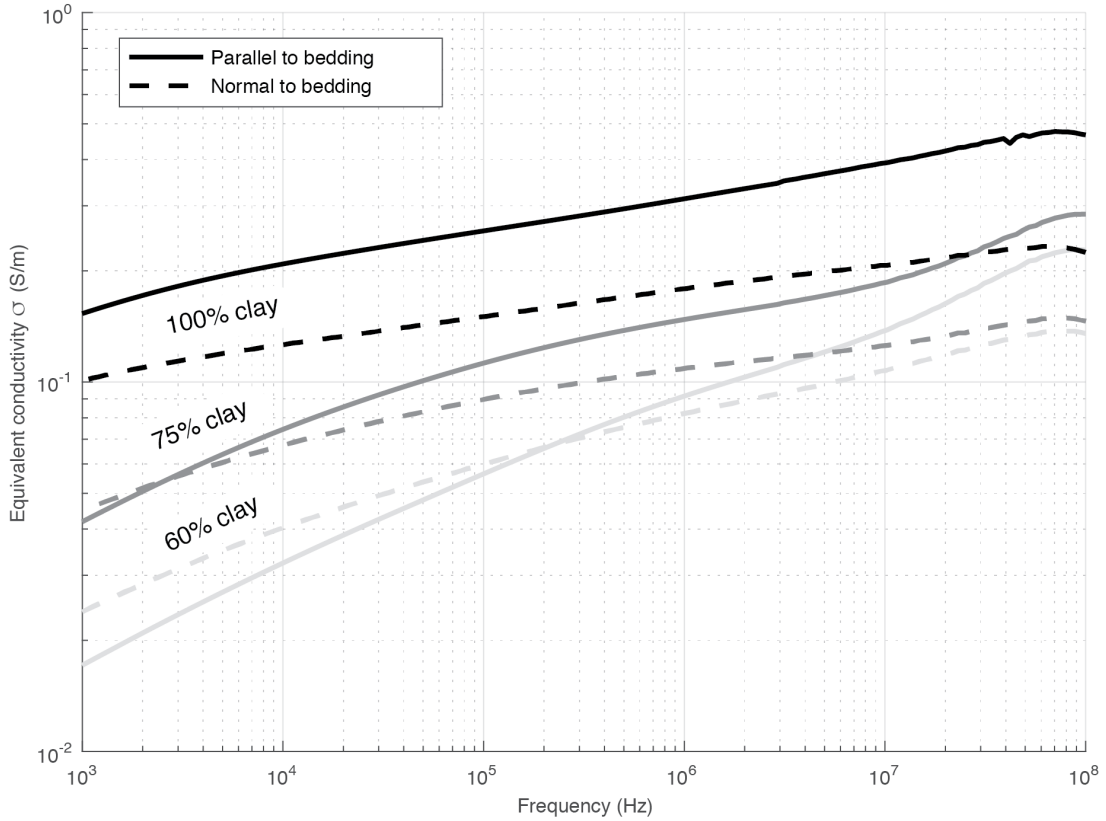


*Figure 49. Effect of clay content on frequency dependent conductivity in the samples measured parallel and normal to the bedding plane.*

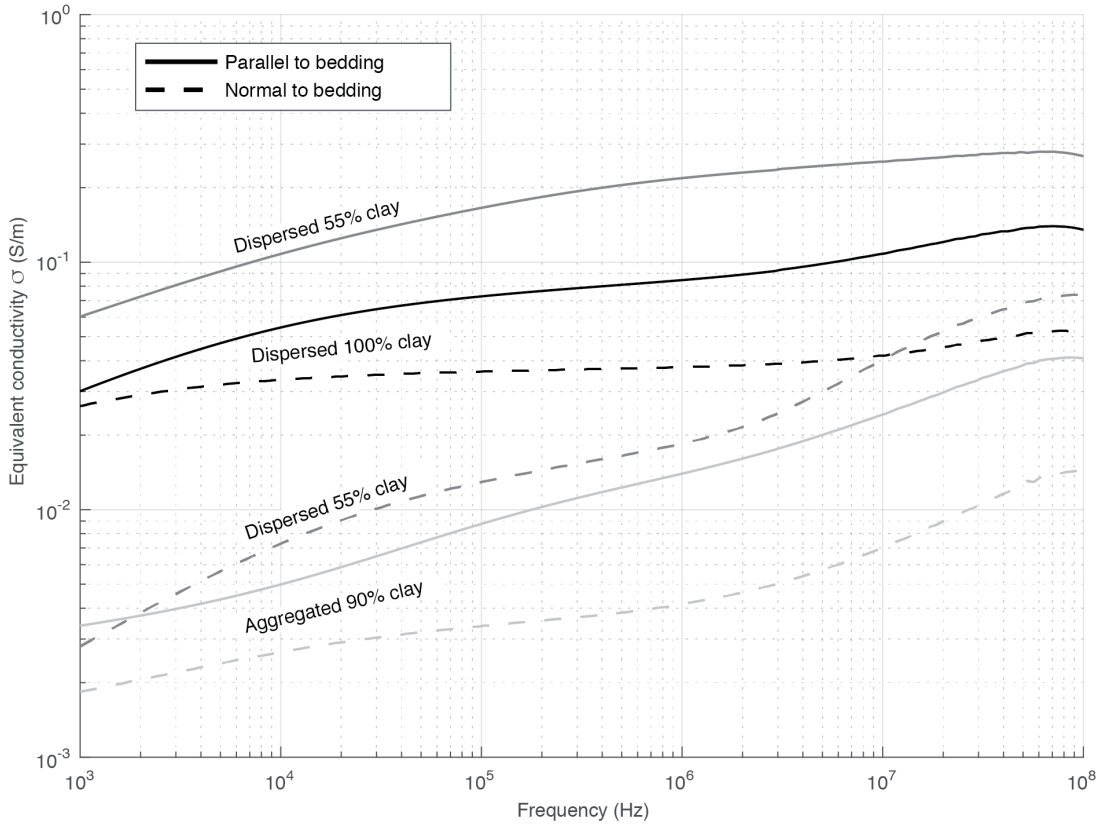


*Figure 50. Effect of microstructure on the conductivity of the artificial shales.*

At frequencies in the range of 1 kHz to 100 MHz the vertical polarisation dominates in the brine saturated samples as shown in Figure 51. The main polarisation mechanism in this frequency band is the Maxwell-Wagner polarisation of counter ions. The movement of ions in the vertical direction is restricted due to the strong orientation of clay particles normal to the applied electric field and the force balance within their electric double layers. In this case, each individual clay particle acts as a capacitor and the ensemble of such particles gives rise to strong polarisation effects exceeding that of individual fluid and mineral phases (Sen and Chew, 1983). In contrast, the cations can be easily drawn along the surface of clay platelets and through the less tortuous pore network along the bedding. Thus, in the presence of a low frequency electric field (below megahertz) in the direction normal to the bedding hydrated counter ions are prone to polarisation rather than to conduction and vice versa for the electric field in the bedding direction. Also, it is important to note that the higher the clay content the more polarisation effects are pronounced in both directions due to the higher concentration and the better alignment of clay platelets given the same porosity level (Beloborodov et al., 2016b).

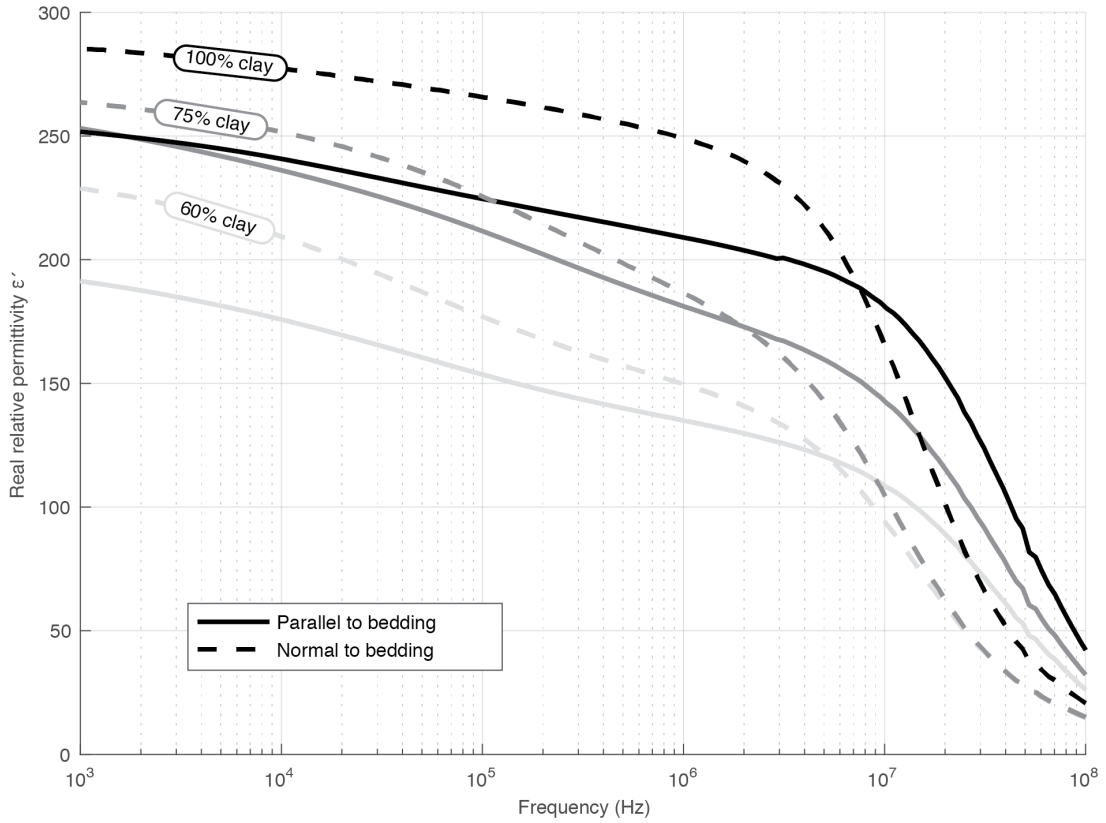


*Figure 51. Dielectric response of three brine-saturated artificial shale samples with clay contents of 60, 75, and 100 per cent.*

Figure 51 shows the rollover of real relative permittivity in the MHz range of frequencies for both the vertical and horizontal measurements. According to Kramers–Krönig relationship (Kremer and Schönhals, 2002) these rollovers correspond to the peaks on the plots of imaginary relative permittivity in Figure 52. Peak values of dielectric loss-factor in vertical direction appear at approximately one order of magnitude lower frequencies and are ~20% higher than those measured in horizontal direction. One must take these effects into account designing the borehole heating antennas for effective hydrocarbon extraction in unconventional reservoirs. Also, samples with higher clay content show the higher values of loss-factor due to the sharper rollover in the real relative permittivity caused by the change in polarisation mechanism from surface-charge to dipole polarisation with the increase of frequency.

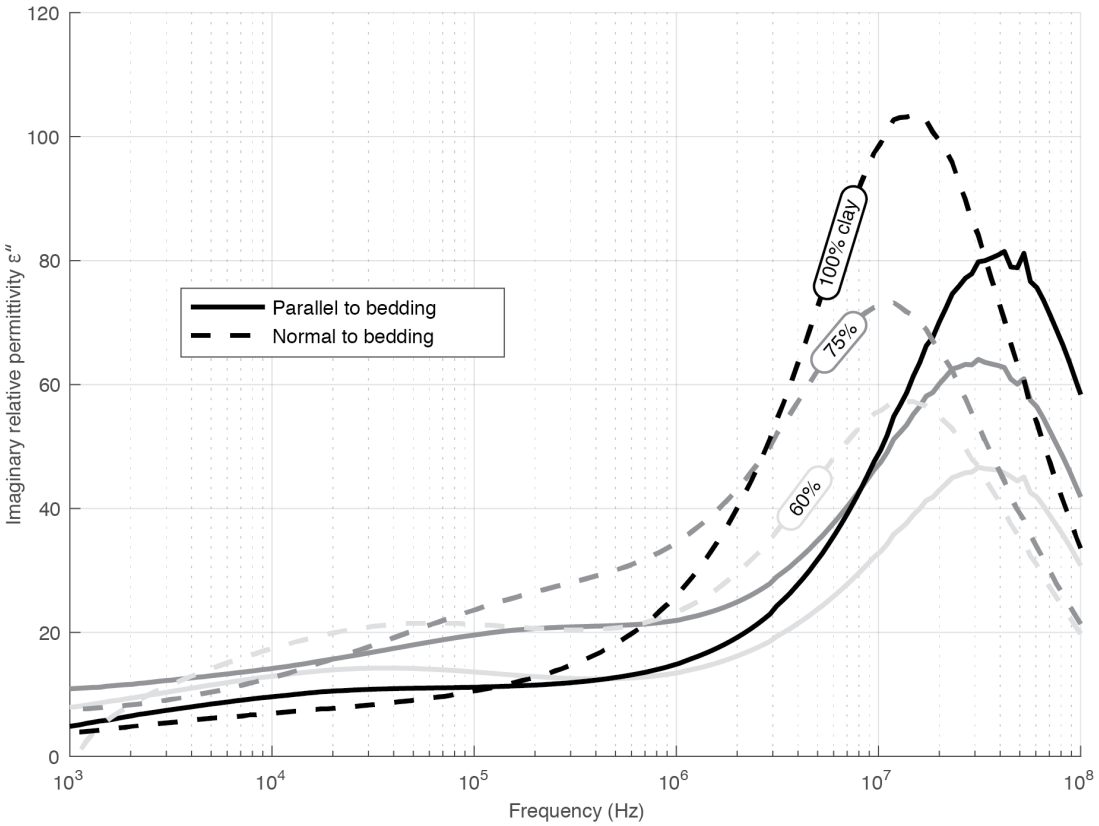


*Figure 52. Frequency dependent dielectric loss in artificial shales with varying clay content.*

Figure 53 illustrates the dielectric loss-factor for the three samples saturated with different brine cation composition and concentration. All the peaks are located at MHz range for the measured samples. The distribution of the peaks at different frequencies depends on the salinity of a pore fluid and its cation composition. Hence, increasing the salinity from 10 to 34 g/l in the pure kaolinite sample saturated with NaCl results in change of peak frequency from $2\times10^6$ to $3\times10^7$ Hz. Sample saturated with 75 g/l NaCl solution exhibits the peak frequency of $4\times10^7$ which highlights the effect of different salt ions on the dielectric loss-factor of clay rocks.

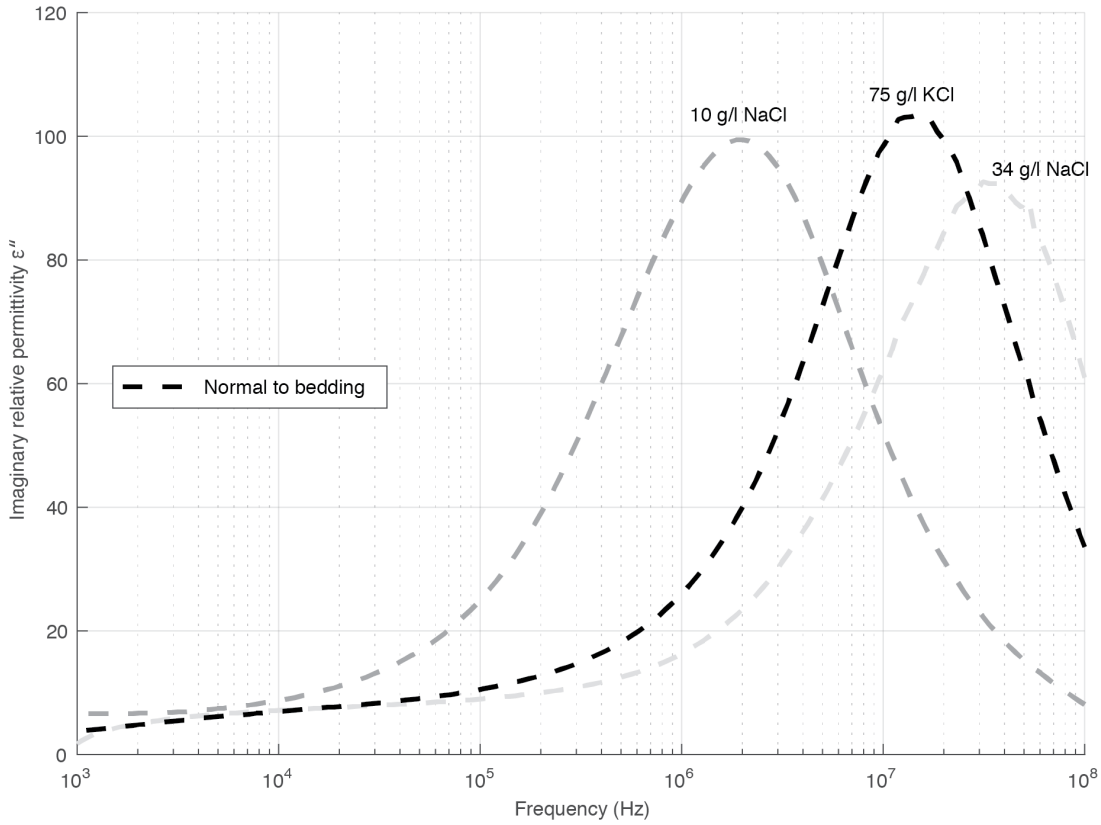


*Figure 53. Frequency dependent dielectric loss in artificial shales saturated with different brine.*

## SUMMARY OF CHAPTER 5

Artificial shales with a simple mineral composition illustrate the broad frequency dispersion of dielectric effects. The variations in salinity of the connate water, its cation composition, clay content and microstructure significantly affect complex dielectric permittivity and conductivity of artificial shales. These effects can be explained by the Maxwell-Wagner polarisation effects at frequencies below megahertz range and the changes occurring in the double electric layer of clay particles in the presence of electrolyte at higher frequencies.

It is shown that at a frequency range between 10 and 100 MHz real relative permittivity has different linear trends with porosity in fresh water and brine saturated samples. The salinity and cation composition of the pore fluid seem to have negligible effect on these high frequency dielectric trends.

The formation of anisotropic microstructure of artificial shales during mechanical compaction results in significant values of dielectric anisotropy between 2 and 4. The magnitude and the characteristic frequency of the peak values in anisotropy curves as well as the crossover with isotropy point depends on the salinity, cation composition of saturating fluid, and clay content.

The absolute peak value of dielectric loss in shales and its characteristic frequency depends not only on the amount of connate fluid, but also on the cation composition of the saturating brine, its salinity, and the orientation of an applied electric field relative to the shale bedding. The peak values of the dielectric loss measured along and normal to bedding lay within the megahertz frequency range with significant separation of approximately 1 order of magnitude. The absolute values of these peaks are approximately 20 per cent higher in the direction normal to the bedding.

The prepared shale samples illustrated the complex dielectric behaviour similar to that of the real rocks. The theoretical modelling of dielectric response is conducted in the following chapter illustrating the use of artificial shales for design and calibration of the rock physics models.

# Chapter 6 – Theoretical modelling of the dielectric properties in artificial shales[6]

## INTRODUCTION

Accurate modelling of the anisotropic dielectric properties of shales is important for the interpretation of dielectric data measured in lean and organic-rich shales forming geological traps and unconventional reservoirs, respectively. A multiphase incremental model is developed for the frequency dependent anisotropic dielectric properties of sedimentary rocks. An example of application of the developed model to simulate the measured anisotropic dielectric behaviours of artificial shales is given.

The new model was built on the theoretical basis of differential effective medium models for any number of mineral grain components aligned in any direction and was shown to be independent of the mixing order. The model incorporates the measured orientation distribution function of clay particles to determine the dielectric anisotropy of shale. The frequency dependent dielectric behaviours of the wet clay minerals are obtained by inverting the elastic properties of the pure clay artificial sample composed of the same clay and brine as the modelled samples. The modelling technique combined the important polarisation mechanisms in the intermediate frequency range and was shown to give satisfactory fit to the measured frequency dependent anisotropic relative permittivity and conductivity of the artificial shales with varying silt contents by using a reasonable aspect ratio and constant dielectric parameters for the silt grains.

[6]This chapter is an extended version of a scientific paper by HAN, T., BELOBORODOV, R., PERVUKHINA, M., JOSH, M., CUI, Y. & ZHI, P. 2018. Theoretical Modeling of Dielectric Properties of Artificial Shales. Geofluids, 2018, 12.

## RESULTS

### Anisotropic dielectric model

*Two-phase anisotropic dielectric model*

Based on Maxwell–Wagner theory (Maxwell, 1891, Wagner, 1914), Asami (2002) derived an equation for the complex relative permittivity ($\varepsilon^*$) of a 2-phase mixture where ellipsoidal inclusions (with complex permittivity of $\varepsilon_g^*$) are oriented in the background medium (with complex permittivity of $\varepsilon_a^*$) with the angle $\phi_k$ between the *k*-axis and the electric field, as

$$\varepsilon^* = \varepsilon_a^* \left[ 1 + \Phi \sum_{k=x,y,z} \frac{\varepsilon_g^* - \varepsilon_a^*}{\varepsilon_a^* + (\varepsilon_g^* - \varepsilon_a^*) L_k} \cos^2 \varphi_k \right], \tag{19}$$

where $\Phi$ is the volume fraction of the solid inclusions, the complex relative permittivity $\varepsilon^*$ is defined as

$$\varepsilon^* = \varepsilon' - j\varepsilon'' = \varepsilon + \frac{\kappa}{j\varepsilon_0 \omega}, \tag{20}$$

where $j = \sqrt{-1}$, $\varepsilon'$ and $\varepsilon''$ are the real and imaginary parts of $\varepsilon^*$, respectively, $\varepsilon$ is the relative permittivity, $\kappa$ is the effective conductivity, $\varepsilon_0 = 8.8542 \times 10^{-12}$ F/m is the absolute permittivity of vacuum and $\omega = 2\pi f$ (where $f$ is the frequency in Hz) is the angular frequency of the applied electric field. $L_k$ is the *k*-axis depolarisation factor of the oblate spheroidal inclusions ($R_x = R_y > R_z$, where $R_k$ is the semi-axis of the ellipsoid along the *k*-axis) with the aspect ratio $\alpha < 1$ ($\alpha = R_z / R_x$), given by Asami (2002)

$$L_z = \frac{1}{1-\alpha^2} - \frac{\alpha}{(1-\alpha^2)^{3/2}} \cos^{-1} \alpha, \tag{21}$$

and

$$L_x = L_y = \frac{1 - L_z}{2}, \tag{22}$$

*Multiphase anisotropic dielectric model*

Berg (2007) presented an incremental algorithm to extend the 2-phase Hanai-Bruggeman (HB) equation to more phases without ordering effect. Han et al. (2015) adapted the algorithm to the isotropic dielectric model of Asami (2002). In this work,

the incremental concept is applied to the 2-phase anisotropic dielectric model (Equation 19) to enable more mineral components to be modelled.

In the new multiphase (*m*-phase) anisotropic dielectric model, the second phase with a volume fraction of $C_2/n$ (where $C_2$ is the initial concentration of phase 2 and $n$ is the incremental number) is first added into the water (the first phase) background, forming an effective medium for the next step (step 2 as shown in Figure 54) in which phase 3 with a volume fraction of $C_3/n$ is then included to form an effective background for step 3. This procedure continues until the $m$-th phase with the volume fraction of $C_m/n$ is finally added. The effective medium formed when the $m-1$ phases are included in each increment becomes a background for the next increment until the incremental number of $n$ is reached. The effective medium formed in each step is assumed to be an effective single phase, and the 2-phase anisotropic equation (Equation 19) is used to calculate the effective dielectric properties in the directions parallel and perpendicular to the applied electric field, respectively.

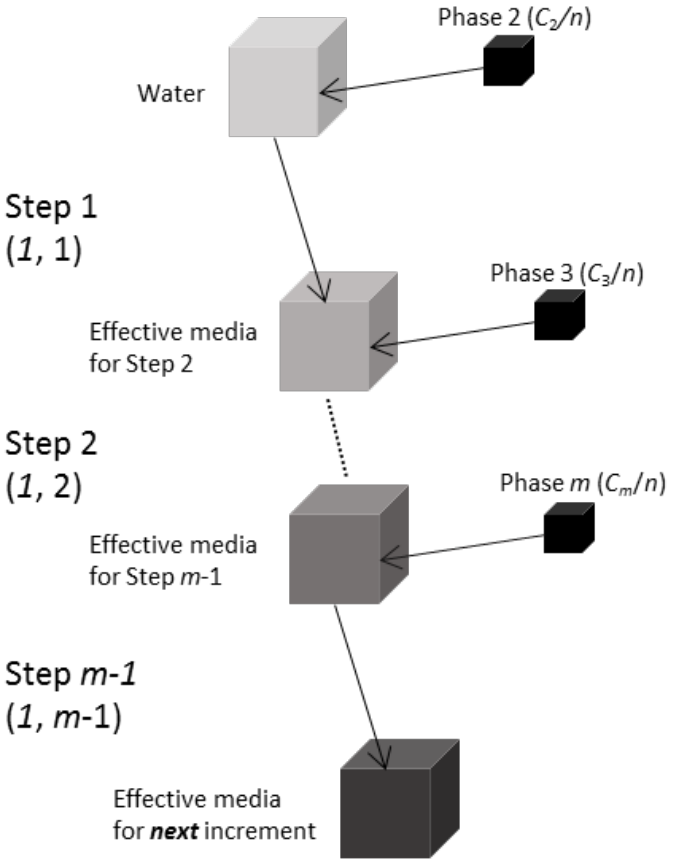


*Figure 54. Schematic diagram showing the steps used in the first increment in the multiphase anisotropic dielectric model, in which water is the starting medium. The*

*effective medium formed in the last step of each increment becomes the starting background for the next increment.*

In the incremental algorithm, an inclusion is added into an effective background medium displacing the equivalent volume. Following Han et al. (2015), it is convenient to derive the volume fractions of the inclusions ($V_i, i = 1{:}\, m$) based on their initial concentrations $C$ and the incremental number $n$.

In the first increment (indicated by the column number), the volume fraction of each component after phase 2 is included (step 1, denoted by the row number):

$$\begin{aligned} &V_1(1,1) = 1 - C_2/n, \\ &V_2(1,1) = C_2/n, \\ &V_3(1,1) = 0, \\ &V_m(1,1) = 0, \end{aligned} \tag{23}$$

the volume fractions of the constituents when phase 3 is added (step 2) are calculated as

$$\begin{aligned} &V_1(1,2) = V_1(1,1) \cdot (1 - C_3/n), \\ &V_2(1,2) = V_2(1,1) \cdot (1 - C_3/n), \\ &V_3(1,2) = C_3/n, \\ &V_4(1,2) = 0, \\ &V_m(1,2) = 0, \end{aligned} \tag{24}$$

the volume fractions of the components when phase 4 is added (step 3) are

$$\begin{aligned} &V_1(1,3) = V_1(1,2) \cdot (1 - C_4/n), \\ &V_2(1,3) = V_2(1,2) \cdot (1 - C_4/n), \\ &V_3(1,3) = V_3(1,2) \cdot (1 - C_4/n), \\ &V_4(1,3) = C_4/n, \\ &V_5(1,3) = 0, \\ &V_m(1,3) = 0, \end{aligned} \tag{25}$$

and after the final step (step $m-1$) when phase $m$ is finally included in the first iteration, the volume fraction of each element can be found by

$$\begin{aligned} &V_1(1, m-1) = V_1(1, m-2) \cdot (1 - C_m/n), \\ &V_{m-1}(1, m-1) = V_{m-1}(1, m-2) \cdot (1 - C_m/n), \\ &V_m(1, m-1) = (C_m/n), \end{aligned} \tag{26}$$

The effective medium in the last step in each increment forms the starting background for the next increment, the volume fraction of each component in the *i*-th increment ($2 \leq i \leq n$), after phase 2, 3, 4 and $m-1$ are added, is therefore given by

$$\begin{aligned}
V_1(i,l) &= V_1(i-1,m-1)\cdot(1-C_2/n),\\
V_2(i,l) &= V_2(i-1,m-1)\cdot(1-C_2/n)+C_2/n,\\
V_3(i,l) &= V_3(i-1,m-1)\cdot(1-C_2/n),\\
V_m(i,l) &= V_1(i-1,m-1)\cdot(1-C_2/n),
\end{aligned} \tag{27}$$

$$\begin{aligned}
V_1(i,2) &= V_1(i,1)\cdot(1-C_3/n),\\
V_2(i,2) &= V_2(i,1)\cdot(1-C_3/n),\\
V_3(i,2) &= V_3(i,1)\cdot(1-C_3/n)+C_3/n,\\
V_4(i,2) &= V_4(i,1)\cdot(1-C_3/n),\\
V_m(i,2) &= V_m(i,1)\cdot(1-C_3/n),
\end{aligned} \tag{28}$$

$$\begin{aligned}
V_1(i,2) &= V_1(i,2)\cdot(1-C_4/n),\\
V_2(i,2) &= V_2(i,2)\cdot(1-C_4/n),\\
V_3(i,2) &= V_3(i,2)\cdot(1-C_4/n),\\
V_4(i,2) &= V_4(i,2)\cdot(1-C_4/n)+C_4/n,\\
V_5(i,2) &= V_5(i,2)\cdot(1-C_4/n),\\
V_m(i,2) &= V_m(i,2)\cdot(1-C_4/n),
\end{aligned} \tag{29}$$

and

$$\begin{aligned}
V_1(i,m-1) &= V_1(i,m-2)\cdot(1-C_m/n),\\
V_{m-1}(i,m-1) &= V_{m-1}(i,m-2)\cdot(1-C_m/n),\\
V_m(i,m-1) &= V_m(i,m-2)\cdot(1-C_m/n)+C_m/n.
\end{aligned} \tag{30}$$

For a given rock sample with known volume fractions of the components (e.g., from laboratory measurements), the initial concentration of each phase for the model input can be determined from Equations 23–30, based on an assigned incremental number $n$.

The modelling results for a hypothetical sample are shown in Figure 55 to demonstrate the effects of mixing order of different inclusions and number of iterations $n$ on simulation results. The sample has a porosity of 0.1 and is composed of brine (with relative permittivity and conductivity of 79 and 4.69 S/m, respectively) and 3 groups of quartz grains aligned at 0°, 30° and 90° to the bedding having volume

fractions of 0.6, 0.2 and 0.1, respectively. The aspect ratios of all the quartz inclusions are assumed to be 0.1, and the relative permittivity and conductivity are taken to be 20 and $10^{-5}$ S/m, respectively. The calculations at each iteration number are done using 6 different mixing orders, as shown in the legend, where 0, 30 and 90 stands for the quartz inclusions oriented at 0°, 30° and 90° to the bedding, respectively and their orders in the legend represent the mixing order. The big separation between the simulated relative permittivity and conductivity when $n$ is set to be 1 confirms the conventional DEM model is dependent on the mixing order of the multiple components (Spalburg, 1988, Cosenza et al., 2009, Han et al., 2011). With an increase of the iteration number, the ordering effect decreases, and the calculated relative permittivity and conductivity at each direction start to converge and become identical when the iteration number is sufficiently high (e.g., $n = 100$), demonstrating the developed multiphase anisotropic dielectric model is independent of the mixing order at high iteration numbers. A further increase in the iteration number will not affect the results but may cause an increase in the computational time. Therefore, unless otherwise stated, an iteration number of 1000 is used for the rest of the calculations to guarantee accuracy of the simulation results in a quick manner.

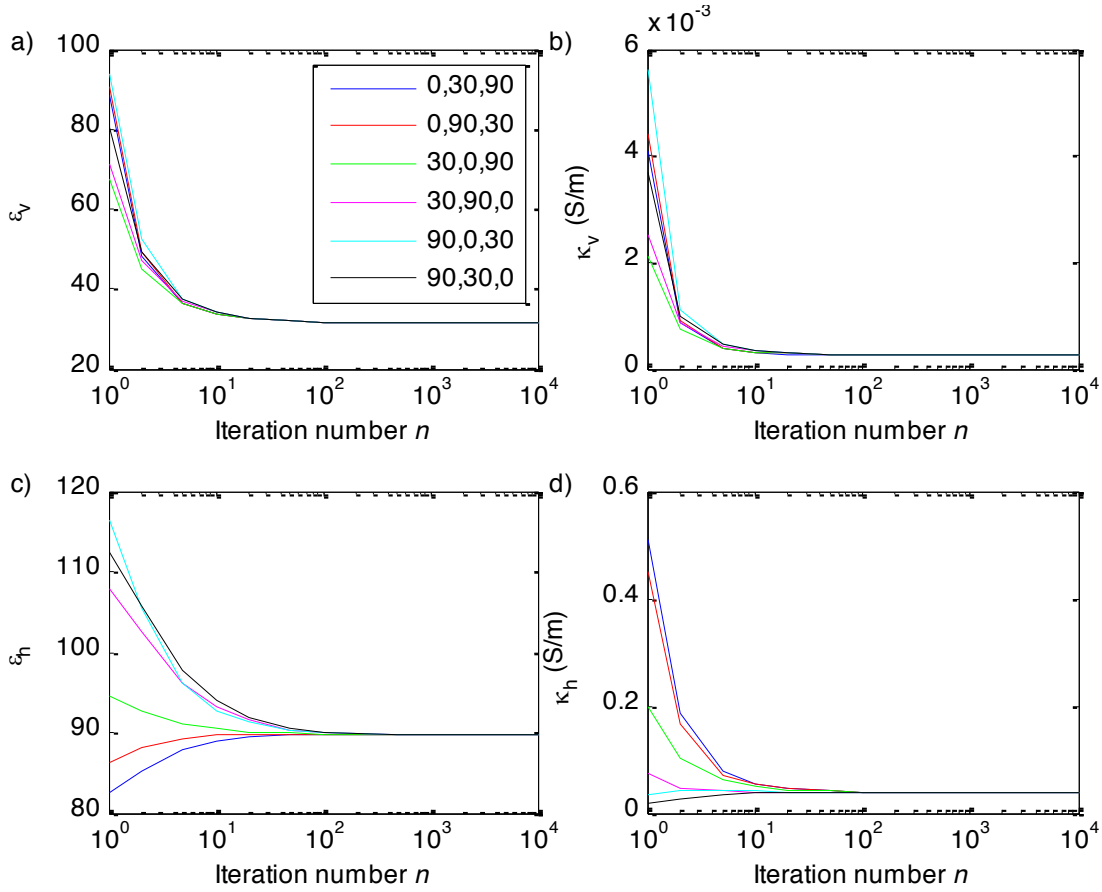


*Figure 55. Simulated relative permittivity and conductivity of the hypothetical sample in the directions when the applied electric field is perpendicular ($\varepsilon_v$ and $\kappa_v$, respectively) and parallel ($\varepsilon_h$ and $\kappa_h$, respectively) to the bedding. The lines with varying colours illustrate the different mixing orders, where 0, 30 and 90 stands for the quartz inclusions oriented at 0°, 30° and 90° to the bedding, respectively.*

**Application to artificial shales**

*Sample selection*

The developed multiphase anisotropic dielectric model is used here for simulating the laboratory measured frequency dependent dielectric responses of the artificial shales. To do this, the frequency dependent dielectric properties of rock-forming components, their volume fractions, and geometric information are needed as the input model parameters. While the dielectric properties of the insulating silt and the conductive water can be considered frequency independent in the frequency range between 0.1 MHz and 100 MHz, there is evidence that the dielectric properties of wet clay minerals are frequency dependent as a result of the Stern layer polarisation

associated with clay minerals (Revil, 2013). Since the magnitude of the Stern layer polarisation depends on the water salinity, the dielectric properties of wet clay minerals are also related to the properties of water. It is therefore reasonable to select a series of samples saturated with the same brine but with varying clay-to-silt ratios so that the frequency dependent dielectric properties of the wet clay minerals at this specific brine conditions can be inverted from the measured dielectric behaviours of the sample with no silt fraction (i.e., the sample composed of only kaolinite and brine). Samples satisfying this criterion include the dispersed samples saturated with distilled water (i.e., samples D0100_0 and D4555_0) and the aggregated samples filled with 75 g/l KCl brine (i.e., samples A0100_75, A2575_75 and A4060_75). However, the dielectric responses of dispersed shales (saturated with the distilled water) are dominated by the Stern layer polarisation that overpowers the Maxwell–Wagner polarisation on which the multiphase dielectric model is based. Therefore, only the aggregated shale samples saturated with 75 g/l KCl are selected for the modelling.

*Determination of the volume fractions of the ingredients*

The measured porosity, silt to kaolinite weight ratios, and the measured orientation distributions of kaolinite particles (as shown in Figure 56 for all the 3 samples in consideration) are used to determine the volume fractions of the ingredients, which are essential for model inputs. The clay particle orientation distributions are measured at polar angle intervals of 5°, giving rise to 19 data points in the range 0° to 90°. Although the multiphase model is developed for any number of phases, the 19 clay phases will significantly increase the computational time. To simplify the clay orientation distributions, but to keep the effects of the distribution density on the dielectric anisotropy, 4 representative angles are chosen instead of using the complete orientation distributions. This is done by averaging the obtained distribution densities between 0° and 15°, 20° and 40°, 50° and 70°, and 75° and 90° to represent the orientation distributions at 0°, 30°, 60°, and 90°, respectively. Considering kaolinite and silt grains are similar in densities, the volume fractions of the kaolinite at the 4 polar angles ($V_{kao}^{i}$) and the volume fraction of the silt ($V_{silt}$) are then determined as

$$V_{kao}^{i} = (1-\varphi)W_{kao}\frac{d_{kao}^{i}}{\sum_{i=0,30,60,90} d_{kao}^{i}}\ , \tag{31}$$

and

$$V_{silt} = (1 - \varphi)W_{silt}, \tag{32}$$

where $\varphi$ is the porosity of the artificial shale sample, $W_{silt}$ and $W_{kao}$ are the preset weight ratio between silt and kaolinite, and $d^i_{kao}$ are the averaged orientation distribution densities at 0°, 30°, 60° and 90° respectively.

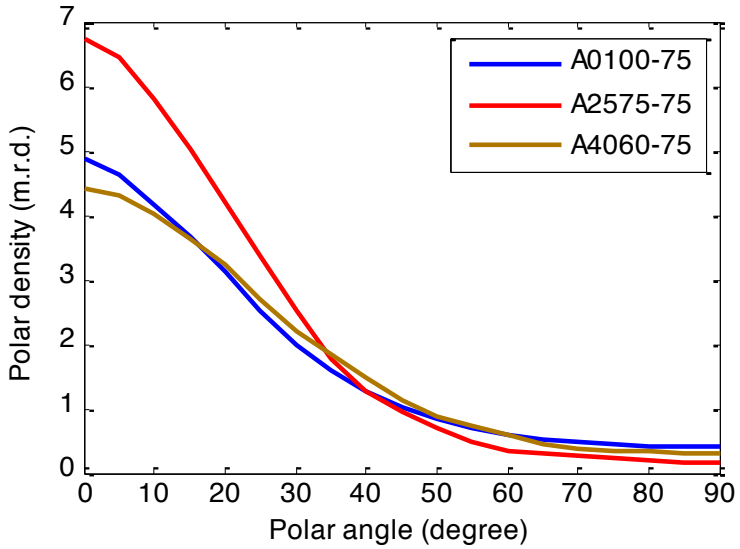


*Figure 56. Experimental c-axis distribution density figures of clay fraction in three samples with corresponding integrated polar angle profiles. Distribution density is expressed in multiples of random distribution (m.r.d).*

The calculated volume fractions of the ingredients for the samples are listed in Table 7, and the initial concentrations of various phases $C$ that are directly input into the model can be obtained from Equations 23–30, based on the assigned incremental number $n = 1000$.

*Table 7. Volume fractions of the rock-forming components for the model input of the samples under investigation. The volume fractions are determined based on the measured porosity of a sample, silt to kaolinite ratio, and the obtained orientation distribution function of kaolinite particles.*

| Sample | $\varphi$ | $V_{silt}$ | $V^0_{kao}$ | $V^{30}_{kao}$ | $V^{60}_{kao}$ | $V^{90}_{kao}$ |
|---|---|---|---|---|---|---|
| A0100_75 | 0.18 | 0 | 0.4756 | 0.2303 | 0.0682 | 0.0459 |
| A2575_75 | 0.158 | 0.2105 | 0.4111 | 0.1792 | 0.0285 | 0.0127 |
| A4060_75 | 0.14 | 0.3440 | 0.2893 | 0.1614 | 0.0429 | 0.0224 |

*Inversion of the dielectric properties of wet clays*

To obtain the unknown dielectric properties of wet clay minerals that are dependent on the connate brine (among many other factors including grain size and temperature), the inversion is conveyed on the measured dielectric properties of the pure kaolinite sample saturated with the same brine as in the other 2 samples, i.e., the 75 g/l KCl brine with relative permittivity of 79 and electrical conductivity of 11.2 S/m. The inversion is done on the sample A0100_75 by minimizing the difference between the laboratory measurements and the model prediction for relative permittivity and conductivity in the directions parallel and perpendicular to the bedding, respectively, at each frequency between 0.1 MHz and 100 MHz where the laboratory data are collected. In the modelling, the average aspect ratio is employed for the kaolinite particles based on the analysis of the SEM images of the compacted sample in Chapter 3.

The results are given in Figure 57 for the inverted frequency dependent relative permittivity and electrical conductivity of the wet kaolinite in the vertical (perpendicular to the bedding, in blue curves) and horizontal (parallel to the bedding, in red curves) directions, respectively. Also shown in Figure 57 is the comparison of the measured shale (A0100_75) relative permittivity and conductivity (vertical and horizontal, respectively) with those predicted using the developed anisotropic model based on the inverted wet clay dielectric properties and their simplified orientation distributions.

The wet clay dielectric properties obtained in the vertical and horizontal directions are for the brine coated oblate kaolinite particles in the directions along the short and long axis, respectively. These properties are thought to be a result of the Stern layer polarisation, that is dependent merely on the brine properties, and are assumed to be the properties of the wet clay in the artificial shales saturated with the same brine. The anisotropic wet clay dielectric properties are further employed to account for the Maxwell–Wagner polarisation through the developed multiphase model to predict the anisotropic dielectric behaviours of the shales with varying amounts of silt fractions. It should be noted that the excellent agreement between the laboratory data and the model prediction as shown in Figure 57c, d is not an indication of the correctness of either the new model or the inverted wet clay dielectric properties, but does imply that the combination of them can sufficiently simulate the measured

frequency dependent dielectric behaviours of the silt-free shale sample. It is therefore reasonable to expect that the joint employment of the developed model and the obtained wet clay dielectric properties could also give satisfactory simulation to the artificial samples with the silt fractions, as to be shown in the following section.

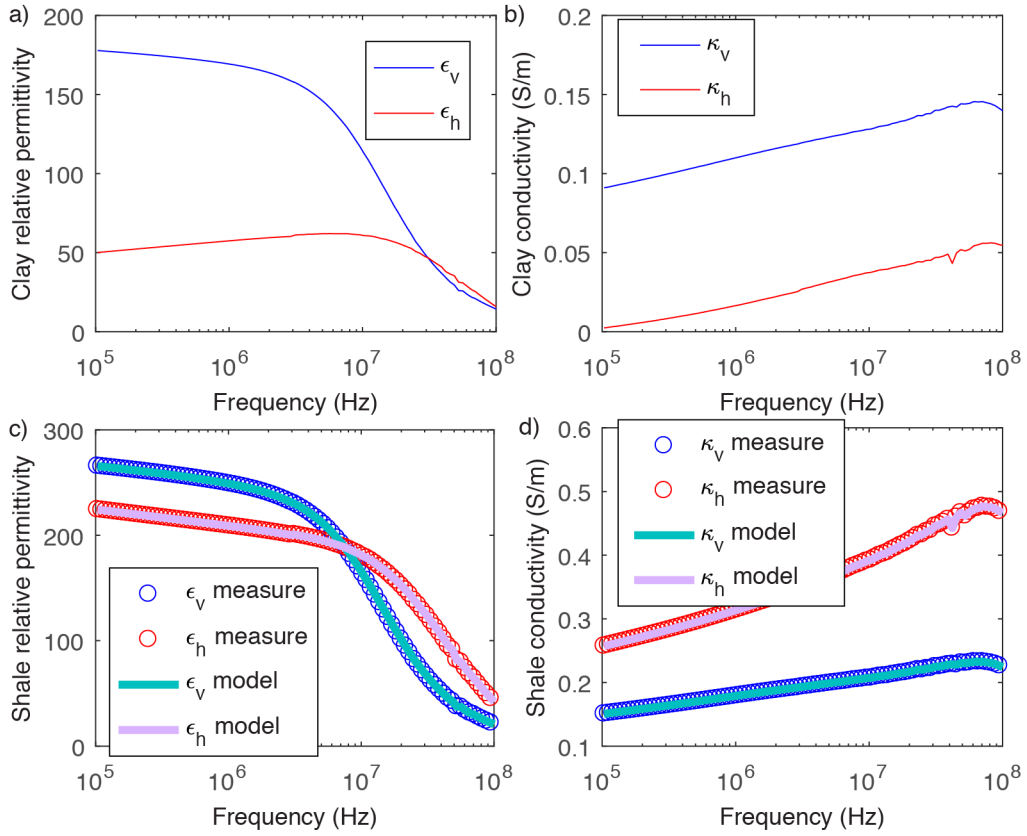


*Figure 57. Inverted frequency dependent relative permittivity (a) and conductivity (b) of the wet kaolinite and comparison of the laboratory measured relative permittivity (c) and conductivity (d) of the shale sample A0100_75 with the model prediction based on the wet kaolinite properties in the vertical and horizontal directions, respectively.*

*Modelling results*

The volume fractions of artificial shale components and the obtained frequency dependent dielectric properties of wet kaolinite aggregates form a basis of the developed multiphase model. It allows simulating the anisotropic responses of the shales with silt inclusions. The inclusion of the silt fraction, however, will add some complexity to the model.

Firstly, the distribution of the silt fractions turns to be random in the kaolinite matrix, making the shale less anisotropic. To adjust the developed multiphase anisotropic dielectric model to be capable of adding isotropic inclusions, the 2-phase

anisotropic dielectric model (Equation 19) is replaced with the 2-phase isotropic model when the silt component is added, given as follows (Asami, 2002)

$$\varepsilon^* = \varepsilon_a^* \left[ 1 + \frac{1}{3} \Phi \sum_{k=x,y,z} \frac{\varepsilon_g^* - \varepsilon_a^*}{\varepsilon_a^* + (\varepsilon_g^* - \varepsilon_a^*) L_k} \right]. \quad (33)$$

Secondly, the dielectric properties of wet silt are unknown. It is well documented in the literature that dry quartz mineral has a relative permittivity of approximately 4.5 (e.g. Olhoeft, 1981), but wet quartz exhibits higher values due to the electrochemical interactions of the mineral-water system. In this work, a constant relative permittivity of 20 (Davis and Annan, 1989, Daniels, 2004) is employed for wet silt with an electrical conductivity of $10^{-5}$ S/m. And lastly, the geometric information (i.e., aspect ratio) of the silt fractions that is required for the model input needs to be determined. In this work, the silt aspect ratio is set as a fitting parameter to give the best correlation between laboratory measurements (both relative permittivity and conductivity) and model prediction in the vertical and horizontal directions, respectively.

The model is applied to the artificial shale samples A2575_75 and A4060_75 using the dielectric properties of the various ingredients together with their volume fractions (as listed in Table 7) and aspect ratios. The modelling results for the artificial shale sample A2575_75 are given in Figure 58. By using the silt aspect ratios of 0.1 and 0.06, the modelled dielectric responses give satisfactory fit to the dielectric measurements with correlation coefficients of $R$ = 0.9833 and $R$ = 0.9775 for the relative permittivity and conductivity in the vertical direction and $R$ = 0.9979 and $R$ = 0.9940 for the relative permittivity and conductivity in the horizontal direction, respectively. The obtained silt aspect ratios of 0.1 and 0.06 are within the aspect ratio range of the silt estimated from the micro-CT image of the compacted sample (Beloborodov *et al*. 2016). It is interesting that different values of the silt aspect ratio are inverted in the orthogonal directions and this can be explained by the fact that although randomly dispersed silts are assumed in the model, they are in fact aligned to some extent, and therefore their contributions to the dielectric responses at different directions are varying, as a result, different values for the silt grain aspect ratio should be used. This is similar to the distinct wet clay dielectric properties that are employed to model the anisotropic shale properties in different directions.

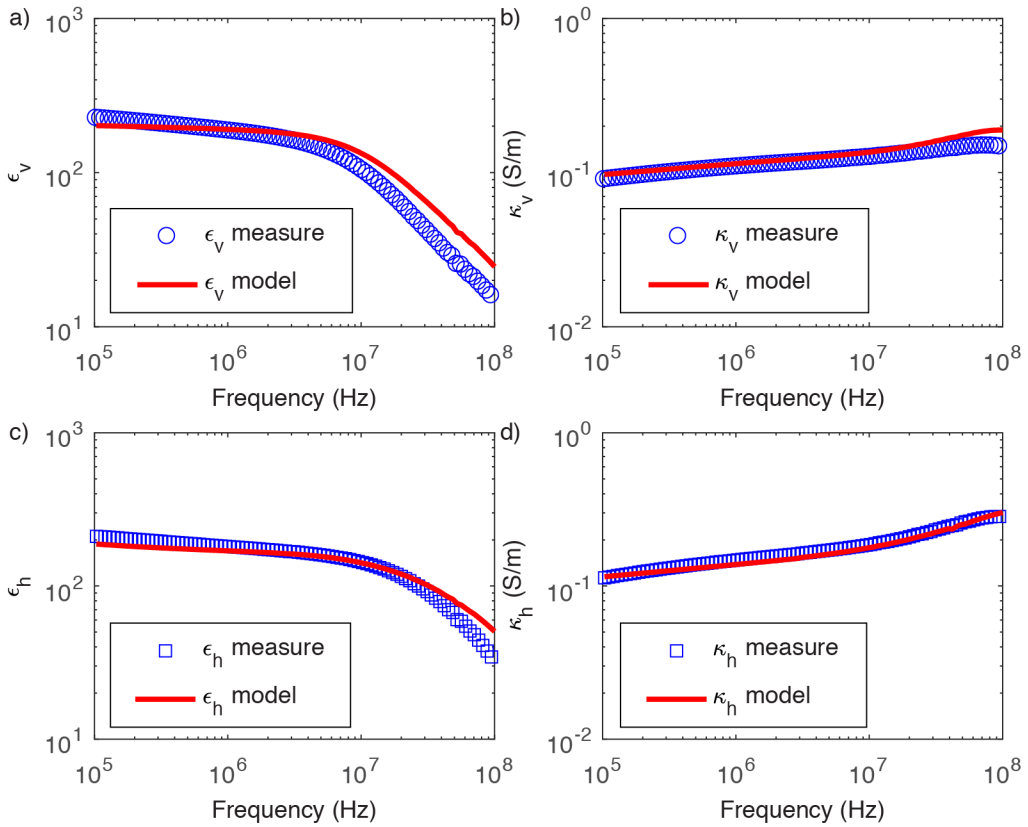


*Figure 58. Comparison of the experimental measurements with the modelling results for the artificial shale sample A2575_75. The coefficients are R = 0.9833 and R = 0.9775, respectively for the relative permittivity and conductivity in the vertical direction and R = 0.9979 and R = 0.9940 for the relative permittivity and conductivity in the horizontal direction, respectively.*

Figure 59 shows the modelling results for the sample A4060_75. When the silt grain aspect ratio is determined to be 0.1 for both vertical and horizontal directions, the new multiphase anisotropic dielectric model gives best fit to the laboratory measurements with correlation coefficients of $R$ = 0.9921 and $R$ = 0.9433 for the vertical relative permittivity and conductivity and $R$ = 0.9971 and $R$ = 0.9943 for the horizontal relative permittivity and conductivity, respectively. The inverted silt aspect ratio is consistent with the results obtained for the sample A2575_75 with lower silt content and the uniform silt aspect ratio for orthogonal directions indicates that the silt grains are more homogeneously distributed in the sample so that the dielectric properties of the rock caused by the silt component can be effectively described by the isotropic model (Equation 33).

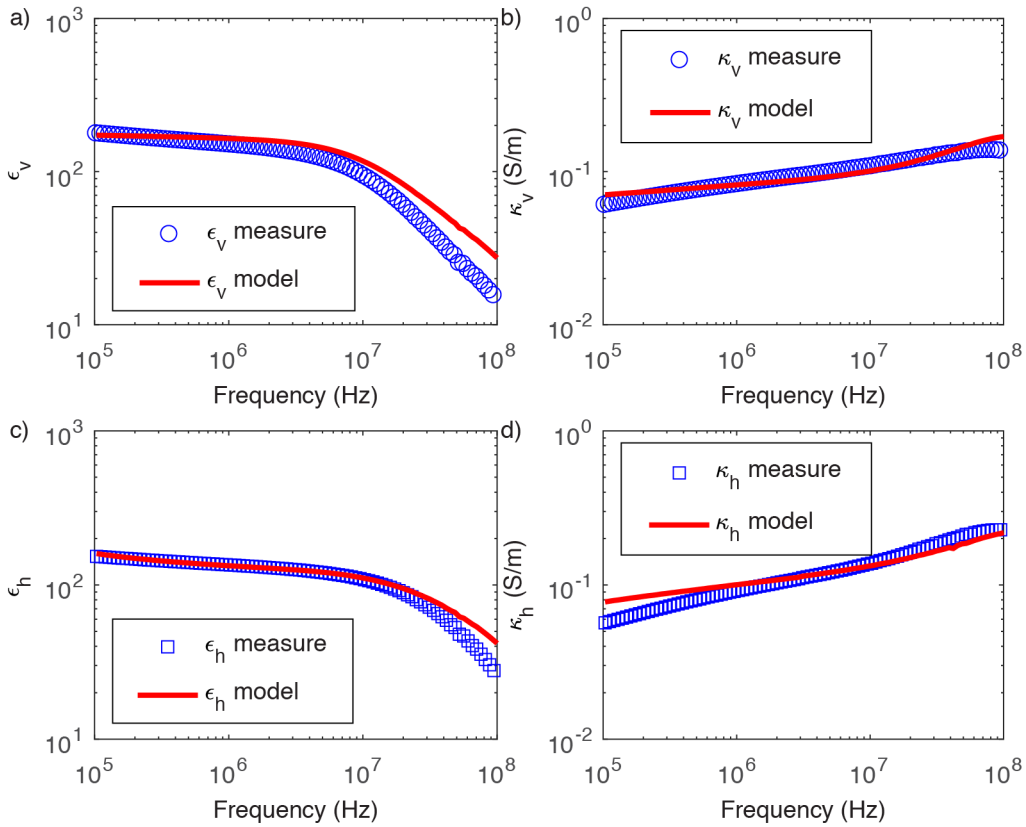


*Figure 59. Comparison of the experimental measurements with the modelling results for the artificial shale sample A4060_75. The coefficient coefficients are R = 0.9921 and R = 0.9433, respectively for the relative permittivity and conductivity in the vertical direction and R = 0.9971 and R = 0.9943 for the relative permittivity and conductivity in the horizontal direction, respectively.*

## DISCUSSION

A new multiphase model is developed for the anisotropic dielectric properties of sedimentary rocks. The model is based on the incremental algorithm (Berg, 2007, Han et al., 2015), in which a small amount of each component is added in every increment, making the model independent of the mixing order, a problem usually encountered by multiphase DEM models (Cosenza et al., 2009, Han et al., 2011, Spalburg, 1988). This ensures the uniqueness of the shale dielectric properties determined from the dielectric responses and volume fractions of the constituents and their specific microstructure described by the simplified orientation distribution function of the clay particles. A complete orientation distribution of clay minerals as measured may give better results for the model but will also increase the computational time dramatically due to the repeated incremental addition of a big number of directional phases. It turns out that

the proposed simplification of the clay orientation distribution function is a reasonable compromise that gives excellent model for laboratory data at low simulation costs.

The direction dependent dielectric properties of the wet clay aggregates as a function of frequency are inverted from the silt-free artificial shale sample using the developed multiphase dielectric model. Since the Maxwell–Wagner polarisation has already been accounted for by the new model, the obtained anisotropic dielectric properties of the wet clay minerals are thought to be the results of the Stern layer polarisation only in the directions along the axes of clay particles coated by the specific 75 g/l KCl brine. The obtained wet clay dielectric properties can be validated by the models based on Stern layer polarisation (Revil, 2013), however, such models usually need additional parameters (e.g., the formation factor and cation exchange capacity of the sample, and electrochemical properties of the connate brine) which are not available from the experiments. Nevertheless, the proposed modelling approach combines the Stern layer and Maxwell–Wagner polarisation mechanisms in the intermediate frequency range 0.1 MHz–100 MHz through the inverted wet clay dielectric properties, which is a clear advantage of the model over other theoretical models that deal with only one of the polarisation mechanisms.

In addition to the anisotropic dielectric properties of wet clay minerals, the shale dielectric anisotropy in the modelling is caused exclusively by aligned clay particles whereas the silt grains are assumed to be randomly dispersed, which reduces anisotropy if the host matrix is anisotropic. The 2-phase isotropic model (Asami, 2002) is therefore employed to account for the dielectric properties when the silt fractions are included. However, the different silt aspect ratios are obtained from the inversion for the sample A2575_75 in two orthogonal directions which indicates that the contributions of the silt grains to the bulk dielectric properties are dependent on the directions, meaning that the silt grains are not randomly distributed as assumed.

In the modelling, the wet clay dielectric properties are frequency dependent, while the relative permittivity and conductivity of the wet silt grains are assumed to be constant over the frequency range under investigation. It should be noted, however, that the dielectric responses of wet quartz should also be a function of the frequency of an applied electrical field, due to the electrochemical interactions of the mineral-water system that give additional contribution to the rock dielectric properties (Davis and Annan, 1989, Revil and Skold, 2011, Daniels, 2004, Revil, 2013). To better determine the frequency dependent dielectric properties of wet silt, a separate

experiment measuring the relative permittivity and conductivity of the silt and 75 g/l KCl brine mixture as a function of frequency is needed. Then the inversion algorithm can be implemented to remove the effects of Maxwell–Wagner polarisation to estimate the frequency dependent dielectric properties of wet silt resulting merely from the Stern layer polarisation. The derived relative permittivity and conductivity of wet silt are essentially the effective values resulted from the electrochemical Stern layer polarisation at each frequency (de Lima and Sharma, 1992).

The proposed modelling approach can be used to calibrate and compare the results of different geophysical tools that measure the dielectric properties in different directions (e.g., dielectric logging from the horizontal direction and surface induced polarisation method from the vertical direction). It can also be used to determine the geo-fluids type and concentration and to estimate the transport properties of shales. Another important potential application of the modelling is for the detection and prediction of the overpressure in shales caused by their extremely low permeability. Accurate prediction and detection of overpressure help to understand the geological history of a sedimentary basin, hydrocarbon migration, and trapping in the reservoir, and significantly reduce the risks of drilling hazards during hydrocarbon exploitation (McPherson, 1999, Muggeridge and Mahmode, 2012, Tingay et al., 2009, Han et al., 2017). Overpressure results in lower than expected electrical resistivity, reciprocal of conductivity. Conventional overpressure prediction models, based on electrical properties, evaluate the difference between the measured electrical properties and those of the normally compacted shales at the same depth in order to estimate the abnormal pore pressure (Hottmann and Johnson, 1965, Zhang, 2011). Since the developed multiphase dielectric model does not take into account the pressure effects, the modelled shale electrical properties can then be regarded as the electrical properties of the shales if the pore pressure is normal (i.e., the normally compacted shale electrical properties), which can be further employed for the overpressure prediction based on their difference from the measured electrical anomalies.

## SUMMARY OF CHAPTER 6

A multiphase incremental model has been developed for the anisotropic dielectric properties of sedimentary rocks. The model is suitable for any number of mineral grain components aligned in any direction and is independent of the mixing order. A new modelling approach for the frequency dependent anisotropic dielectric properties of shales takes into account the measured orientation distribution function of clay particles and the dielectric properties of wet clay minerals inverted from the obtained dielectric behaviours of the pure clay artificial shale sample.

The method combines the two important polarisation mechanisms (i.e., the Stern layer polarisation and the Maxwell–Wagner polarisation, respectively) taking effect in the frequency range of 0.1–100 MHz. Application of the modelling approach to the artificial shale samples with varying silt contents shows that the frequency dependent anisotropic dielectric properties of shales can be adequately modelled by using a reasonable aspect ratio and constant dielectric parameters for the silt grains.

# Outlook

Experimental characterisation of the petrophysical and rock physics properties of rocks in relation to their mineral composition and microstructure is a pivotal point in the quantitative interpretation of geophysical data. This might be a very challenging task when dealing with shales. The complexity of their composition, lack of preserved core material, and inhomogeneity of the natural rocks result in a poor notion of the shale properties and factors influencing their development. The inability to prove the theoretical models on the experimental data obtained on natural materials only exaggerates the problem.

In this thesis, I created a setup and proposed a new methodology for simultaneous measurements of compaction trends of anisotropic elastic and hydraulic properties of shale in fully controlled laboratory conditions. I adopted and enhanced the signal processing techniques used in seismology and non-destructive testing to measure elastic properties of shales with high precision. I investigated the anisotropic electric properties in relation to the connate fluids and mineral composition of shales. I used the state-of-the-art methods for characterization of shale microstructure that allowed modelling the anisotropic elastic and dielectric properties of shales. The key findings of my work are following.

- Anisotropy of elastic properties in shales starts to develop at critical porosity, when the rock becomes rigid.
- Shales with different initial clay microstructure exhibit significantly different compressibility and consequently compaction trends of elastic properties.
- Orientation of the clay fraction has the dominating effect on elastic anisotropy, while the increasing amount of non-clay inclusions decreases the anisotropy.
- Elastic properties of clay matrix are independent on the volumetric concentration of quartz inclusions when the latter is low, less that ~20 %, and vice versa.
- Silt fraction and clay mineralogy are the two key parameters that are responsible for broad variations of permeability in shales at the same porosity.
- The strong correlations, $R^2$ above 0.95, between the hydraulic permeability and seismic attributes, the acoustic impedance and $V_P/V_S$ ratio, are observed.

- At frequencies in a range of 10–100 MHz, the real part of relative dielectric permittivity has different linear trends with porosity in fresh water and brine saturated samples.
- The magnitude and the characteristic frequency of the peak values in dielectric anisotropy curves as well as the crossover with isotropy point is dependent on salinity, the cation composition of saturating fluid, and the clay content of shale.
- The absolute peak value of dielectric loss in shales and its characteristic frequency depends on the cation composition of the saturating brine, its salinity, and the orientation of an applied electric field relative to the shale bedding.
- A multiphase incremental model has been developed for the anisotropic dielectric properties of sedimentary rocks. The model is for any number of components aligned in any direction and is independent of the mixing order. The model takes into account the measured orientation distribution functions of clay particles and the dielectric properties of wet clay minerals.

The key ideas and results discussed and presented in the thesis have a potential for further investigation and can be readily applied in various aspects of geophysical exploration. Thus, the results of compaction experiments shown in Chapters 3 and 4, including the measured elastic properties and parameters of microstructure of the studied shales, form a solid basis for building new and testing of the existing rock physics models. The latter will help to better characterize the physical nature of elastic properties of individual clay minerals and elastic anisotropy of shales in general. Also, it is shown that reliable compaction trends that are necessary for velocity model building and seismic inversions can be studied in controlled laboratory conditions. Therefore, better understanding of elastic anisotropy in shales and its relation to rock diagenesis and microstructure will help to improve the existing imaging methodologies. Results obtained and described in Chapter 4 are central for basin and fluid flow modelling as they provide compaction trends for permeability of shales and illustrate the strong influence of mineralogical composition on them. The other important result illustrates the relationship between permeability of shales and seismic attributes which unlocks the potential to invert seismic data for hydraulic properties of shales, which in its turn is indispensable for modelling of fluid migration in conventional and unconventional reservoirs and in various geosequestration scenarios. Finally, the results of Chapter 5 illustrate some key features of shales that can be

employed when designing effective strategies for hydrocarbon extraction and production from unconventional reservoirs using dielectric heating.

Additionally, I would like to highlight that experimental procedure illustrated in the thesis allows studying relationships between anisotropic elastic properties and permeability in shales and their compaction trends in a broad porosity range, from ~40 to 10 %, what to the author's knowledge has not been done before. It has been shown that the experimentally obtained parameters of the clay matrix and quantitative parameters of microstructure acquired at the end of compaction experiments may be effectively used for modelling the anisotropic elastic and dielectric properties of shales. The simplicity of implementation of the presented methodology and the spectrum of its applications should encourage fellow rock-physicist to utilize it for design of new and validation of existing rock-physics models.

# List of figures

# List of tables

# Bibliography


ABRAHAM, T., VAN NESTE, C. W., AFACAN, A. & THUNDAT, T. 2016. Dielectric Relaxation-Based Capacitive Heating of Oil Sands. *Energy & Fuels,* 30**,** 1987-1996.

ADAMS, A. L., NORDQUIST, T. J., GERMAINE, J. T. & FLEMINGS, P. B. 2016. Permeability anisotropy and resistivity anisotropy of mechanically compressed mudrocks. *Canadian Geotechnical Journal,* 53**,** 1474-1482.

AL-HARAHSHEH, M., KINGMAN, S., SAEID, A., ROBINSON, J., DIMITRAKIS, G. & ALNAWAFLEH, H. 2009. Dielectric properties of Jordanian oil shales. *Fuel Processing Technology,* 90**,** 1259-1264.

ALLAN, A. M., KANITPANYACHAROEN, W. & VANORIO, T. 2015. A multiscale methodology for the analysis of velocity anisotropy in organic-rich shale. *Geophysics,* 80**,** C73-C88.

APLIN, A. C., MATENAAR, I. F., MCCARTY, D. K. & VAN DER PLUIJM, B. A. 2006. Influence of mechanical compaction and clay mineral diagenesis on the microfabric and pore-scale properties of deep-water Gulf of Mexico mudstones. *Clays and Clay Minerals,* 54**,** 500-514.

ASAMI, K. 2002. Characterization of heterogeneous systems by dielectric spectroscopy. *Progress in Polymer Science,* 27**,** 1617-1659.

ASTM 2007. Test Method for Particle-Size Analysis of Soils. West Conshohocken, PA: ASTM International.

ASTM 2008. Density of Powders and Solids by Helium Displacement. West Conshohocken, PA: ASTM International.

BACHRACH, R. 2011. Elastic and resistivity anisotropy of shale during compaction and diagenesis: Joint effective medium modeling and field observations. *Geophysics,* 76**,** E175-E186.

BACKUS, G. E. 1962. Long-wave elastic anisotropy produced by horizontal layering. *Journal of Geophysical Research,* 67**,** 4427-4440.

BAKER, D. W., CHAWLA, K. S. & KRIZEK, R. J. 1993. Compaction Fabrics of Pelites - Experimental Consolidation of Kaolinite and Implications for Analysis of Strain in Slate. *Journal of Structural Geology,* 15**,** 1123-1137.

BAYUK, I. O., AMMERMAN, M. & CHESNOKOV, E. M. 2007. Elastic moduli of anisotropic clay. *Geophysics,* 72**,** D107-D117.

BELOBORODOV, R., PERVUKHINA, M., ESTEBAN, L. & LEBEDEV, M. 2015. Compaction of Quartz-kaolinite Powders with Aggregated Initial Microstructure - Elastic Properties and Anisotropy. *77th EAGE Conference and Exhibition 2015.* Madrid.

BELOBORODOV, R., PERVUKHINA, M. & LEBEDEV, M. 2016a. Measurements and Modelling of the Elastic Properties of Artificial Shales. *78th EAGE Conference and Exhibition 2016.* Vienna.

BELOBORODOV, R., PERVUKHINA, M., LUZIN, V., DELLE PIANE, C., CLENNELL, M. B., ZANDI, S. & LEBEDEV, M. 2016b. Compaction of quartz-kaolinite mixtures: The influence of the pore fluid composition on the development of their microstructure and elastic anisotropy. *Marine and Petroleum Geology,* 78**,** 426-438.

BERG, C. 2007. An effective medium algorithm for calculating water saturations at any salinity or frequency. *Geophysics,* 72**,** E59-E67.

BERNABÉ, Y., MOK, U. & EVANS, B. 2006. A note on the oscillating flow method for measuring rock permeability. *International Journal of Rock Mechanics and Mining Sciences,* 43**,** 311-316.
BERRYMAN, J. G. 1995. Mixture theories for rock properties. *AGU Reference Shelf***,** 205-228.
BERRYMAN, J. G. & HOVERSTEN, G. M. 2012. Modelling electrical conductivity for earth media with macroscopic fluid-filled fractures. *Geophysical Prospecting,* 61**,** 471-493.
BERTONCELLO, A. & HONARPOUR, M. M. 2013. Standards for Characterization of Rock Properties in Unconventional Reservoirs: Fluid Flow Mechanism, Quality Control, and Uncertainties. *SPE Annual Technical Conference and Exhibition.* Society of Petroleum Engineers.
BIRCH, F. 1960. The velocity of compressional waves in rocks to 10 kilobars: 1. *Journal of Geophysical Research,* 65**,** 1083-1102.
BJORLYKKE, K. 1998. Clay mineral diagenesis in sedimentary basins - a key to the prediction of rock properties. Examples from the North Sea Basin. *Clay Minerals,* 33**,** 15-34.
BJORLYKKE, K. 2014. Relationships between depositional environments, burial history and rock properties. Some principal aspects of diagenetic process in sedimentary basins. *Sedimentary Geology,* 301**,** 1-14.
BOHINC, K., KRALJ-IGLIČ, V. & IGLIČ, A. 2001. Thickness of electrical double layer. Effect of ion size. *Electrochimica Acta,* 46**,** 3033-3040.
BOYARSKII, D., TIKHONOV, V. & KOMAROVA, N. Y. 2002. Model of dielectric constant of bound water in soil for applications of microwave remote sensing. *Progress In Electromagnetics Research,* 35**,** 251-269.
BROWN, M. A., GOEL, A. & ABBAS, Z. 2016. Effect of Electrolyte Concentration on the Stern Layer Thickness at a Charged Interface. *Angewandte Chemie International Edition,* 55**,** 3790-3794.
BRUGGEMAN, D. A. G. 1935. Berechnung verschiedener physikalischer Konstanten von heterogenen Substanzen. I. Dielektrizitätskonstanten und Leitfähigkeiten der Mischkörper aus isotropen Substanzen. *Annalen der Physik,* 416**,** 636-664.
BUSSIAN, A. E. 1983. Electrical conductance in a porous medium. *Geophysics,* 48**,** 1258-1268.
CAMPBELL, D. L. 1976. Electrical Anisotropy of Oil Shales in Piceance Basin, Colorado. *Geophysics,* 41**,** 345-345.
CANAN, B. 1999. *Dielectric properties of mixtures of clay-water-organic compounds.* Colorado School of Mines. Arthur Lakes Library.
CHUHROV, F. V. 1955. *Colloids it the earth crust*, USSR Academy of Science.
CLAVIER, C., COATES, G. & DUMANOIR, J. 1984. Theoretical and Experimental Bases for the Dual-Water Model for Interpretation of Shaly Sands. *Society of Petroleum Engineers Journal,* 24**,** 153-168.
CLENNELL, M. B., DEWHURST, D. N., BROWN, K. M. & WESTBROOK, G. K. 1999. Permeability anisotropy of consolidated clays. *Geological Society, London, Special Publications,* 158**,** 79-96.
COLLINS, K. & MCGOWN, A. 1974. The form and function of microfabric features in a variety of natural soils. *Géotechnique,* 24**,** 223-254.
COSENZA, P., GHORBANI, A., CAMERLYNCK, C., REJIBA, F., GUÉRIN, R. & TABBAGH, A. 2009. Effective medium theories for modelling the relationships between electromagnetic properties and hydrological variables in geomaterials: a review. *Near Surface Geophysics,* 7**,** 563-578.

DANIELS, D. J. 2004. *Ground Penetrating Radar*, Institution of Engineering and Technology.

DAVIS, J. L. & ANNAN, A. P. 1989. Ground-Penetrating Radar for High-Resolution Mapping of Soil and Rock Stratigraphy1. *Geophysical Prospecting,* 37**,** 531-551.

DAY-STIRRAT, R. J., APLIN, A. C., SRODON, J. & VAN DER PLUIJM, B. A. 2008. Diagenetic reorientation of phyllosilicate minerals in Paleogene mudstones of the Podhale Basin, southern Poland. *Clays and Clay Minerals,* 56**,** 100-111.

DAY-STIRRAT, R. J., FLEMINGS, P. B., YOU, Y., APLIN, A. C. & VAN DER PLUIJM, B. A. 2012. The fabric of consolidation in Gulf of Mexico mudstones. *Marine Geology,* 295**,** 77-85.

DAY-STIRRAT, R. J., SCHLEICHER, A. M., SCHNEIDER, J., FLEMINGS, P. B., GERMAINE, J. T. & VAN DER PLUIJM, B. A. 2011. Preferred orientation of phyllosilicates: Effects of composition and stress on resedimented mudstone microfabrics. *Journal of Structural Geology,* 33**,** 1347-1358.

DE LIMA, O. A. L. & SHARMA, M. M. 1990. A grain conductivity approach to shaly sandstones. *Geophysics,* 55**,** 1347-1356.

DE LIMA, O. A. L. & SHARMA, M. M. 1992. A generalized Maxwell-Wagner theory for membrane polarization in shaly sands. *Geophysics,* 57**,** 431-440.

DELLE PIANE, C., ALMQVIST, B. S. G., MACRAE, C. M., TORPY, A., MORY, A. J. & DEWHURST, D. N. 2015. Texture and diagenesis of Ordovician shale from the Canning Basin, Western Australia: Implications for elastic anisotropy and geomechanical properties. *Marine and Petroleum Geology,* 59**,** 56-71.

DELLINGER, J. & VERNIK, L. 1994. Do Travel-Times in Pulse-Transmission Experiments Yield Anisotropic Group or Phase Velocities. *Geophysics,* 59**,** 1774-1779.

DER'AGIN, B. V. 1989. *Theory of stability of colloids and thin films*, Consultants Bureau.

DEWERS, T. A., HEATH, J., EWY, R. & DURANTI, L. 2012. Three-dimensional pore networks and transport properties of a shale gas formation determined from focused ion beam serial imaging. *International Journal of Oil, Gas and Coal Technology,* 5**,** 229-248.

DEWHURST, D. N., APLIN, A. C., SARDA, J. P. & YANG, Y. L. 1998. Compaction-driven evolution of porosity and permeability in natural mudstones: An experimental study. *Journal of Geophysical Research: Solid Earth,* 103**,** 651-661.

DJERAN-MAIGRE, I., TESSIER, D., GRUNBERGER, D., VELDE, B. & VASSEUR, G. 1998. Evolution of microstructures and of macroscopic properties of some clays during experimental compaction. *Marine and Petroleum Geology,* 15**,** 109-128.

DONADILLE, J.-M. 2016. On the Petrophysical Analysis of Dielectric Anisotropy. Society of Petrophysicists and Well-Log Analysts.

DONG, X. B. & WANG, Y. H. 2008. The Effects of the pH-Influenced Structure on the Dielectric Properties of Kaolinite-Water Mixtures. *Soil Science Society of America Journal,* 72**,** 1532-1541.

DOUBE, M., KLOSOWSKI, M. M., ARGANDA-CARRERAS, I., CORDELIERES, F. P., DOUGHERTY, R. P., JACKSON, J. S., SCHMID, B., HUTCHINSON, J. R. & SHEFELBINE, S. J. 2010. BoneJ Free and extensible bone image analysis in ImageJ. *Bone,* 47**,** 1076-1079.

DRÆGE, A., JAKOBSEN, M. & JOHANSEN, T. A. 2006. Rock physics modelling of shale diagenesis. *Petroleum Geoscience,* 12**,** 49-57.

DUTTA, T., MAVKO, G., MUKERJI, T. & LANE, T. 2009. Compaction trends for shale and clean sandstone in shallow sediments, Gulf of Mexico. *The Leading Edge,* 28**,** 590-596.

EFREMOV, I. F. 1971. *Periodic colloidal structures,* Leningrad, Izd-vo "Himiya".

ELLIS, M. H., SINHA, M. C., MINSHULL, T. A., SOTHCOTT, J. & BEST, A. I. 2010. An anisotropic model for the electrical resistivity of two-phase geologic materials. *Geophysics,* 75**,** E161-E170.

FAM, M. & SANTAMARINA, C. 1995. Study of Geoprocesses with Complementary Mechanical and Electromagnetic Wave Measurements in an Oedometer. *Geotechnical Testing Journal,* 18**,** 307-314.

FAWAD, M., MONDOL, N. H., JAHREN, J. & BJORLYKKE, K. 2010. Microfabric and rock properties of experimentally compressed silt-clay mixtures. *Marine and Petroleum Geology,* 27**,** 1698-1712.

FISCHER, G. J. 1992. The Determination of Permeability and Storage Capacity: Pore Pressure Oscillation Method. *In:* EVANS, B. & WONG, T.-F. (eds.) *Fault Mechanics and Transport Properties of Rocks - A Festschrift in Honor of W. F. Brace.* Academic Press.

FREED, D., SELEZNEV, N., HOU, C.-Y., FELLAH, K., LITTLE, J., DUMY, G. & SEN, P. 2016. A Physics-Based Model for the Dielectric Response of Shaly Sands. Society of Petrophysicists and Well-Log Analysts.

FREED, R. L. & PEACOR, D. R. 1989. Variability in Temperature of the Smectite Illite Reaction in Gulf-Coast Sediments. *Clay Minerals,* 24**,** 171-180.

GAO, Q., TAO, J., HU, J. & YU, X. 2015. Laboratory study on the mechanical behaviors of an anisotropic shale rock. *Journal of Rock Mechanics and Geotechnical Engineering,* 7**,** 213-219.

GARROUCH, A. A. & SHARMA, M. M. 1994. The Influence of Clay Content, Salinity, Stress, and Wettability on the Dielectric-Properties of Brine-Saturated Rocks - 10 Hz to 10 Mhz. *Geophysics,* 59**,** 909-917.

GELIUS, L.-J. & WANG, Z. 2008. Modelling production caused changes in conductivity for a siliciclastic reservoir: a differential effective medium approach. *Geophysical Prospecting,* 56**,** 677-691.

GLOVER, P. W. J., MEREDITH, P. G., SAMMONDS, P. R. & MURRELL, S. A. F. 1994. Ionic surface electrical conductivity in sandstone. *Journal of Geophysical Research: Solid Earth,* 99**,** 21635-21650.

HAMILTON, E. L. 1979. Sound-Velocity Gradients in Marine-Sediments. *Journal of the Acoustical Society of America,* 65**,** 909-922.

HAMILTON, E. L. 1980. Geoacoustic Modeling of the Sea-Floor. *Journal of the Acoustical Society of America,* 68**,** 1313-1340.

HAN, T., BEST, A. I., MACGREGOR, L. M., SOTHCOTT, J. & MINSHULL, T. A. 2011. Joint elastic-electrical effective medium models of reservoir sandstones. *Geophysical Prospecting,* 59**,** 777-786.

HAN, T., CLENNELL, M. B., JOSH, M. & PERVUKHINA, M. 2015. Determination of effective grain geometry for electrical modeling of sedimentary rocks. *Geophysics,* 80**,** D319-D327.

HAN, T., PERVUKHINA, M., BEN CLENNELL, M. & NEIL DEWHURST, D. 2017. Model-based pore-pressure prediction in shales: An example from the Gulf of Mexico, North America. *Geophysics,* 82**,** M37-M42.

HANAI, T. 1960. Theory of the dielectric dispersion due to the interfacial polarization and its application to emulsions. *Kolloid-Zeitschrift,* 171**,** 23-31.
HANAI, T. 1961. A remark on the "Theory of the dielectric dispersion due to the interfacial polarization". *Kolloid-Zeitschrift,* 175**,** 61-62.
HASANOV, A. K. 2014. *Reservoir transport and poroelastic properties from oscillating pore pressure experiments.* Thesis M.S., Colorado School of Mines.
HASANOV, A. K., PRASAD, M. & BATZLE, M. L. 2017. Simultaneous measurements of transport and poroelastic properties of rocks. *Review of Scientific Instruments,* 88**,** 124503.
HEDBERG, H. D. 1936. Gravitational compaction of clays and shales. *American Journal of Science,* Series 5 Vol. 31**,** 241-287.
HELLER, R., VERMYLEN, J. & ZOBACK, M. 2014. *Experimental investigation of matrix permeability of gas shales,* Tulsa, OK, USA, American Association of Petroleum Geologists.
HIRT, A. M., EVANS, K. F. & ENGELDER, T. 1995. Correlation between Magnetic-Anisotropy and Fabric for Devonian Shales on the Appalachian Plateau. *Tectonophysics,* 247**,** 121-132.
HIZEM, M., BUDAN, H., DEVILLE, B., FAIVRE, O., MOSSE, L. & SIMON, M. 2008. Dielectric Dispersion: A New Wireline Petrophysical Measurement. *SPE Annual Technical Conference and Exhibition.* Society of Petroleum Engineers.
HOFLER, S., WILL, G. & HAMM, H. M. 1988. Neutron-Diffraction Pole Figure Measurements on Iron-Meteorites. *Earth and Planetary Science Letters,* 90**,** 1-10.
HORNBY, B. E., SCHWARTZ, L. M. & HUDSON, J. A. 1994. Anisotropic Effective-Medium Modeling of the Elastic Properties of Shales. *Geophysics,* 59**,** 1570-1583.
HOTTMANN, C. E. & JOHNSON, R. K. 1965. Estimation of Formation Pressures from Log-Derived Shale Properties. *Journal of Petroleum Technology,* 17**,** 717-722.
JIANG, S., TANG, X., CAI, D., XUE, G., HE, Z., LONG, S., PENG, Y., GAO, B., XU, Z. & DAHDAH, N. 2017. Comparison of marine, transitional, and lacustrine shales: A case study from the Sichuan Basin in China. *Journal of Petroleum Science and Engineering,* 150**,** 334-347.
JOHANSEN, T. A., RUUD, B. O. & JAKOBSEN, M. 2004. Effect of grain scale alignment on seismic anisotropy and reflectivity of shales. *Geophysical Prospecting,* 52**,** 133-149.
JOSH, M. 2014. Dielectric Permittivity: A Petrophysical Parameter for Shales. *Petrophysics,* 55**,** 319-332.
JOSH, M. 2017. A combination dielectric and acoustic laboratory instrument for petrophysics. *Measurement Science and Technology,* 28**,** 125904.
JOSH, M., CLENNELL, B. & CAUCHEFERT, M. 2016. Dielectric Permittivity and Anisotropy of Intact Multi-Saturated Organic Shales. Society of Petrophysicists and Well-Log Analysts.
JOSH, M., CLENNELL, M. B., RAVEN, M. D. & DEWHURST, D. N. 2015. Factors Controlling Dielectric Response of Clays and Shales. *SEG Technical Program Expanded Abstracts 2015.*
KANG, X., KANG, G. C. & BATE, B. 2014. Measurement of Stiffness Anisotropy in Kaolinite Using Bender Element Tests in A Floating Wall Consolidometer. *Geotechnical Testing Journal,* 37**,** 869-883.

KELLER, L. M., HOLZER, L., WEPF, R., GASSER, P., MUNCH, B. & MARSCHALL, P. 2011. On the application of focused ion beam nanotomography in characterizing the 3D pore space geometry of Opalinus clay. *Physics and Chemistry of the Earth,* 36**,** 1539-1544.

KRANZ, R. L., SALTZMAN, J. S. & BLACIC, J. D. 1990. Hydraulic diffusivity measurements on laboratory rock samples using an oscillating pore pressure method. *International Journal of Rock Mechanics and Mining Sciences & Geomechanics Abstracts,* 27**,** 345-352.

KREMER, F. & SCHÖNHALS, A. 2002. *Broadband Dielectric Spectroscopy*, Springer Berlin Heidelberg.

KRÜGER, M., GROSSE, C. U. & LEHMANN, F. 2013. Automated Shear-Wave Techniques to Investigate the Setting and Hardening of Concrete in Through-Transmission. *In:* GÜNEŞ, O. & AKKAYA, Y. (eds.) *Nondestructive Testing of Materials and Structures.* Dordrecht: Springer Netherlands.

KUILA, U., DEWHURST, D. N., SIGGINS, A. F. & RAVEN, M. D. 2011. Stress anisotropy and velocity anisotropy in low porosity shale. *Tectonophysics,* 503**,** 34-44.

LASH, G. G. & BLOOD, D. R. 2004. Origin of shale fabric by mechanical compaction of flocculated clay: Evidence from the Upper Devonian Rhinestreet shale, western New York, USA. *Journal of Sedimentary Research,* 74**,** 110-116.

LEROY, P., REVIL, A., KEMNA, A., COSENZA, P. & GHORBANI, A. 2008. Complex conductivity of water-saturated packs of glass beads. *Journal of Colloid and Interface Science,* 321**,** 103-117.

LONARDELLI, I., WENK, H. R. & REN, Y. 2007. Preferred orientation and elastic anisotropy in shales. *Geophysics,* 72**,** D33-D40.

LUFFEL, D. L., HOPKINS, C. W. & SCHETTLER, P. D., JR. 2013. Matrix Permeability Measurement of Gas Productive Shales. *SPE Annual Technical Conference and Exhibition.* Society of Petroleum Engineers.

MARCUSSEN, Ø., THYBERG, B. I., PELTONEN, C., JAHREN, J., BJØRLYKKE, K. & FALEIDE, J. I. 2009. Physical properties of Cenozoic mudstones from the northern North Sea: Impact of clay mineralogy on compaction trends. *AAPG Bulletin,* 93**,** 127-150.

MAXWELL, J. C. 1891. Electricity and magnetism. *A Treatise on Electricity and Magnetism.* Cambridge University Press.

MCPHERSON, B. J. O. L. 1999. Hydrodynamics and overpressure mechanisms in the Sacramento Basin, California. *American Journal of Science,* 299**,** 429-466.

MILITZER, B., WENK, H. R., STACKHOUSE, S. & STIXRUDE, L. 2011. First-principles calculation of the elastic moduli of sheet silicates and their application to shale anisotropy. *American Mineralogist,* 96**,** 125-137.

MILLER, D. E., HORNE, S. A. & WALSH, J. 2012. Precise inversion of logged slownesses for elastic parameters in a gas shale formation. *Geophysics,* 77**,** B197-B206.

MOKHTARI, M. & TUTUNCU, A. N. 2015. Characterization of anisotropy in the permeability of organic-rich shales. *Journal of Petroleum Science and Engineering,* 133**,** 496-506.

MONDOL, N. H., BJORLYKKE, K. & JAHREN, J. 2008. Experimental compaction of clays: relationship between permeability and petrophysical properties in mudstones. *Petroleum Geoscience,* 14**,** 319-337.

MONDOL, N. H., BJORLYKKE, K., JAHREN, J. & HOEG, K. 2007. Experimental mechanical compaction of clay mineral aggregates - Changes in physical

properties of mudstones during burial. *Marine and Petroleum Geology,* 24**,** 289-311.
MOYANO, B., SPIKES, K. T., JOHANSEN, T. A. & MONDOL, N. H. 2012. Modeling compaction effects on the elastic properties of clay-water composites. *Geophysics,* 77**,** D171-D183.
MUGGERIDGE, A. & MAHMODE, H. 2012. Hydrodynamic aquifer or reservoir compartmentalization? *AAPG Bulletin,* 96**,** 315-336.
MUKHAMETSHINA, A. & MARTYNOVA, E. 2013. Electromagnetic Heating of Heavy Oil and Bitumen: A Review of Experimental Studies and Field Applications. *Journal of Petroleum Engineering,* 2013**,** 7.
NISHIZAWA, O. 1982. Seismic Velocity Anisotropy in a Medium Containing Oriented Cracks - Transversely Isotropic Case. *Journal of Physics of the Earth,* 30**,** 331-347.
NUR, A., MAVKO, G., DVORKIN, J. & GALMUDI, D. 1998. Critical porosity: A key to relating physical properties to porosity in rocks. *The Leading Edge,* 17**,** 357-362.
OLHOEFT, G. R. 1981. Electrical properties of rocks. *Physical properties of rocks and minerals,* 2**,** 257-297.
OLHOEFT, G. R. Geophysical Detection Of Hydrocarbon And Organic Chemical Contamination. 5th EEGS Symposium on the Application of Geophysics to Engineering and Environmental Problems, 1992.
ORTEGA, J. A., ULM, F. J. & ABOUSLEIMAN, Y. 2007. The effect of the nanogranular nature of shale on their poroelastic behavior. *Acta Geotechnica,* 2**,** 155-182.
ORTEGA, J. A., ULM, F. J. & ABOUSLEIMAN, Y. 2010. The effect of particle shape and grain-scale properties of shale: A micromechanics approach. *International Journal for Numerical and Analytical Methods in Geomechanics,* 34**,** 1124-1156.
OSIPOV, V. I. 1976. *The Nature of the Strength and Deformation Properties of Clay Rocks*, Izd. Mosk. Univ.
OSIPOV, V. I., SOKOLOV, V. N. & EREMEEV, V. V. 2004. *Clay seals of oil and gas deposits,* Lisse, A.A. Balkema Publishers.
OSIPOV, V. I., SOKOLOV, V. N. & RUMYANTSEVA, N. A. 1989. *Microstructure of Clay Rocks,* Moscow, Nedra.
OWENS, W. H. 1973. Strain Modification of Angular Density Distributions. *Transactions-American Geophysical Union,* 54**,** 118-118.
PELTONEN, C., MARCUSSEN, O., BJORLYKKE, K. & JAHREN, J. 2009. Clay mineral diagenesis and quartz cementation in mudstones: The effects of smectite to illite reaction on rock properties. *Marine and Petroleum Geology,* 26**,** 887-898.
PERVUKHINA, M., DEWHURST, D., GUREVICH, B., KUILA, U., SIGGINS, T., RAVEN, M. & NORDGÅRD BOLÅS, H. 2008. Stress-dependent elastic properties of shales: Measurement and modeling. *The Leading Edge,* 27**,** 772-779.
PERVUKHINA, M., GOLODONIUC, P., GUREVICH, B., CLENNELL, M. B., DEWHURST, D. N. & NORDGARD-BOLAS, H. M. 2015a. Prediction of sonic velocities in shale from porosity and clay fraction obtained from logs - A North Sea well case study. *Geophysics,* 80**,** D1-D10.

PERVUKHINA, M., GUREVICH, B., DEWHURST, D. N., GOLODONIUC, P. & LEBEDEV, M. 2015b. Rock Physics Analysis of Shale Reservoirs. *Fundamentals of Gas Shale Reservoirs.* John Wiley & Sons, Inc.

PERVUKHINA, M., GUREVICH, B., GOLODONIUC, P. & DEWHURST, D. 2011. Parameterization of elastic stress sensitivity in shales. *Geophysics,* 76**,** Wa147-Wa155.

PERVUKHINA, M. & RASOLOFOSAON, P. N. J. 2015. Burial/Compaction and Seismic Anisotropy in Shaly Formations. *77th EAGE Conference and Exhibition 2015.* Madrid: EAGE.

PERVUKHINA, M. & RASOLOFOSAON, P. N. J. 2017. Compaction trend versus seismic anisotropy in shaly formations. *Geophysical Prospecting,* 65**,** 1351-1365.

PIANE, C. D., DEWHURST, D. N., SIGGINS, A. F. & RAVEN, M. D. 2011. Stress-induced anisotropy in brine saturated shale. *Geophysical Journal International,* 184**,** 897-906.

POLLASTRO, R. M. 1993. Considerations and Applications of the Illite-Smectite Geothermometer in Hydrocarbon-Bearing Rocks of Miocene to Mississippian Age. *Clays and Clay Minerals,* 41**,** 119-133.

RABAUTE, A., REVIL, A. & BROSSE, E. 2003. In situ mineralogy and permeability logs from downhole measurements: Application to a case study in chlorite-coated sandstones. *Journal of Geophysical Research: Solid Earth,* 108.

REVIL, A. 2013. On charge accumulation in heterogeneous porous rocks under the influence of an external electric field. *Geophysics,* 78**,** D271-D291.

REVIL, A. & GLOVER, P. W. J. 1998. Nature of surface electrical conductivity in natural sands, sandstones, and clays. *Geophysical Research Letters,* 25**,** 691-694.

REVIL, A., GRAULS, D. & BREVART, O. 2002. Mechanical compaction of sand/clay mixtures. *Journal of Geophysical Research: Solid Earth,* 107**,** ECV 11-1–ECV 11-15.

REVIL, A. & SKOLD, M. 2011. Salinity dependence of spectral induced polarization in sands and sandstones. *Geophysical Journal International,* 187**,** 813-824.

REVIL, A., WOODRUFF, W. F., TORRES-VERDÍN, C. & PRASAD, M. 2013. Complex conductivity tensor of anisotropic hydrocarbon-bearing shales and mudrocks. *Geophysics,* 78**,** D403-D418.

RIEKE, H. H., CHILINGARIAN, G. V. & FERTL, W. H. 1978. Review of the Importance of Gravitational Sediment Compaction in Oil Producing Areas. *Energy Sources,* 4**,** 165-193.

SABA, S., BARNICHON, J.-D., CUI, Y.-J., TANG, A. M. & DELAGE, P. 2014. Microstructure and anisotropic swelling behaviour of compacted bentonite/sand mixture. *Journal of Rock Mechanics and Geotechnical Engineering,* 6**,** 126-132.

SAEVIK, P. N., JAKOBSEN, M., LIEN, M. & BERRE, I. 2014. Anisotropic effective conductivity in fractured rocks by explicit effective medium methods. *Geophysical Prospecting,* 62**,** 1297-1314.

SAYERS, C. M. 1994. The Elastic-Anisotropy of Shales. *Journal of Geophysical Research: Solid Earth,* 99**,** 767-774.

SAYERS, C. M. 2005. Seismic anisotropy of shales. *Geophysical Prospecting,* 53**,** 667-676.

SAYERS, C. M. 2010. The Seismic Anisotropy of Shales. *Geophysics under Stress: Geomechanical Applications of Seismic and Borehole Acoustic Waves*, 105-121.

SCHINDELIN, J., ARGANDA-CARRERAS, I., FRISE, E., KAYNIG, V., LONGAIR, M., PIETZSCH, T., PREIBISCH, S., RUEDEN, C., SAALFELD, S., SCHMID, B., TINEVEZ, J. Y., WHITE, D. J., HARTENSTEIN, V., ELICEIRI, K., TOMANCAK, P. & CARDONA, A. 2012. Fiji: an open-source platform for biological-image analysis. *Nature Methods,* 9**,** 676-682.

SCHWARTZ, N. & FURMAN, A. 2012. Spectral induced polarization signature of soil contaminated by organic pollutant: Experiment and modeling. *Journal of Geophysical Research: Solid Earth,* 117.

SEN, P. N. 1980. The Dielectric And Conductivity Response Of Sedimentary Rocks. Society of Petroleum Engineers.

SEN, P. N. 1981. Relation of certain geometrical features to the dielectric anomaly of rocks. *Geophysics,* 46**,** 1714-1720.

SEN, P. N. & CHEW, W. C. 1983. The Frequency Dependent Dielectric And Conductivity Response Of Sedimentary Rocks. *Journal of Microwave Power,* 18**,** 95.

SEN, P. N., SCALA, C. & COHEN, M. H. 1981. A self-similar model for sedimentary rocks with application to the dielectric constant of fused glass beads. *Geophysics,* 46**,** 781-795.

SERGEYEV, Y. M., GRABOWSKAOLSZEWSKA, B., OSIPOV, V. I., SOKOLOV, V. N. & KOLOMENSKI, Y. N. 1980. The Classification of Microstructures of Clay Soils. *Journal of Microscopy-Oxford,* 120**,** 237-260.

SERIFF, A. J. 1985. Anisotropy, Shear-Waves, and Shales. *Geophysics,* 50**,** 367-368.

SONG, I. & RENNER, J. 2007. Analysis of oscillatory fluid flow through rock samples. *Geophysical Journal International,* 170**,** 195-204.

SPALBURG, M. The effective medium theory used to derive conductivity equations for clean and shaly hydrocarbon-bearing reservoirs. Eleventh European Formation Evaluation Symposium, 1988.

STERN, O. 1924. Zur Theorie Der Elektrolytischen Doppelschicht (The theory of the electrolytic double shift). *Zeitschrift für Elektrochemie und angewandte physikalische Chemie,* 30**,** 508-516.

STRAKHOV, N. M. 1967. *Principles of lithogenesis*, Springer.

TERZAGHI, K. 1925. Principles of soil mechanics, IV—Settlement and consolidation of clay. *Engineering News-Record,* 95**,** 874-878.

THOMSEN, L. 1986. Weak Elastic-Anisotropy. *Geophysics,* 51**,** 1954-1966.

THYBERG, B., JAHREN, J., WINJE, T., BJØRLYKKE, K. & FALEIDE, J. I. 2009. From mud to shale: rock stiffening by micro-quartz cementation. *First Break,* 27**,** 53-59.

TINGAY, M. R. P., HILLIS, R. R., SWARBRICK, R. E., MORLEY, C. K. & DAMIT, A. R. 2009. Origin of overpressure and pore-pressure prediction in the Baram province, Brunei. *AAPG Bulletin,* 93**,** 51-74.

VAN OLPHEN, H. 1977. *An introduction to clay colloid chemistry: for clay technologists, geologists, and soil scientists*, Wiley.

VASIN, R. N., WENK, H. R., KANITPANYACHAROEN, W., MATTHIES, S. & WIRTH, R. 2013. Elastic anisotropy modeling of Kimmeridge shale. *Journal of Geophysical Research: Solid Earth,* 118**,** 3931-3956.

VASSEUR, G., DJERANMAIGRE, I., GRUNBERGER, D., ROUSSET, G., TESSIER, D. & VELDE, B. 1995. Evolution of Structural and Physical

Parameters of Clays during Experimental Compaction. *Marine and Petroleum Geology,* 12**,** 941-954.
VERNIK, L. & NUR, A. 1992. Ultrasonic Velocity and Anisotropy of Hydrocarbon Source Rocks. *Geophysics,* 57**,** 727-735.
VOLTOLINI, M., WENK, H. R., MONDOL, N. H., BJORLYKKE, K. & JAHREN, J. 2009. Anisotropy of experimentally compressed kaolinite-illite-quartz mixtures. *Geophysics,* 74**,** D13-D23.
VON HIPPEL, A. R. 1954. *Dielectrics and waves,* New York; London, Wiley; Chapman & Hall.
VYZHVA, S. A., PRODAYVODA, G. T. & VYZHVA, A. S. 2014. Elastic Properties of Some Clay Minerals. *Nafta-Gaz,* R. 70**,** 743-756.
WAGNER, K. W. 1914. Erklärung der dielektrischen Nachwirkungsvorgänge auf Grund Maxwellscher Vorstellungen. *Archiv für Elektrotechnik,* 2**,** 371-387.
WANG, Q., CUI, Y. J., TANG, A. M., BARNICHON, J. D., SABA, S. & YE, W. M. 2013. Hydraulic conductivity and microstructure changes of compacted bentonite/sand mixture during hydration. *Engineering Geology,* 164**,** 67-76.
WANG, Y. H. & DONG, X. B. 2008. Complementary wave-based characterizations of sedimentation processes. *Journal of Geotechnical and Geoenvironmental Engineering,* 134**,** 47-56.
WANG, Y. H. & SIU, W. K. 2006. Structure characteristics and mechanical properties of kaolinite soils. I. Surface charges and structural characterizations. *Canadian Geotechnical Journal,* 43**,** 587-600.
WELLER, J. M. 1959. Compaction of sediments. *AAPG Bulletin,* 43**,** 273-310.
WENK, H. R., VOLTOLINI, M., MAZUREK, M., VAN LOON, L. R. & VINSOT, A. 2008. Preferred orientations and anisotropy in shales: Callovo-Oxfordian shale (France) and opalinus clay (Switzerland). *Clays and Clay Minerals,* 56**,** 285-306.
YANG, Y. L. & APLIN, A. C. 2010. A permeability-porosity relationship for mudstones. *Marine and Petroleum Geology,* 27**,** 1692-1697.
ZADEH, M. K., MONDOL, N. H. & JAHREN, J. 2016. Experimental mechanical compaction of sands and sand-clay mixtures: a study to investigate evolution of rock properties with full control on mineralogy and rock texture. *Geophysical Prospecting,* 64**,** 915-941.
ZHANG, J. 2011. Pore pressure prediction from well logs: Methods, modifications, and new approaches. *Earth-Science Reviews,* 108**,** 50-63.

---

# Appendices

## A. LIST OF MANUSCRIPTS

*Journal papers*

The study presented in Chapter 3 was published in the form of a full-length article: BELOBORODOV, R., PERVUKHINA, M., LUZIN, V., DELLE PIANE, C., CLENNELL, M. B., ZANDI, S. & LEBEDEV, M. 2016. Compaction of quartz-kaolinite mixtures: The influence of the pore fluid composition on the development of their microstructure and elastic anisotropy. *Marine and Petroleum Geology,* 78**,** 426-438.

The work described in Chapter 4 is published in the form of a full-length article: BELOBORODOV, R., PERVUKHINA, M. & LEBEDEV, M. 2018. Compaction trends of full stiffness tensor and fluid permeability in artificial shales. *Geophysical Journal International*, 212, 1687-1693.

The study presented in Chapter 5 is published in the form of a full-length article: BELOBORODOV, R., PERVUKHINA, M., HAN, T. & JOSH, M. 2017. Experimental Characterization of Dielectric Properties in Fluid Saturated Artificial Shales. *Geofluids*, 2017, 8.

Chapter 6 summarizes the work published in the form of a full-length article: HAN, T., BELOBORODOV, R., PERVUKHINA, M., JOSH, M., CUI, Y. & ZHI, P. 2018. Theoretical Modeling of Dielectric Properties of Artificial Shales. *Geofluids*, 2018, 12.

*Conference papers*

The results shown in the thesis were partially presented in a number of national and international scientific conferences:

BELOBORODOV, R., PERVUKHINA, M., ESTEBAN, L. & LEBEDEV, M. 2015a. Changes in elastic properties of artificial shales due to compaction. *ASEG Extended Abstracts.* Perth, WA: ASEG-PESA.

BELOBORODOV, R., PERVUKHINA, M., ESTEBAN, L. & LEBEDEV, M. 2015b. Changes in elastic properties of artificial shales due to compaction. *3IWRP Extended Abstracts.* Perth, WA: 3IWRP.

BELOBORODOV, R., PERVUKHINA, M., ESTEBAN, L. & LEBEDEV, M. 2015c. Compaction of Quartz-kaolinite Powders with Aggregated Initial Microstructure - Elastic Properties and Anisotropy. *77th EAGE Conference and Exhibition 2015.* Madrid.

BELOBORODOV, R., PERVUKHINA, M. & LEBEDEV, M. 2016. Measurements and Modelling of the Elastic Properties of Artificial Shales. *78th EAGE Conference and Exhibition 2016.* Vienna.

BELOBORODOV, R., PERVUKHINA, M. & LEBEDEV, M. 2017a. Compaction trends of permeability in artificial shales measured using pressure-oscillation technique. *79th EAGE Conference & Exhibition 2017.* Paris, France.

BELOBORODOV, R., PERVUKHINA, M. & LEBEDEV, M. 2017b. The coupling of elastic properties and hydraulic permeability in artificial shales. *SEG.* Houston.

BELOBORODOV, R., PERVUKHINA, M. & LEBEDEV, M. 2017c. Fast-track estimation of hydraulic permeability compaction trends during the mechanical compaction of artificial shales. *4th International Workshop on Rock Physics.* Trondheim, Norway.

## B. LIST OF CONFERENCES ATTENDED

The work I developed during my thesis (between December 2014 and August 2017) was presented at the following national and international conferences:

**Australian Society of Exploration Geophysics (ASEG-PESA)**

*Perth, Australia, February 2015*

Poster presentation: Changes in elastic properties of artificial shales due to compaction

**3rd International Workshop on Rock Physics (3rd IWRP)**

*Perth, Australia, April 2015*

Poster presentation: Changes in elastic properties of artificial shales due to compaction

**European Association of Geophysicists and Engineers (EAGE Madrid)**

*Madrid, Spain, June 2015*

Oral presentation: Compaction of quartz-kaolinite powders with aggregated initial microstructure: elastic properties and anisotropy

**Curtin Reservoir Geophysics Consortium (CRGC 2015)**

*Perth, Australia, December 2015*

Oral presentation: Compaction of quartz-kaolinite mixtures: effects of elongated inclusions and composition of pore fluid on elastic properties

**European Association of Geophysicists and Engineers (EAGE Vienna)**

*Vienna, Austria, May 2016*

Oral presentation: Measurements and modelling of the elastic properties of artificial shales

**Curtin Reservoir Geophysics Consortium (CRGC 2016)**

*Perth, Australia, December 2016*

Oral presentation: Pressure oscillation technique for permeability measurements in artificial shales

**4th International Workshop on Rock Physics (4th IWRP)**

*Trondheim, Norway, May 2017*

Oral presentation: Fast-track estimation of hydraulic permeability compaction trends during the mechanical compaction of artificial shales

**European Association of Geophysicists and Engineers (EAGE Paris)**

*Paris, France, June 2017*

Oral presentation: Compaction trends of permeability in artificial shales measured using pressure-oscillation technique

**SEG Annual Meeting 2017**

*Houston, USA, September 2017*

Oral presentation: The coupling of elastic properties and hydraulic permeability in artificial shales.

# Permissions to reuse the published articles

Copyright Clearance Center RightsLink® Home Create Account Help

**Title:** Compaction of quartz-kaolinite mixtures: The influence of the pore fluid composition on the development of their microstructure and elastic anisotropy

**Author:** Roman Beloborodov,Marina Pervukhina,Vladimir Luzin,Claudio Delle Piane,Michael B. Clennell,Setayesh Zandi,Maxim Lebedev

**Publication:** Marine and Petroleum Geology

**Publisher:** Elsevier

**Date:** December 2016



LOGIN

**If you're a copyright.com user,** you can login to RightsLink using your copyright.com credentials.

Already **a RightsLink user** or want to learn more?

Please note that, as the author of this Elsevier article, you retain the right to include it in a thesis or dissertation, provided it is not published commercially. Permission is not required, but please ensure that you reference the journal as the original source. For more information on this and on your other retained rights, please visit: https://www.elsevier.com/about/our-business/policies/copyright#Author-rights

BACK CLOSE WINDOW



Copyright Clearance Center RightsLink® Home Create Account Help

OXFORD UNIVERSITY PRESS

**Title:** Compaction trends of full stiffness tensor and fluid permeability in artificial shales

**Author:** Beloborodov, Roman; Pervukhina, Marina

**Publication:** Geophysical journal international

**Publisher:** Oxford University Press

**Date:** 2017-11-29



LOGIN

**If you're a copyright.com user,** you can login to RightsLink using your copyright.com credentials.

Already **a RightsLink user** or want to learn more?

**Crown Copyright**

This content is covered by Crown Copyright. You are not required to obtain permission to reuse this content.

Geofluids
Volume 2017 (2017), Article ID 1019461, 8 pages
https://doi.org/10.1155/2017/1019461





**Research Article**

# Experimental Characterization of Dielectric Properties in Fluid Saturated Artificial Shales

Roman Beloborodov,[1] Marina Pervukhina,[2] Tongcheng Han,[3,4] and Matthew Josh[2]

[1]Department of Exploration Geophysics, Curtin University, Perth, WA 6151, Australia
[2]CSIRO Energy, Perth, WA 6151, Australia
[3]School of Geosciences, China University of Petroleum (East China), Qingdao 266580, China
[4]Laboratory for Marine Mineral Resources, Qingdao National Laboratory for Marine Science and Technology, Qingdao 266071, China

Correspondence should be addressed to Roman Beloborodov; roman.beloborodov@postgrad.curtin.edu.au

Received 27 July 2017; Accepted 20 November 2017; Published 20 December 2017

Academic Editor: Feng Yang



Geofluids
Volume 2018 (2018), Article ID 2973181, 12 pages
https://doi.org/10.1155/2018/2973181





**Research Article**

# Theoretical Modeling of Dielectric Properties of Artificial Shales

Tongcheng Han,[1,2] Roman Beloborodov,[3] Marina Pervukhina,[4] Matthew Josh,[4] Yanlin Cui,[5] and Pengyao Zhi[6]

[1]School of Geosciences, China University of Petroleum (East China), Qingdao 266580, China
[2]Laboratory for Marine Mineral Resources, Qingdao National Laboratory for Marine Science and Technology, Qingdao 266071, China
[3]Department of Exploration Geophysics, Curtin University, Perth, WA 6151, Australia
[4]CSIRO Energy, Perth, WA 6151, Australia
[5]Library, China University of Petroleum (East China), Qingdao 266580, China
[6]College of Earth Science and Engineering, Shandong University of Science of Technology, Qingdao 266590, China

Correspondence should be addressed to Tongcheng Han; hantc@upc.edu.cn

Received 27 July 2017; Revised 18 October 2017; Accepted 9 November 2017; Published 11 January 2018

Academic Editor: Xiaohu Dong